POLITECNICO DI TORINO

MASTER THESIS

Raman Spectroscopy on Biochar

Author:
Jacopo ACQUAFRESCA

Supervisor:
Prof. Alberto TAGLIAFERRO

April 4, 2018

ii

POLITECNICO DI TORINO

Abstract

Nanotechnologies for ICTs
Department of Applied Science and Technology

Raman Spectroscopy on Biochar

by Jacopo ACQUAFRESCA

Raman Spectroscopy is one the most used techniques to study materials and nano-materials. After the technical improvement of the equipment used to perform the spectroscopy in the past thirty years, especially in terms of resolution and filter, it has estabiled as the principal instrument to evaluate and study carbons. The applications are very wide and with well known results, in particular for what concerns crystalline materials like diamond, graphene and grafite, for which is relatively easy to indentify properties and quality of different samples. The important knowledges learned in studying these materials had lead to shift the focus to more complex allotropes or coumponds, especially amorphous carbons and carbon nano-fibers. In this project, we studied a particular type of amorphous carbon: the Biochar. Biochar can be made in a lot of different ways, using different precursors (that are basically kind of woods) and differents amount of time and temperature during the process of pyrolysis. The purpose was to find some patterns in the spectra of this extremely disordered material and being able to relate them to different physical and chemical properties of different samples. The majority of work has being done almost entirely in Politecnico di Torino, only the production of the materials has been done almost entirely at the UK Biochar Research Centre. The process it was divided in some steps: first we perform spectroscopy to every samples to obtain the spectra. Then, using a Matlab program developed in Politecnico di Torino, we refined the spectra drawing the baseline, normalizing data between each other and fitting the results with a proper set of functions. Finally we confronted the signals finding some correspondance in terms of disorder, mostly due to the evolution of the state of the materials through different temperatures.

Acknowledgements

This dissertation presents the cumulative results of more than six months of research. During this time, I was greatly supported by many people who contributed in different ways and without whom this work would not have been possible.First and foremost, I would like to thank my supervisor Prof. Alberto Tagliaferro – I have felt privileged to be her Master student and experience the kindly, friendly, and supportive supervision. Then, special thanks go to Massimo Rovere. He was my supervisor for daily activities and experiments planning.I thank some of my colleagues not only for the help and association in many projects done in these years but also for the friendship. I would also like to thank all my friends, Giulia and my family for always being there to help and support me.

Contents

List of Figures

List of Tables

Chapter 1

Introduction

1.1 How to Study Carbons and Why

Carbon is a chemical element, with atomic number 6 and it belongs to group 14 of the periodic table.
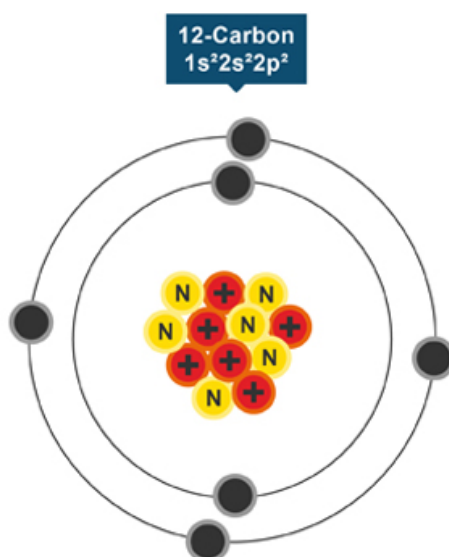
FIGURE 1.1: The Bohr representation of a 12-Carbon atom

It one of the most interesting, useful and complex elements because it forms a large variety of compounds, around the number of ten million, more than any other single element, and play a primary role in the life of every living being. It can bonds with many other type of atoms, including carbon, and in very different ways (single bonds, double bonds and even triple bonds), forming usually multiple stable covalent bonds. Its exceptional behaviour is due mainly to its hybridization features: carbon has the electron configuration of 1s2 2s2 2p2, this means that carbon would have 2 unpaired electrons in its p orbitals and that it will only form 2 bonds, but through the mixing of atomic orbitals it can assume planar (sp hybridization), triangular (sp2 hybridization) or even tetrahedral (sp3 hybridization) shape.

Carbons are a broad class of ordered or disordered solid phases composed primarily of elemental carbon. Both synthetic and natural materials belong to this
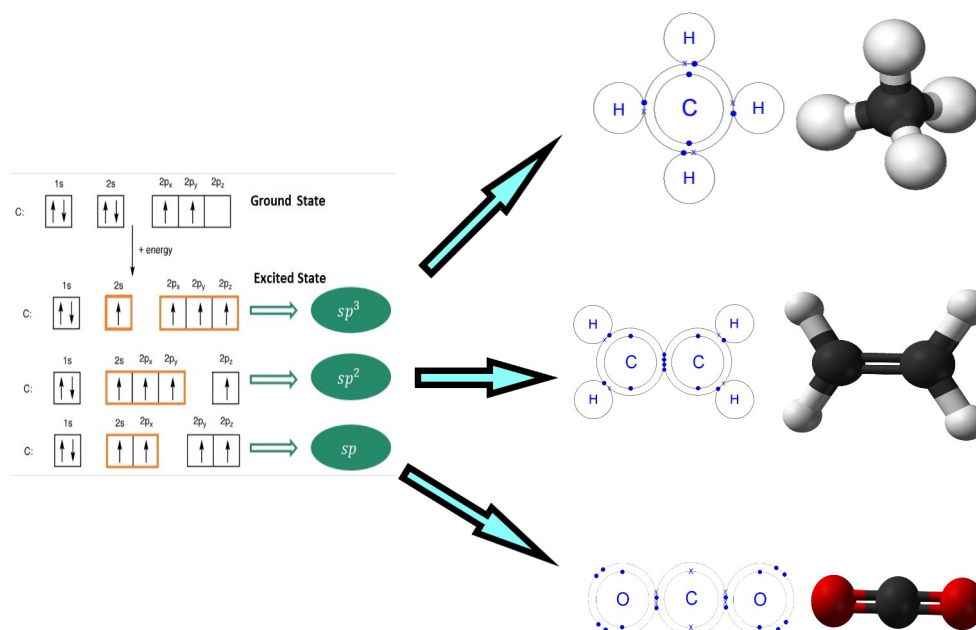
FIGURE 1.2: The hybridization of carbon atoms and some examples.
At Rigth from up to down: Methane(CH4),Ethyne(C2H2) and Carbon
Dioxide (CO2)

category and amid the most famous and studied materials we found a lot of al-
lotropes of pure carbon, for example graphene, graphite, diamond, carbon nan-
otubes, fullerenes, glassy carbon and other materials like carbon fibers, amorphous
hydrogenated carbon graphene oxide and chars. The fields of applications are virtu-
ally unlimited strarting from mechanical and thermal applications, to electronic and
photonic devices. Carbons can be used in the fabrication of smart and high tech-
nology materials, in the area harsh environment, energy storage and conversion,
biology, medicine and many other applications of the present and the future. The
key in discovering the properties of a carbon material is studying its chemical com-
position and atomic structure. The main method of investigation is spectroscopy
that is defined as the study of the interaction of the matter with radiative energy.

In general we can use different type of radiative energy and different kind of
instrumentation that exploit different physical phenomena to study this kind of ma-
terials. The most important and used ones are:

- XPS

- EELS

- IR Spectroscopy

- Raman Spectroscopy

Now we will briefly discuss these techniques and then we'll focus on Raman Scat-
tering

1.2 XPS Spectroscopy

X-ray photoelectron spectroscopy (XPS) is a technique suitable for determining the ionization potentials of molecules and so it is avaluable help when it takes the elemental composition (in terms of atomic percentage) or the quantitative differentiation of the same element in different chemical environments, and that peculiarity is very useful when you study carbon materials. This techique is performed in a Ultra Hig Vacuum chamber (expensive and slow) irradiating a material with X-rays and acquiring the subsequently emitted photoelectrons. This procedure is very surface-sensitive because the radiation is composed by electrons with energies below 1500 eV that interact with the sample in a way that allow only the electrons from the top atomic layers to escape from the surface. Analysing the energyies of the collected photoelectrons we can relate them to the the binding energy of the core levels of an atom that depends on the number of electrons that are located in the valence band. In a few words you can obtain informations abour the chemical state of the molecules on the surface of a solid sample of any kind, conductor, insulator or semiconductor as long as compatible with the vacuum environment.

General it can be used to evaluate sp2/sp3 ratio (see fig. 1.4) or Adventious Carbon, a thin layer of carbonaceous material is usually found on the surface of most air exposed samples (see fig. 1.3)
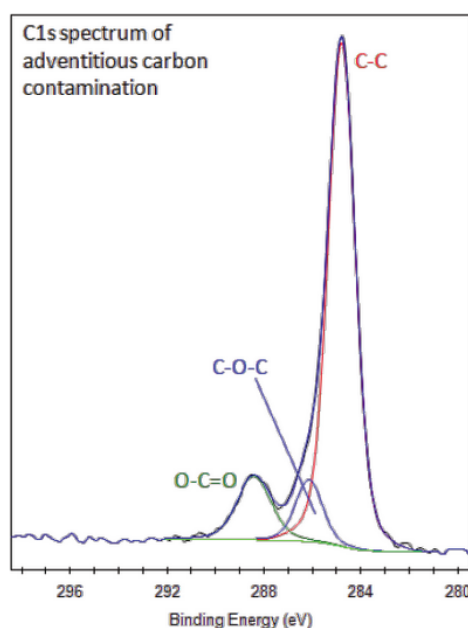
FIGURE 1.3: XPS spectrum of adventitious carbon

As shown in fig. 1.4, functionalized graphene have a very articulate spectrum in the C1s region, showing the contemporary presence of sp2 and sp3 components. We see that in the process of fitting, for sp2 carbon (a clue of the derivation of the material from probably graphite or graphene) you have to use asymettric functions, including in certain cases also symmetric loss peak. Meanwhile, for the sp3 component and functionalized carbon are necessary symmetric shapes. Usually the sp2 component is about 1 eV lower to the lower binding energy side of the sp3 carbon. At the end of the procedure of deconvolution it can be find the ratio of sp3 vs sp2 in the film.
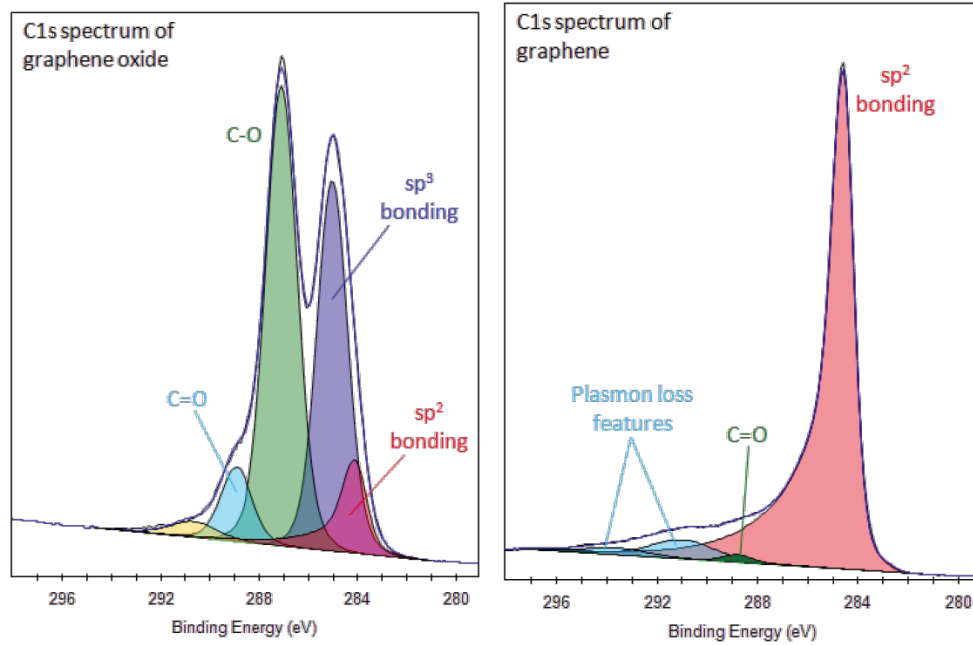
FIGURE 1.4: XPS spectra of Graphene Oxide and Graphene
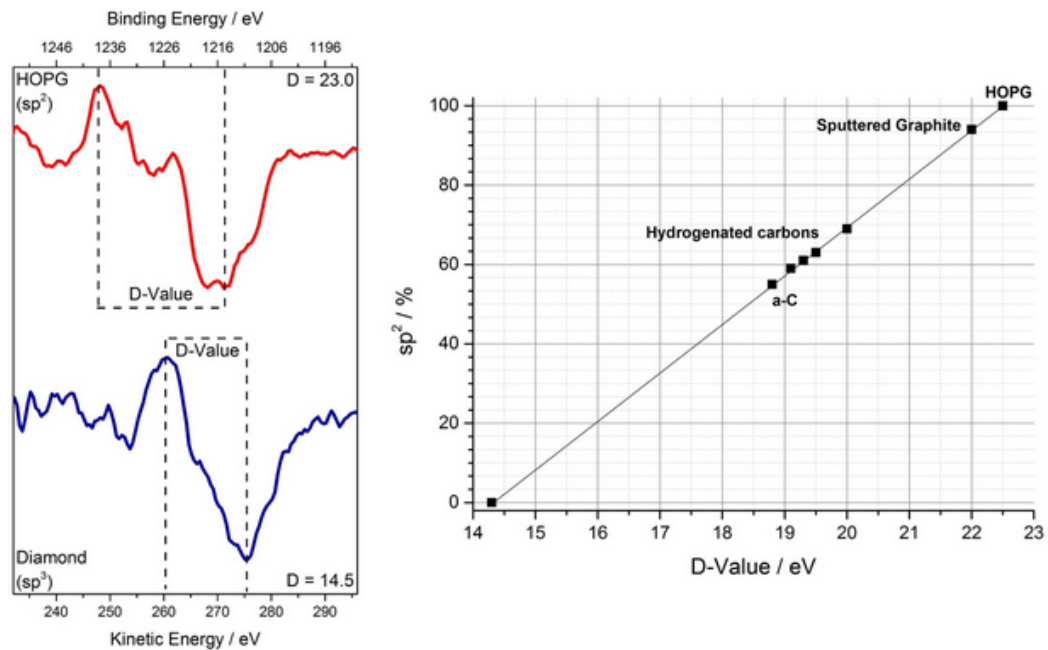
FIGURE 1.5: X-Ray induced C KLL spectra of of a sample of HOPG
and Diamond. Right: Grafic scheme of the percentual of sp2 content
in various kind of carbons

Apart from some exceptions like in previous case, it is hard to find a manner to fit uniquely mixed sp2/sp3 spectra. If you are studying non functionalized materials it is more useful focusing on the C KLL Auger peak (a phenomenon stil caused by X-ray irradiation), that is a invaluable method to distinguish sp2 carbon by the sp3 component in a semi quantitative way. Shown in fig. 1.5, you can see how it is derived the D-parameter from the differentiated form of the C KLL spectrum. The

value of that variable is directly linked with the quantity of sp2 and sp3 present in the material. This system is instead suitable with more difficulty in the of functionalized carbon materials.

1.3 EELS

EELS, or electron energy loss spectroscopy, include all the techniques that study the difference of energy between electrons sent towards a specimen and the same electrons after the interaction with the matter. Also this kind of spectroscopy is very useful to determine the chemical properties and the molecular structures of a material obtaining information about the kind, the number and the chemical state of the atoms and the interactions between them. In the specific of the most important of these techniques, trasmission EELS, exploits electrons with kinetic energies from 0.1 to 0.3 MeV that penetrate and get through the entire specimen, hitting the detector below. This procedure is performed in a transimission electron microscope (TEM).
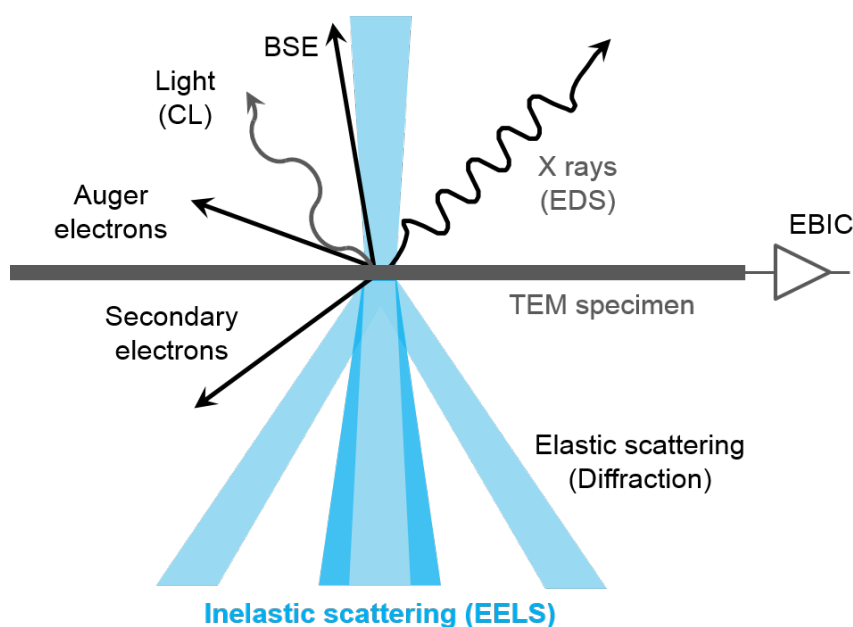
FIGURE 1.6: Schematic representation of an electron-sample interaction

Among the electrons that arrive at the sample, some of them continue their path with unaltered trajectory and energy, some others interact with the materials undergo elastic scattering or inelastic scattering (losing energy). This last possibility lead the specimen to an excited state. The excited state is due to the promotion of a core electron to a higher energy state when it is hitting by an incident electron. In particular, it can only get to an empty state of the atoms that can be above the Fermi energy (what we usually mean as the anti bonding orbitals of the molecular orbital theory) or even above the vacuum level. TEM detect the energy loss of the scattered electrons and correlating that with the energy of the states of the atoms of the studied material find which kind of elements, molecules and bonding is composed the specimen. There are some applications in the field of carbons: EELS can be used to detect particles of diamond, fullerene and graphite. This allotropes have similar

absorption peaks because are formed by the same element, usually around 284 eV (obviously due to the electronic states of that element). Fig. 1.7 shows the differences between the EELS spectra of graphite, fullerene and diamond. For example in graphite we observe a sharp peak that corresponds to excitation of the electron 1s orbital (K shell) to a π anti bonding orbital, that is empty. You can't find this peak in the spectrum of diamond because the previously mechanism is impossibile in that material (there is no π anti bonding orbital).
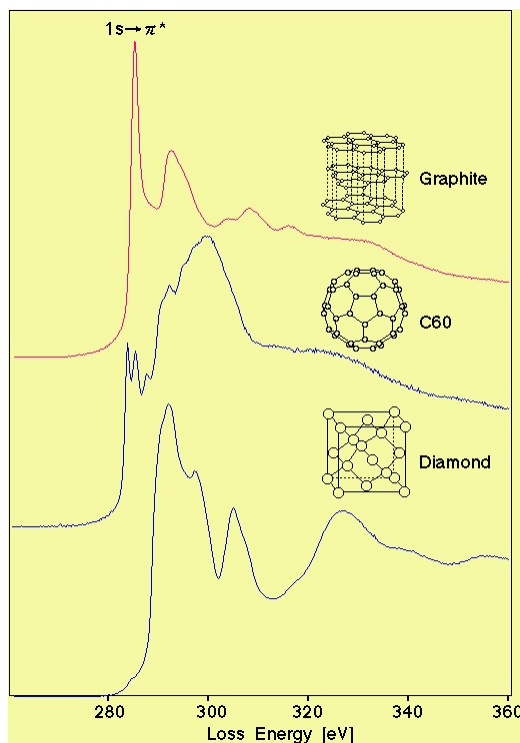
FIGURE 1.7: EELS spectra of Graphene, Fullerene and Diamond samples

At the end of the day the results and the applications of EELS are very similar to XPS but electron spettroscopy scan a very smaller volume of matter with respect to the X-ray spettroscopy. Another important thing to underline is about the instrument that performs the EELS. Infact, Trasmission Electron Microscope is a very expensive instrument and the sample studied need a specific preparation. The last important thing that it has to be taken in account that generally electrons carry more energy to the matter with respect to light rays and there are more probability of damaging the sample.

1.4   Infrared Spectroscopy

IR spettroscopy is an analytical technique useful in the study of virtually any kind of material in any physical state. It's based on incident radiations with wavelenght comprise between 4000 and 400 cm-1 (infrared spectrum). Collecting informations about the absorption or emission spectrum of a material you can correlate the peaks of the resulting signal directly to the bonds between atoms of the studied material and then to the elemental composition of the sample[16]. The analysis of the spectrum is not very simple because the interatomic bonds can vibrate in a lot of

different motions (mainly stretching and bending) and may absorb more than one infrared frequency. In general stretching produce more relevant peaks than bending, but bending peaks are useful when you have to differentiating types of bonds, like aromatic substitution, that are very similar between each others. The classical theory treatment explained the conditions for a material to be infrared active: at least one of the dipole moment component derivatives with respect to the normal coordinate, taken at the equilibrium position, should be non-zero. fig. 1.8 the plot of a component of the dipole moment against the normal coordinate that has a gradient different from zero. For example, neither of the carbon-carbon bonds in ethene or ethyne absorb IR radiation.
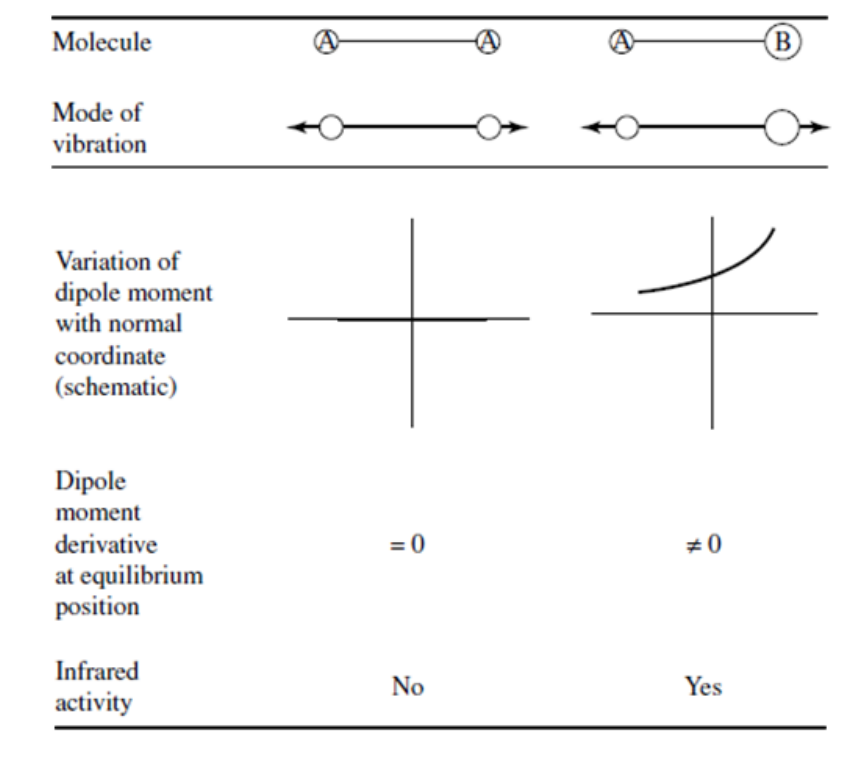
FIGURE 1.8: Dipole moment variations and infrared activities for an
A-A and an A-B molecule

Studying accurately the transmitted (or absorbed) spectrum it can be seen the molecular structure of some kind of materials because functional groups give rise to characteristic bands both in terms of intensity and position (frequency). For example can be used to characterized films of amorphous carbon nitride. fig. 1.10 reveal the position of some important carbon bonding.

Molecule				
Mode of vibration				
Variation of dipole moment with normal coordinate (schematic)				
Dipole moment derivative at equilibrium position	$= 0$		$\neq 0$	$\neq 0$
Infrared activity	No		Yes	Yes

FIGURE 1.9: Dipole moment variations and infrared activities for a linear A-B-A molecule
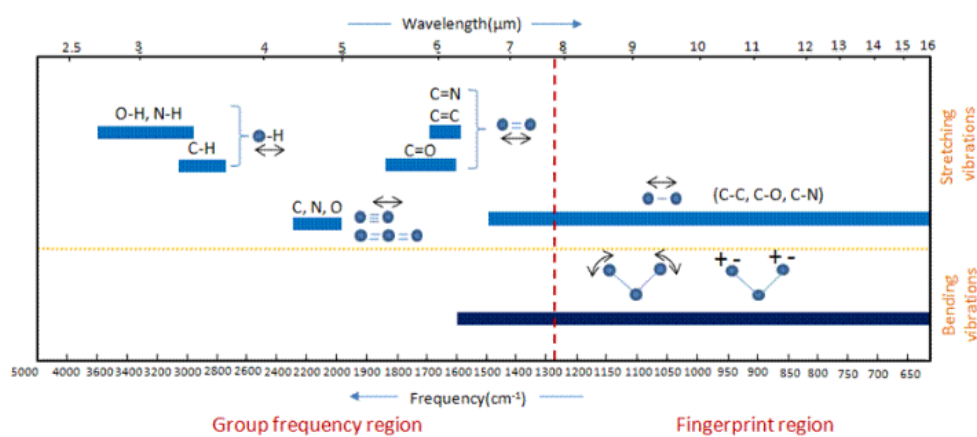
FIGURE 1.10: Scheme of the interpretation of a IR spectrum

Chapter 2

Raman Spectroscopy

2.1 Introduction to Raman Spectroscopy

Raman scattering is one of the most important and used form of molecular spectroscopy. It's based on the vibrational transitions of the molecules when irradiating with electromagnetic radiation, so Raman spectroscopy is similar to IR spectroscopy, but here are some evident differences between them. First, Raman scattering is a two photon event meanwhile IR is a one photon event (one photon absorbed and then one photon emitted). Second, it exploits another property of the matter, the change in the polarizability of the molecule with respect to its vibrational motion. Then an induced dipole moment arises from the interaction of the polarizability with the incoming radiation, and this dipole emitted a radiation containing both Rayleigh and Raman scattering. Raman radiation is the light scattering with a shifted frequency of the incident radiation due to the loss or the absorption of vibrational energy in the molecule, whereas the Rayleigh radiation is the main peak at the same frequency of the light source. The loss of vibrational energy is called anti-Stokes Raman scattering, while if the molecule gains energy we called that phenomenon Stokes Raman scattering[6].

2.2 Theoretical Basis of Incoherent Light Scattering

For a material, the origin of a scattered radiation are the oscillating electric and magnetic multipole moments induced by an electromagnetic radiation, in this case a light ray that can be treated in a strictly classical way for both semiclassical and quantum theories. There are mainly three kinds of source for the multipole moments: the oscillating electric dipole, the oscillating magnetic dipole and the electric quadrupole. The most intense is the oscillating electric dipole and in most cases is the only phenomenon that can be taken in account to evaluate the light scattering because the electric field can be approximate as constant over a molecule . Chiral systems requires the inclusion of the other two terms. The electric dipole radiates a light ray with intensity I:

$$I = k'_\omega \omega_s^4 p_0^2 \sin^2 \theta \qquad (2.1)$$

Where p_0 is the amplitude of the induced electric dipole with frequency ω_s. The main point for the theorical treatments is to find how ω_s and p_0 are determined by the properties of the scattering molecule and the incident electromagnetic radiation of frequency ω_1.

One practical way to treat a molecular system in a weak electric field is exploiting the perturbation theory for an hamiltonian of a charges system expanding the interaction system U in a Taylor series in the absence of the field[5].
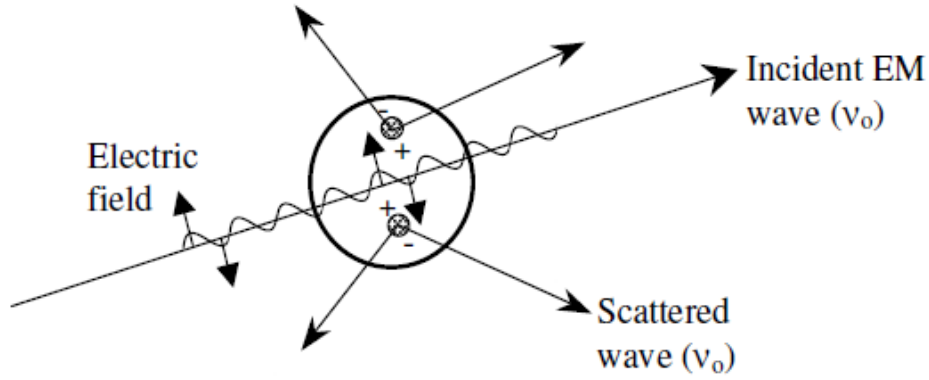
FIGURE 2.1: Illustration of an incoherent light scattering

$$U[(E)_0] = (U)_0 + (E_\rho)_0 [\frac{\partial U}{\partial (E_\rho)_0}] + \frac{1}{2}(E_\rho)_0 (E_\sigma)_0 [\frac{\partial^2 U}{\partial (E_\rho)_0 \partial (E_\sigma)_0}]$$

$$+ \frac{1}{6}(E_\rho)_0 (E_\sigma)_0 (E_\tau)_0 [\frac{\partial^3 U}{\partial (E_\rho)_0 \partial (E_\sigma)_0 \partial (E_\tau)_0}] + \ldots \quad (2.2)$$

In this case it has also known (for hypothesis) that the perturbation is caused interely by the electric dipole:

$$U = (U)_0 - p_0(E_0) \quad (2.3)$$

If we now differentiate eq. (2.2) with respect to E we obtain for the p component of the total dipole moment, both permanent and induced, of the molecule in the presence of a static electric field the following result:

$$p\rho = p_\rho^{per} + \frac{1}{2}\alpha_{\rho\sigma}(E_\sigma)_0 + \frac{1}{6}\beta_{\rho\sigma\tau}(E_\sigma)_0 (E_\tau)_0 + \ldots \quad (2.4)$$

$$p^{per} = [\frac{\partial U}{\partial (E_\rho)_0}]_0 \quad (2.5)$$

$$\alpha_{\rho\sigma} = [\frac{\partial^2 U}{\partial (E_\rho)_0 \partial (E_\sigma)_0}] \quad (2.6)$$

$$\beta_{\rho\sigma\tau} = [\frac{\partial^3 U}{\partial (E_\rho)_0 \partial (E_\sigma)_0 \partial (E_\tau)_0}] \quad (2.7)$$

where p_ρ^{per} is the ρ component of the permanent electric dipole vector p_ρ^{per} and $\alpha_{\rho\sigma}$ is a coefficient which relates the σ component of E_0 to the ρ component of p. It is evident that nine coefficients are required to relate the three components of the vector E_0 to the three components of the vector p. The nine coefficients of $\alpha_{\rho\sigma}$ are the components of the electric polarizability tensor, a second-rank tensor. Furthermore, $\beta_{\rho\sigma\tau}$ is a coefficient which relates the σ and τ components of E_0 to the ρ component of p. In the same way of the previous case, 27 such components are needed to relate the nine dyads of the electric field components to the three electric dipole components. The

twenty-seven coefficients are the components of the third rank tensor, the electric hyperpolarizability tensor $\beta_{\rho\sigma\tau}$. Using these definitions eq. (2.4) may be written in tensor form as:

$$p = p_\rho^{per} + \boldsymbol{\alpha} \cdot \mathbf{E} + \frac{1}{2}\boldsymbol{\beta} : \mathbf{E} + \ldots \tag{2.8}$$

To simplify we can say:

$$p = p_\rho^{per} + p^{ind} \tag{2.9}$$

$$p^{ind} = p^{(1)} + p^{(2)} + p^{(3)} + \ldots \tag{2.10}$$

$$p^{(1)} = \boldsymbol{\alpha} \cdot \mathbf{E} \tag{2.11}$$

In the next paragraphs we studied only $p^{(1)}$ that is the dominant terms in the formula of electric dipole moment and contains the polarizability tensor, the key factor in the Raman Effect.

2.3 Classical Treatment of Raman Scattering

From equation (2.11) we have $\alpha_{\rho\sigma}$ that is the and E is the strength of electric field of the incident EM wave. For the incident EM wave, the electric field may be expressed as:

$$E = E_0 \cos(\omega_1 t) \tag{2.12}$$

Where ω_1 is the angular frequency of the monochromatic EM wave. Instead the polarizability depends on the relative location of the individual atoms that usually can change of a little fraction from the equilibrium position. For such small displacement the variation of the polarizability with vibrations of the molecule can be expressed by expanding each component of the polarizability tensor a in a Taylor series with respect to the normal coordinates of vibration, as follows:

$$\alpha_{\rho\sigma} = (\alpha_{\rho\sigma})_0 + \sum_k (\frac{\partial \alpha_{\rho\sigma}}{\partial Q_k})_0 Q_k + \frac{1}{2}\sum_{k,l} (\frac{\partial^2 \alpha_{\rho\sigma}}{\partial Q_k \partial Q_l})_0 Q_k Q_l + \ldots \tag{2.13}$$

where $(\alpha_{\rho\sigma})_0$ is the value of $\alpha_{\rho\sigma}$ at the equilibrium configuration, $Q_k\ Q_l\ldots$ are normal coordinates of vibration associated with the molecular vibrational frequencies ω_k $\omega_l\ldots$, and the summations are over all normal coordinates. Then we can truncate the polynomial to the first two terms and then take in account only one mode of vibration. So:

$$\alpha_{\rho\sigma} = (\alpha_{\rho\sigma})_0 + (\frac{\partial \alpha_{\rho\sigma}}{\partial Q_k})_0 Q_k \tag{2.14}$$

If we take in account only simple harmonic motion, the time dependence of Q_k is given by:

$$Q_k = Q_{k0} \cos(\omega_k t) \tag{2.15}$$

Where $Q_k 0$ is the normal coordinate amplitude. Substituting eq. (2.15) in eq. (2.14) and eq. ((2.14), (2.12)) in eq. (2.11) we obtain:

$$p^{(1)} = (\alpha_{\rho\sigma})_0 E_0 \cos(\omega_1 t) + (\frac{\partial \alpha_{\rho\sigma}}{\partial Q_k})_0 E_0 Q_{k0} \cos(\omega_k t)\cos(\omega_1 t) \tag{2.16}$$

and then applying trigonometrical substitution:

$$p^{(1)} = (\alpha_{\rho\sigma})_0 E_0 \cos(\omega_1 t) + \frac{1}{2}(\frac{\partial \alpha_{\rho\sigma}}{\partial Q_k})_0 E_0 Q_{k0} \cos(\omega_1 + \omega_k)t$$

$$+ \frac{1}{2}(\frac{\partial \alpha_{\rho\sigma}}{\partial Q_k})_0 E_0 Q_{k0} \cos(\omega_1 - \omega_k)t \quad (2.17)$$

then we can name:

$$\alpha^{Ray} = (\alpha_{\rho\sigma})_0 \quad (2.18)$$

$$\alpha_k^{Ram} = \frac{1}{2}(\frac{\partial \alpha_{\rho\sigma}}{\partial Q_k})_0 E_0 Q_{k0} \quad (2.19)$$

Eq. (2.17) give you already a lot of informations: you find the three distinct frequencies, called ω_1, $(\omega_1 - \omega_k)$ and $(\omega_1 + \omega_k)$, where are created the induced dipole moments. The first scattered frequency corresponds to the Rayleigh scattering (elastic scattering), and it has the same value of the incident frequency, so the condition is that α^{Ray} be non-zero. We know and it is evident that every kind of molecule is polarizable to a greater or lesser extent, and the classical equilibrium polarizability tensor $(\alpha_{\rho\sigma})_0$ will always have some non-zero components and so α^{Ray} will be always non-zero. The results is that all molecules exhibit Rayleigh scattering. The other two frequencies are shifted to higher or lower frequencies and are consequently inelastic processes. The scattered light in these two events is called Raman scattering, with the shorter wavelength shifting (up-shifted frequency) referred to as anti-Stokes scattering, and the longer wavelength shifting (down-shifted frequency) referred to as Stokes scattering. In this cases, the indispensable requirement for Raman scattering associated with a molecular frequency ω_k is that α_k^{Ram} be non-zero. So you need that one of the components of the derived polarizability tensor is non-zero. In general, if we want reassuming, the vibrational displacement of atoms and therefore a particular vibrational mode lead to a change in polarizability[8].

2.4   Selection Rule for Fundamental Vibrations

Consider a diatomic molecule with maximum vibrational displacement Q_0. When the molecule is at maximum extension, the electrons are more readily displaced by an electromagnetic field due to the greater separation causing a lower influence from the other atom. Thus the polarizability is increased at the maximum bond length. . In the other case, when it is at maximal compression, the electrons of a given atom feel the effects of the other atom's nucleus and hence, they are not perturbed as much. Therefore the polarizability is minor for the minimum bond length. Fig. 2.2 shows how the behaviour of polarizabily as a function of displacemente near the point of equilibrium, for the case of a diatomic molecule. Meanwhile in the case of a linear and non-linear three-atomic molecule, we have a larger number of directions as shown in fig. 2.3 and fig. 2.4: In general classical theory gives the correct frequency dependence for Rayleigh scattering and vibrational Raman scattering. So it leads to good results of equilibrium dipole tensor $(\alpha_{\rho\sigma})_0$ and it can be used to extimate $(\frac{\partial \alpha_{\rho\sigma}}{\partial Q_k})_0$ only in the case of vibrational frequencies of very simple molecules. It cannot be applied to molecular rotations as classical theory can't provide the solution for specific discrete rotational frequencies to molecular systems. The results are that the classical polarizability tensors of the classical treatment can offer only a qualitative insight to the properties of molecules. In comparison, the quantum transition

FIGURE 2.2: Polarizzability of a diatomic A-B molecule as a function of vibrational displacement about equilibrium

FIGURE 2.3: Polarizability of a triatomic A-B-A molecule as a function of vibrational displacement about equilibrium

FIGURE 2.4: Polarizability of a triatomic non-linear A-B-A molecule
as a function of vibrational displacement about equilibrium

polarizability tensors can provide a quantitative understanding about fundamental
molecular properties and give a much deeper vision of the factors that characterize
Raman scattering. Also the classical amplitude Q_k is not very precise and has to be
replaced with a quantum mechanical amplitude.

2.5   Quantum Mechanical Treatment of Raman Scattering

In the quantum mechanical treatment of light-scattering phenomena, we treat the
interacting molecule in the material system quantum mechanically but continue to
treat the electromagnetic radiation classically. We shall be concerned in particular
with the allowed transitions between states of the molecule when it is under the per-
turbing influence of the incident radiation and the frequency-dependent multipole
transition moments associated with such transitions. The properties of the scattered
radiation can then be determined by regarding such frequency-dependent multi-
pole transition moments as classical multipole sources of electromagnetic radiation.
In the case of quantum mechanical picture the induced electric dipole of classical
theory is replaced by the transition electric dipole associated with a transition in the
molecule between two states: i, the initial state, and f the final state, that is the result
of the influence on the molecule by the incident electromagnetic radiation of fre-
quency ω_1 [7]. Hence, we write for the total induced transition electric dipole vector
an equation very similar to eq. 2.10 that was used for the classical treatment:

$$p_{fi}^{ind} = p_{fi}^{(1)} + p_{fi}^{(2)} + p_{fi}^{(3)} + \ldots \tag{2.20}$$

where $p_{fi}^{(1)}$ is linear in E, $p_{fi}^{(2)}$ is quadratic in E, $p_{fi}^{(3)}$ is cubic in E and so on.

In the same way of the classical treatment we study only the first grade term that takes this explicit form:

$$p_{fi}^{(1)} = (\tilde{p}_{fi}^{(1)}) + (\tilde{p}_{fi}^{(1)})^* \tag{2.21}$$

$$\tilde{p}_{fi}^{(1)} = \langle \Psi_f^{(1)} | \hat{p} | \Psi_i^{(0)} \rangle + \langle \Psi_f^{(0)} | \hat{p} | \Psi_i^{(1)} \rangle \tag{2.22}$$

where the $\Psi_f^{(0)}$ e $\Psi_i^{(0)}$ are the time-dependent unperturbed wave function of the initial of the initial and final states of the molecule, the $\Psi_f^{(1)}$ and the $\Psi_i^{(1)}$ the perturbed ones and $\hat{p}$ is the electric dipole moment operator. Then, the method for evaluating eq. 2.22 is as follows. The first thing that we need is the correlation between the perturbed time-dependent wave functions $\Psi_i^{(1)}$ and $\Psi_f^{(1)}$, and the unperturbed time-dependent wave functions $\Psi_i^{(1)}$ and $\Psi_f^{(0)}$ of the system. To find these relationships we have to make the following assumptions about the nature of the perturbation:

- First order perturbation

- Interaction hamiltonian for the perturbation is entirely electric dipole in nature

- Perturbation is produced by the time-dependent electric field associated with a plane monochromatic electromagnetic wave of frequency ω_1

At this point you can substitute $\Psi_i^{(1)}$ and $\Psi_f^{(1)}$ in eq. 2.22. Furthermore, you have to gather the resulting terms according to their wavelength dependence and identify the terms which coincide to Rayleigh and Raman radiation. If we want to preserve generality in the analysis of the incident electromagnetic radiation we must consider the el. field amplitudes to be complex. On the other hand, for the next steps of the treatment (to ease the calculations), we take the time-independent wave functions to be real. We need complex wave functions only in a few and rare cases, namely when we have to take in account the magnetic filed or the molecules have degenerate states. In general if we apply the quantum mechanics perturbation theory at the equation following The procedure we have just outlined we obtain for the ρ component of $\tilde{p}_{fi}^{(1)}$ for real wave functions[2]:

$$
\begin{aligned}
(p_\rho^{(1)})_{fi} = \frac{1}{2\hbar} \sum_{r \neq i} \Bigg\{ &\frac{\langle \psi_f | \hat{p}_\rho | \psi_r \rangle \langle \psi_r | \hat{p}_\sigma | \psi_i \rangle}{\omega_{ri} - \omega_1 - i\Gamma_r} \tilde{E}_{\sigma 0} exp[-i(\omega_1 - \omega_{fi})t] \\
&+ \frac{\langle \psi_f | \hat{p}_\rho | \psi_r \rangle \langle \psi_r | \hat{p}_\sigma | \psi_i \rangle}{\omega_{ri} + \omega_1 + i\Gamma_r} \tilde{E}_{\sigma 0}^* exp[i(\omega_1 + \omega_{fi})t] \Bigg\} \\
+ \frac{1}{2\hbar} \sum_{r \neq i} \Bigg\{ &\frac{\langle \psi_f | \hat{p}_\sigma | \psi_r \rangle \langle \psi_r | \hat{p}_\rho | \psi_i \rangle}{\omega_{rf} - \omega_1 - i\Gamma_r} \tilde{E}_{\sigma 0}^* exp[i(\omega_1 + \omega_{fi})t] \\
&+ \frac{\langle \psi_f | \hat{p}_\sigma | \psi_r \rangle \langle \psi_r | \hat{p}_\rho | \psi_i \rangle}{\omega_{rf} + \omega_1 + i\Gamma_r} \tilde{E}_{\sigma 0} exp[-i(\omega_1 - \omega_{fi})t] \Bigg\} \\
&+ complex \quad conjugate \tag{2.23}
\end{aligned}
$$

According to Placzek (1934) who call for a theorem made by Klein (1927), the terms in eq. 2.23 involving $(\omega_1 - \omega_{fi})$ describe the origination of Rayleigh and Raman scattering provided that $(\omega_1 - \omega_{fi}) > 0$. If ω_{fi} is negative, that is the final state is less energetic than the initial state, as in anti-Stokes Raman scattering, this requirement is always satisfied. In the same way, if ω_{fi} is zero, the solution is that the initial and final states have the same energy, and we are talking about Rayleigh scattering,

this requirements is always satisfied. If ω_{fi} is positive, that is the final state is more energetic than the initial state, as in Stokes Raman scattering, then the requirement $\hbar(\omega_1 - \omega_{fi}) > 0$, or equivalently $(\hbar\omega_1 > \hbar\omega_{fi}) > 0$ suggests that the energy of the irradiating light must be more than sufficient to reach the final state f from the initial state i. In the case of vibrational or rotational transitions which don't change the electronic state, if we take in account frequencies that are in the range of the visible or the ultraviolet spectrum, this condition is always satisfied. After making these assumptions, we can say that the Stokes and anti-Stokes Raman part of the ρ component of the real induced transition electric dipole moment can be write in this way:

$$(p_\rho^{(1)})_{fi} = \frac{1}{2\hbar} \sum_{r \neq i,f} \left\{ \frac{\langle f | \hat{p}_\rho | r \rangle \langle r | \hat{p}_\sigma | i \rangle}{\omega_{ri} - \omega_1 - i\Gamma_r} + \frac{\langle f | \hat{p}_\sigma | r \rangle \langle r | \hat{p}_\rho | i \rangle}{\omega_{rf} + \omega_1 + i\Gamma_r} \right\} \tilde{E}_{\sigma 0} exp(-i\omega_s t)$$

$$+ complex \quad conjugate \quad \text{(2.24)}$$

And knowing the relation between the polarizability tensor and the induced electric dipole from eq. (2.11):

$$(\alpha_{\rho\sigma})_{fi} = \frac{1}{\hbar} \sum_{r \neq i,f} \left\{ \frac{\langle f | \hat{p}_\rho | r \rangle \langle r | \hat{p}_\sigma | i \rangle}{\omega_{ri} - \omega_1 - i\Gamma_r} + \frac{\langle f | \hat{p}_\sigma | r \rangle \langle r | \hat{p}_\rho | i \rangle}{\omega_{rf} + \omega_1 + i\Gamma_r} \right\} \quad \text{(2.25)}$$

The outcomes of the quantum mechanical analysis are generally analogous in form to those obtained from the classical treatment described previously, but instead having a polarizzability and an oscillating el. dipole, we find a transition electric dipole and a polarizability tensor.

Unlike the classical polarizability, the quantum mechanical polarizability can describe in theory the properties of the molecules from the informations given from the scattered radiation because is defined in terms of wave functions and energy levels of the molecules. First, We discuss the frequency denominators $(\omega_{ri} - \omega_1 - i\Gamma_r)$ which appear in the first term of the transition polarizability $(\alpha_{\rho\sigma})_{fi}$ given by eq. (2.31). In achiving this equation there was no condition that $\hbar\omega_1$, the energy of a photon of the incident electromagnetic field, should bear any specific affiliation to any absorption energy $\hbar\omega_{ri}$ of the scattering molecule. Also, no requirements was made about the energies of the states $|r\rangle$. However, as shown in fig. 2.5 we have in two main possibilities that can help the calculations: first it is when the frequency of the exciting radiation ω_1 is very much smaller than any absorption frequency ω_{ri} of the molecule, that is $\omega_{ri} \gg \omega_1$ for all r. Then $\omega_{ri} - \omega_1 \approx \omega_{ri}$ for all states $|r\rangle$ and the Γ_r can be neglected because they are small relative to the ω_{ri}. In this case Here the system is represented as interacting with incident light of frequency ω_1 and making a transition from an initial stationary state $|i\rangle$ to a so-called virtual state and then to a final stationary state $|f\rangle$ with another transition. In particular we noted that the virtual state which isn't, as matter of fact, a stationary state of the system. Consequently we can say that doesn't belong to the set of solutions of a time-independent Schrödinger equation and so does not correspond to a well-defined value of the energy. This process, that is a case absorption without energy conservation, give rise to such a state is called virtual absorption. When $\omega_{ri} \approx \omega_1$ the Raman process is illustrated in fig. 2.5(c) and is called discrete resonance Raman scattering.Meanwhile, if $\hbar\omega_1$ is large enough to reach the dissociative continuum energy levels of the system the Raman process is illustrated in fig. 2.5(d) and is called continuum resonance Raman scattering. Instead, if we focus on the frequency denominator $(\omega_{fr} + \omega_1 + i\Gamma_r)$

in the second term of the transition polarizability $(\alpha_{\rho\sigma})_{fi}$ given by eq. (2.31) we find that, because is taken in account the sum of $\omega_f r$ and ω_1, this denominator doesn't become small and cannot lead to dominant terms in the sum over r. Consequently, when the first term in $(\alpha_{\rho\sigma})_{fi}$ has one or more dominant terms the other term will become relatively unimportant. Now it is very important to point out that the we expected in the event of resonance Raman scattering a very higher intensity with respect to normal Raman scattering because, as we know, when $\omega_{ri} \approx \omega_1$ the first term in the formula becomes very small, , but remains large if $\omega_{ri} \gg \omega_1$. To conclude, we can say the second term in the expression for $(\alpha_{\rho\sigma})_{fi}$ can be neglected in the resonance scattering except for stimulated emission which doesn't concern us here.

(a) Normal Raman scattering

$\omega_1 \ll \omega_{ri}$

(b) Pre-resonance Raman scattering

$\omega_1 \rightarrow \omega_{ri}$

(c) Discrete resonance Raman scattering

$\omega_1 \approx \omega_{ri}$

(d) Continuum resonance Raman scattering

ω_1 in range of dissociative continuum levels.
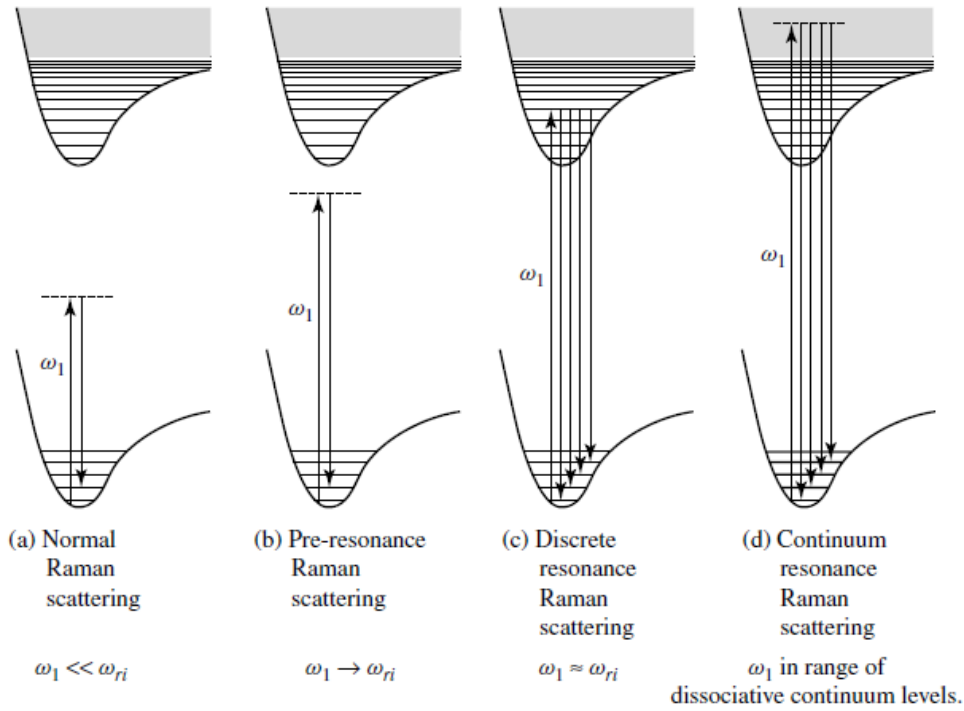
FIGURE 2.5: Four types of Raman Scattering processes

We specified in the introduction to this chapter that we need to introduce some simplifications to make the general formula for $(\alpha_{\rho\sigma})_{fi}$ more tractable. In this chapter and the subsequent ones we consider these modifications in some detail. Throughout the rest of this chapter we will consider the time-independent wave functions to be real. The first and fundamental step in solving the more general expression for $(\alpha_{\rho\sigma})_{fi}$ given by eq. (2.31) is to apply the adiabatic approximation (from Born and Oppenheimer, 1927) which enables the electronic and nuclear motions to be treated separately. We expand the notation for a general jth electronic–nuclear state so that its electronic, vibrational and rotational parts are represented by their respective quantum numbers e^j, v^j and R^j and write:

$$|j\rangle = \left|e^j v^j R^j\right\rangle \tag{2.26}$$

The Born–Oppenheimer, or adiabatic, approximation empower us to set:

$$|j\rangle = \left|e^j\right\rangle \left|v^j\right\rangle \left|R^j\right\rangle \tag{2.27}$$

for the state $|j\rangle$ and, for its energy,

$$\omega_{e^j v^j R^i} = \omega_{e^j} + \omega_{v^j} + \omega_{R^j} \tag{2.28}$$

The general state function is now a product of the discrete electronic, vibrational and rotational terms; and the energy is given by the separate electronic, vibrational and rotational parts. We now apply the Born–Oppenheimer approximation to eq. (2.31) by introducing equations (2.27) and (2.28). We express the outcome as:

$$(\alpha_{\rho\sigma})_{e^f v^f R^f : e^i v^i R^i} = \left\langle R^f\right| \left\langle v^f\right| \left\langle e^f\right| \hat{\alpha}_{\rho\sigma}(e^r, v^r, R^r) \left|e^i\right\rangle \left|v^i\right\rangle \left|R^i\right\rangle \tag{2.29}$$

Now the modifications we can make are effecting closure over the complete set of rotational states associated with each electronic/vibrational level, and this is possible for most of the practical situations where Raman scattering is observed under experimental conditions in which the rotational structure is not resolved, and setting $e^i = e^g$, so assuming that the initial state for the electron is in every case the ground state, so we assuming that the molecules are fully "relaxed". So the equation became:

$$(\alpha_{\rho\sigma})_{e^f v^f : e^g v^i} = \left\langle v^f\right| \left\langle e^f\right| \hat{\alpha}_{\rho\sigma}(e^r, v^r) \left|e^g\right\rangle \left|v^i\right\rangle \tag{2.30}$$

Now we have to consider two different methods. The first one is more radical, we introduce a number of quite profound approximations, more or less simultaneously, and obtain relatively simple results. This is the method developed by Placzek (1934). The other approach, require the introduction of the approximations in stages. This procedure is particularly precise for the treatment of resonance Raman scattering and electronic Raman scattering so we will use this second method. From the previous results:

$$(\alpha_{\rho\sigma})_{e^f v^f : e^g v^i} = \frac{1}{\hbar} \sum_{r \neq i, f} \left\{ \frac{\left\langle v^f\right| (p_\rho)_{e^f e^r} \left|v^r\right\rangle \left\langle v^r\right| (p_\sigma)_{e^r e^g} \left|v^i\right\rangle}{\omega_{e^r e^g} + \omega_{v^r v^i} - \omega_1 - i\Gamma_{e^r v^r}} \right.$$
$$\left. + \frac{\left\langle v^f\right| (p_\sigma)_{e^f e^r} \left|v^r\right\rangle \left\langle v^r\right| (p_\rho)_{e^r e^g} \left|v^i\right\rangle}{\omega_{e^r e^g} + \omega_{v^r v^i} + \omega_1 + i\Gamma_{e^r v^r}} \right\} \tag{2.31}$$

With:

$$(p_\rho)_{e^f e^r} = \left\langle e^f\right| \hat{p}_\rho \left|e^r\right\rangle \tag{2.32}$$

$$(p_\rho)_{e^r e^g} = \left\langle e^r\right| \hat{p}_\rho \left|e^g\right\rangle \tag{2.33}$$

For these last equations we have to take in account the slight dependence of the electronic transition moments on the normal coordinates of vibration Q_k which arises from the dependence of the Hamiltonian of the system itself. This process was first proposed by Herzberg and Teller (1933) and is called after them. So the electronic

transition dipoles become:

$$(p_\rho)_{e^f\prime e^r\prime} = (p_\rho)^0_{e^f e^r} + \frac{1}{\hbar} \sum_{e^s \neq e^r} \sum_k (p_\rho)^0_{e^f e^s} \frac{h^k_{e^s e^r}}{\omega_{e^r} - \omega_{e^s}} Q_k$$

$$+ \frac{1}{\hbar} \sum_{e^t \neq e^f} \sum_k (p_\rho)^0_{e^t e^r} \frac{h^k_{e^f e^t}}{\omega_{e^f} - \omega_{e^t}} Q_k \quad (2.34)$$

$$(p_\sigma)_{e^r\prime e^g\prime} = (p_\sigma)^0_{e^r e^g} + \frac{1}{\hbar} \sum_{e^s \neq e^r} \sum_k (p_\sigma)^0_{e^s e^g} \frac{h^k_{e^r e^s}}{\omega_{e^r} - \omega_{e^s}} Q_k$$

$$+ \frac{1}{\hbar} \sum_{e^t \neq e^g} \sum_k (p_\sigma)^0_{e^r e^t} \frac{h^k_{e^t e^g}}{\omega_{e^g} - \omega_{e^t}} Q_k \quad (2.35)$$

With $h^k_{e^a e^b}$ that is a coupling integral defined in this way:

$$h^k_{e^a e^b} = \langle \psi_{e^a}(Q_0) | (\partial \hat{H}_e / \partial Q_k)_0 | \psi_{e^b}(Q_0) \rangle \quad (2.36)$$

$(p_\sigma)_{e^r\prime e^g\prime}$ is visually shown in fig. 2.6. Instead, fig. 2.7 represent $(p_\rho)_{e^f\prime e^r\prime}$ When,
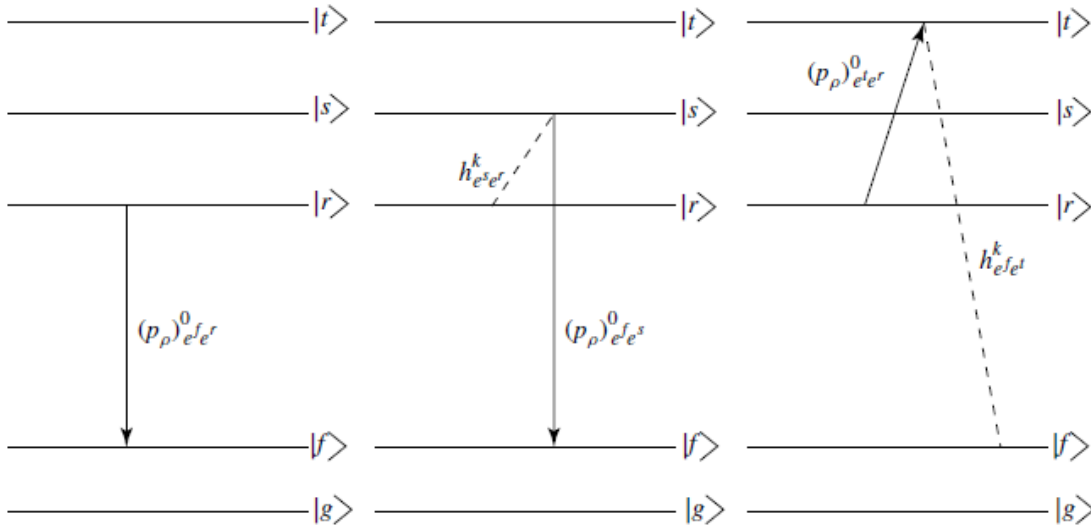
FIGURE 2.6: : The three contributions to (2.35) which arise from Herzberg-Teller coupling

in eq. (2.31), $(p_\rho)_{e^f e^r}$ is replaced by $(p_\rho)_{e^f\prime e^r\prime}$ using eq. (2.34), $(p_\rho)_{e^r e^g}$ is replaced by $(p_\rho)_{e^r\prime e^g\prime}$ using eq. (2.35) , a rather complicated result is obtained which we shall express in the form:

$$(\alpha_{\rho\sigma})_{e^f v^f : e^g v^i} = A^I + B^I + C^I + D^I \quad (2.37)$$

Furthermore, we can simplify these formulas somewhat because the electronic transition moments and the integral $h^k_{e^a e^b}$ do not, under the conditions for which the Born–Oppenheimer approximation is valid, work on the vibrational wavefunctions. Therefore we may separate the vibrational terms from the electronic terms (see Appendix) and write:

$$(\alpha_{\rho\sigma})_{e^f v^f : e^g v^i} = A^{II} + B^{II} + C^{II} + D^{II} \quad (2.38)$$
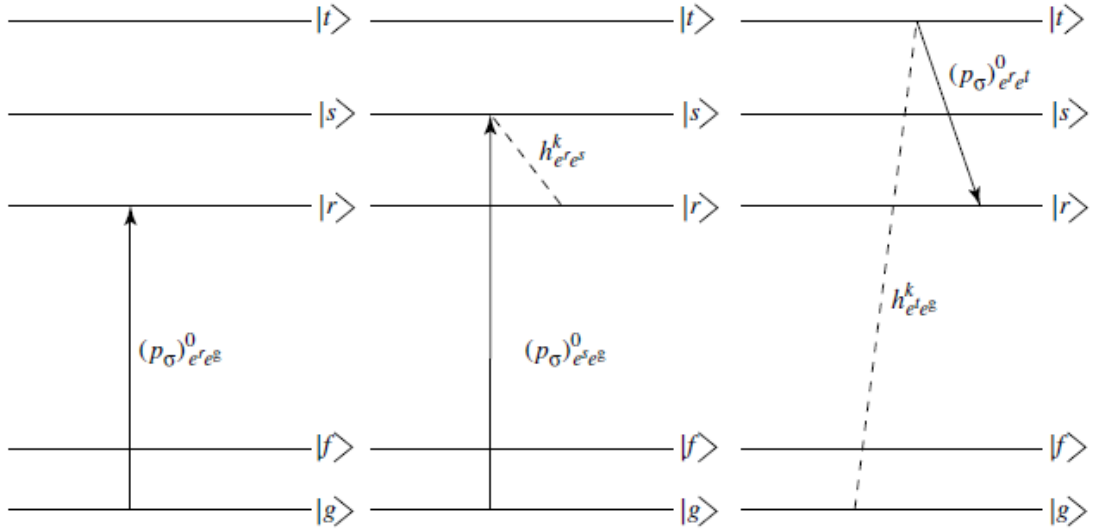
FIGURE 2.7: The three contribution to eq. (2.34) which arise from Herzberg-Teller coupling

2.5.1 Vibrational Raman Scattering

Further simplifications of eq. (2.38) are possible because we are interested only in pure vibrational Raman scattering for our purposes and equipment because Electronic Raman Scattering is prominent at very low frequencies (is difficult to divide from Rayleigh signal). So in our case $e^f = e^g$, and we can distinguish two preminent situations if we make specific assumptions regarding the relationship of the vibronic absorption frequencies $\omega_{e^r v^r:e^g v^i}$, or equivalently $\omega_{e^r e^g} + \omega_{v^r v^i}$, to ω_1 the frequency of the exciting radiation. . If the frequency of the exciting radiation is well removed from any electronic absorption frequencies, that is $\omega_{e^r e^g} + \omega_{v^r v^i} \gg \omega_1$ for all e^r and v^r we have non-resonance or normal vibrational Raman scattering. As a consequence, $\omega_{e^r e^g} + \omega_{v^r v^i} - \omega_1$ is insensitive to the $\omega_{v^r v^i}$ and may be substituted by $\omega_{e^r e^g} - \omega_1$. Also provided $\omega_1 \gg \omega_{v^r v^f}$, $\omega_{e^r e^f} + \omega_{v^r v^f} + \omega_1$ can be substituted by $\omega_{e^r e^f} + \omega_1$; this last simplification does not require that $\omega_{e^r e^f} \gg \omega_1$. Further, as $\omega_{e^r e^g} - \omega_1$ and $\omega_{e^r e^f} + \omega_1$ are now much larger than the damping factor $i\Gamma_{e^r v^r}$ that in this case may be neglected. An important consequence of these modifications in the frequency denominators is that closure over the set of vibrational states in each electronic state e^r becomes allowed because the denominators are not v^r dependent. As opposed to the resonance case which we consider later, a large number of excited electronic states $|s\rangle$ will contribute to the $B^I I$, $C^I I$ and $D^I I$ terms of eq. (2.38) through the matrix elements of the type $h^k_{e^a e^b}$ delineated in eq. (2.36). The relative magnitudes of these contributions cannot be easily estabilished and so it is more realistic in the non-resonance situation to use a less explicit equation than that used in eqs. (2.34) and (2.35). Therefore we can write:

$$(p_\rho)_{e^f{}'e^{r\prime}} = (p_\rho)^0_{e^f e^r} + \sum_k (p_\rho)^k_{e^f e^r} Q_k \tag{2.39}$$

Corresponding relationships for $(p_\sigma)_{e^f{}'e^{r\prime}}, (p_\rho)_{e^{r\prime}e^{g\prime}}$ and $(p_\sigma)_{e^{r\prime}e^{g\prime}}$ are easily given. We now introduce into eq. (2.38) the simplifications we have previously debated: the neglection of $\omega_{v^r v^i}$, $\omega_{v^r v^f}$ and the $i\gamma_{e^r v^r}$, closure over vibrational states, $e^f = e^g$ and The use of equations of the type (2.39) instead of eqs. (2.34) and (2.35). When these

conditions are introduced, eq. (2.38) is replaced by:

$$(\alpha_{\rho\sigma})_{v^f:v^i} = A^{III} + B^{III} + C^{III} + D^{III} \tag{2.40}$$

With:

$$A^{III} = \frac{1}{\hbar} \sum_{e^r \neq e^g} \left\{ \frac{(p_\rho)^0_{e^g e^r}(p_\sigma)^0_{e^r e^g}}{\omega_{e^r e^g} - \omega_1} + \frac{(p_\sigma)^0_{e^g e^r}(p_\rho)^0_{e^r e^g}}{\omega_{e^r e^g} + \omega_1} \right\} \tag{2.41}$$

$$B^{III} + C^{III} = \frac{1}{\hbar} \sum_{e^r \neq e^g} \sum_k \left\{ \frac{(p_\rho)^k_{e^g e^r}(p_\sigma)^0_{e^r e^g} + (p_\rho)^0_{e^g e^r}(p_\sigma)^k_{e^r e^g}}{\omega_{e^r e^g} - \omega_1} \right.$$
$$\left. + \frac{(p_\sigma)^0_{e^g e^r}(p_\rho)^k_{e^r e^g} + (p_\sigma)^k_{e^g e^r}(p_\rho)^0_{e^r e^g}}{\omega_{e^r e^g} + \omega_1} \right\} \langle v^f | Q_k | v^i \rangle \tag{2.42}$$

$$D^{III} = \frac{1}{\hbar} \sum_{e^r \neq e^g} \sum_{k,k'} \left\{ \frac{(p_\rho)^k_{e^g e^r}(p_\sigma)^{k'}_{e^r e^g}}{\omega_{e^r e^g} - \omega_1} + \frac{(p_\sigma)^{k'}_{e^g e^r}(p_\rho)^k_{e^r e^g}}{\omega_{e^r e^g} + \omega_1} \right\} \langle v^f | Q_k Q_{k'} | v^i \rangle \tag{2.43}$$

2.5.2 Vibrational Resonance Raman Scattering

Instead, if the excitation frequency lies within the contour of an electronic absorption band the approximations employed in the treatment of normal scattering are no longer valid. The dependence of the frequency denominator on the vibrational quantum numbers cannot be disregarded; the frequency difference $\omega_{e^r e^g} + \omega_{v^r v^i} - \omega_1$ is very small and proportional to the damping factor $i\Gamma_{e^r v^r}$ and so this factor cannot be ignored; and the explicit dependence of the first-order term in the Herzberg–Teller formulation on the excited states $|s\rangle$ must be taken into account. Nonetheless, further simplifications are possible. When ω_1 reaches some particular electronic absorption frequency $\omega_{e^r e^g} + \omega_{v^r v^i}$, the excited electronic state involved will dominate the summation over states in the expression for the transition polarizability. It is then generally adequate to consider one or at most two electronic manifolds in the analysis of Raman scattering in the case of resonance. Another important thing is that under resonant conditions, only the first term in each of eqs. A^{II}, B^{II}, C^{II} and D^{II} can be significant. The second term contributes only a slowly varying background and may be disregarded. Therefore, we can restrict the summation over vibrational states to one sum over the states $\left| v^{r(r)} \right\rangle$; and we must contemplate coupling of the resonant electronic state $|e^r\rangle$ to only one excited electronic state, $|e^s\rangle$ in the B^{IV} terms and $|e^t\rangle$ in the C^{IV} terms, and only two excited states $|e^s\rangle$ and $\left| e^{s'} \right\rangle$ where s and s' could be the same) in the D^{IV} terms. In the same way we can restrict the sum to a single normal coordinate Q_k in the B^{IV} and C^{IV} terms and a pair of normal coordinates Q_k and Q_k' (where k and k' may be equal) in the D^{IV} term. Results are:

$$(\alpha_{\rho\sigma})_{v^f:v^i} = A^{IV} + B^{IV} + C^{IV} + D^{IV} \tag{2.44}$$

$$A^{IV} = \frac{1}{\hbar}(p_\rho)^0_{e^g e^r}(p_\sigma)^0_{e^r e^g} \sum_{v^r_k} \frac{\langle v^{f(g)}_k | v^{r(r)}_k \rangle \langle v^{r(r)}_k | v^{i(g)}_k \rangle}{\omega_{e^r v^r_k : e^g v^i_k} - \omega_1 - i\Gamma_{e^r v^r_k}} \tag{2.45}$$

$$B^{IV} = \frac{1}{\hbar^2}(p_\rho)^0_{e^g e^s} \frac{h^k_{e^s e^r}}{\omega_{e^r} - \omega_{e^s}} (p_\sigma)^0_{e^r e^g} \sum_{v^r_k} \frac{\left\langle v^{f(g)}_k \middle| Q_k \middle| v^{r(r)}_k \right\rangle \left\langle v^{r(r)}_k \middle| v^{i(g)}_k \right\rangle}{\omega_{e^r v^r_k : e^g v^i_k} - \omega_1 - i\Gamma_{e^r v^r_k}}$$

$$+ \frac{1}{\hbar^2}(p_\rho)^0_{e^g e^r} \frac{h^k_{e^r e^s}}{\omega_{e^r} - \omega_{e^s}} (p_\sigma)^0_{e^s e^g} \sum_{v^r_k} \frac{\left\langle v^{f(g)}_k \middle| v^{r(r)}_k \right\rangle \left\langle v^{r(r)}_k \middle| Q_k \middle| v^{i(g)}_k \right\rangle}{\omega_{e^r v^r_k : e^g v^i_k} - \omega_1 - i\Gamma_{e^r v^r_k}} \quad (2.46)$$

$$C^{IV} = \frac{1}{\hbar^2} \frac{h^k_{e^g e^t}}{\omega_{e^g} - \omega_{e^t}} (p_\rho)^0_{e^t e^r}(p_\sigma)^0_{e^r e^g} \sum_{v^r_k} \frac{\left\langle v^{f(g)}_k \middle| Q_k \middle| v^{r(r)}_k \right\rangle \left\langle v^{r(r)}_k \middle| v^{i(g)}_k \right\rangle}{\omega_{e^r v^r_k : e^g v^i_k} - \omega_1 - i\Gamma_{e^r v^r_k}}$$

$$+ \frac{1}{\hbar^2}(p_\rho)^0_{e^g e^r}(p_\sigma)^0_{e^r e^t} \frac{h^k_{e^t e^g}}{\omega_{e^g} - \omega_{e^t}} \sum_{v^r_k} \frac{\left\langle v^{f(g)}_k \middle| v^{r(r)}_k \right\rangle \left\langle v^{r(r)}_k \middle| Q_k \middle| v^{i(g)}_k \right\rangle}{\omega_{e^r v^r_k : e^g v^i_k} - \omega_1 - i\Gamma_{e^r v^r_k}} \quad (2.47)$$

$$D^{IV} = \frac{1}{\hbar^3}(p_\rho)^0_{e^g e^s} \frac{h^k_{e^s e^r} h^{k'}_{e^r e^{k'}}}{(\omega_{e^r} - \omega_{e^s})(\omega_{e^r} - \omega_{e^{s'}})} (p_\sigma)^0_{e^{s'} e^g} \sum_{v^r_k, v^r_{k'}} \frac{\left\langle v^{f(g)}_k \middle| Q_k \middle| v^{r(r)}_k \right\rangle \left\langle v^{r(r)}_{k'} \middle| Q_{k'} \middle| v^{i(g)}_{k'} \right\rangle}{\omega_{e^r v^r_k : e^g v^i_k} - \omega_1 - i\Gamma_{e^r v^r_k}}$$
$$(2.48)$$

In these equations the exclusions $|e^r\rangle \neq |e^g\rangle$, $|e^s\rangle \neq |e^r\rangle$, $\left|e^{s'}\right\rangle \neq |e^r\rangle$ and $|e^t\rangle \neq |e^g\rangle$ apply, and an additional sign has been introduced on the vibrational quantum numbers which appear in the numerators to underline to which electronic state they belong. Hence, the symbols $v_{k^{i(g)}}$ and $v_{k^{f(g)}}$ imply that the initial and final state vibrational quantum numbers v_{k^i} and v_{k^f} respectively associate to the ground electronic state $|e^g\rangle$. Equally, symbols such as $v_{k^{r(r)}}$ and $v_{k^{r(s)}}$ imply that the intermediate state vibrational quantum number v^i_k associate to the intermediate electronic states $|e^r\rangle$ and $|e^s\rangle$ respectively with the exclusion that $r, s \neq g$. The C^{IV} term which is formulated in eq. (2.47) involves the vibronic coupling of the ground electronic state $|e^g\rangle$ to an excited electronic state $|e^t\rangle$. In the case of a large energy separation between the ground electronic state and the excited electronic states this term is likely to be trivial and we shall not consider it further. The D^{IV} term which is delineated in eq. (2.48) relates the vibronic coupling of the excited electronic state $|e^r\rangle$ to two other excited electronic states $|e^s\rangle$ and $|e^{s'}\rangle$. This term is likely to be very small and will also not be considered further.

For the A^{IV} term to be non-zero, two conditions must be satisfied. Both the transition dipole moments $(p_\rho)^0_{e^g e^r}$ and $(p_\sigma)^0_{e^r e^g}$ which emerge as a product must be non-zero; and the multiplication of the vibrational overlap integrals, $\langle v^{f(g)}_k | v^{r(r)}_k \rangle$ and $\langle v^{r(r)}_k | v^{i(g)}_k \rangle$, must also be non-zero for at least one $v^{r(r)}_k$ value. The first condition is unequivocal. It plainly orders the resonant electronic transition to be electric-dipole allowed. For strong scattering the transition dipole moments that we are taking in account should have appreciable magnitudes. So the excitation within the contour of an intense absorption band, as for example a band arising from a charge transfer mechanism or a $\pi^* - \pi$ transition, would be favourable.Instead, excitation within the contour of a weak band, like one resulting from a ligand-field or spin-forbidden transition, would not be able to generate a considerable A^{IV} term. We now examine the second condition, shrinking the discussion to the case of harmonic potential functions. In the case of orthogonal vibrational wave functions, the vibration overlap integrals , $\langle v^{f(g)}_k | v^{r(r)}_k \rangle$ and $\langle v^{r(r)}_k | v^{i(g)}_k \rangle$ are zero unless $v^{f(g)}_k = v^{r(r)}_k$ and

$v_k^{r(r)} = v_k^{i(g)}$ and thus, there is no contribution from the A^{IV} term to Raman scattering. Still, if non-orthogonal vibrational wave functions are included the A^{IV} term can be non-zero. For any one vibrational mode of a molecule, namely the kth vibrational mode, non-orthogonality can arise in two manners. The first of these is if for the kth mode its classical vibration frequency is not equal in the electronic states $|e^g\rangle$ and $|e^r\rangle$, that is $\omega_k^r \neq \omega_k^g$. We find this difference if the shape of the potential energy surface is not the same in the two electronic states. The second case of non-orthogonality arise if there is a displacement ΔQ_k of the potential energy minimum along the normal coordinate Q_k as between the electronic states $|e^g\rangle$ and $|e^r\rangle$. If $\omega_k^r \neq \omega_k^g$ and $\Delta Q_k = 0$ the situation is illustrated in Fig. 2.8.
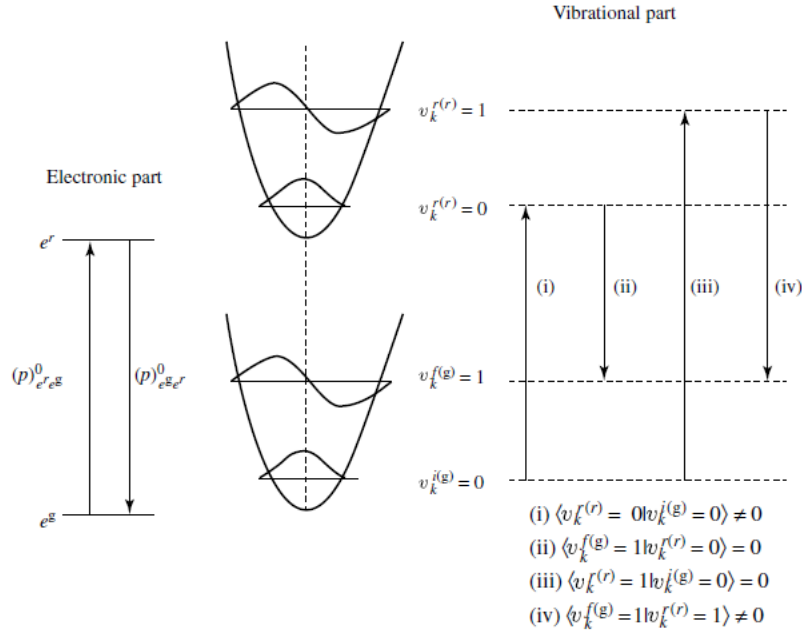
FIGURE 2.8: A case of dipole electronic transitions and vibrational overlap integrals involved in AIV

Instead, fig. 2.9 shows the case in which $\omega_k^r \neq \omega_k^g$ and $\Delta Q_k \neq 0$: Nevertheless, if the magnitude of ΔQ_k is large enough, the multiplication of the vibrational overlap integrals $\langle v_k^{f(g)}|v_k^{r(r)}\rangle$ and $\langle v_k^{r(r)}|v_k^{i(g)}\rangle$ may have significant magnitudes not only for transitions from $v_k^{i(g)} = 0$ to $v_k^{f(g)} = 0$ but also for transitions from $v_k^{i(g)} = 0$ to $v_k^{f(g)} = 2, 3, 4, 5, \ldots$ Concluding, the A^{IV} term can produce overtones in the resonance Raman spectrum with intensities proportional to that of the fundamental.

The B^{IV} term as written in eq. (2.46) relates the vibronic coupling of the resonant excited state $|e^r\rangle$ to one other excited state $|e^s\rangle$. We take in account first the vibronic coupling integrals which for convenience we now write as $h_{e^s e^r}^k / \Delta\omega_{e^r e^s}$ and $h_{e^r e^s}^k / \Delta\omega_{e^s e^r}$ where $\Delta\omega_{e^r e^s} = \omega(e^r) - \omega(e^s)$. The term $h_{e^s e^r}^k / \Delta\omega_{e^r e^s}$ is a measure of the strength of vibronic coupling of the states $|e^r\rangle$ and $|e^r\rangle$ along the normal coordinate Q_k. One important thing we have to notice is that the Herzberg–Teller expansion is only valid for weak vibronic coupling, i.e. within the framework of the adiabatic Born–Oppenheimer approximation. At the of the day we study the products of vibrational transition integrals and overlap integrals, specifically $\left\langle v_k^{f(g)} \middle| Q_k \middle| v_k^{r(r)} \right\rangle \langle v_k^{r(r)}|v_k^{i(g)}\rangle$ and $\langle v_k^{f(g)}|v_k^{r(r)}\rangle \left\langle v_k^{r(r)} \middle| Q_k \middle| v_k^{i(g)} \right\rangle$. In the harmonic approximation for Q_k', $\left\langle v_k^{f(g)} \middle| Q_k \middle| v_k^{r(r)} \right\rangle$
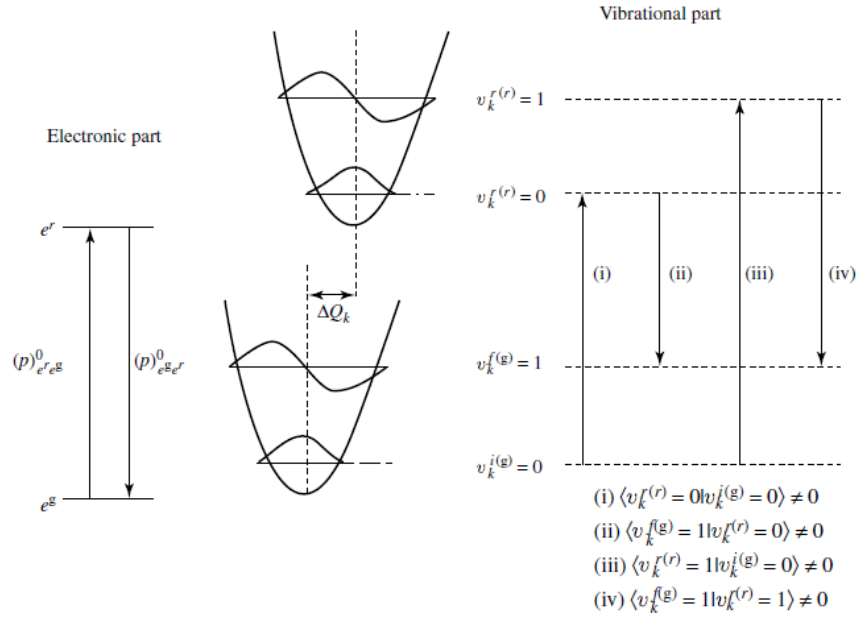
FIGURE 2.9: A different case of dipole electronic transitions and vibrational overlap integrals involved in AIV

is non-zero only if $v_k^{f(g)} = v_k^{r(r)} + 1$ and $\left\langle v_k^{r(r)} \middle| Q_k \middle| v_k^{i(g)} \right\rangle$ is non-zero only if $v_k^{r(r)} = v_k^{i(g)} + 1$. If we consider only diagonal vibrational overlap integrals, that is those for which $v_k^{r(r)} = v_k^{i(g)}$ and $v_k^{f(g)} = v_k^{r(r)}$, the multiplications of the vibrational transition integrals and overlap integrals are non-zero only if $v_k^{f(g)} = v_k^{r(r)} + 1$. If upper vibrational levels of the kth mode are empty, a case usually described as the low temperature limit, then $v_k^{i(g)} = 0_k^{i(g)}$ and $v_k^{f(g)} = 1_k^{f(g)}$ so that only two such products contribute. If we insert the values of the vibrational quantum numbers explicitly and also give them electronic state sign labels, the two contributing products take the forms $\left\langle 1_k^{f(g)} \middle| Q_k \middle| 0_k^{r(r)} \right\rangle \langle 0_k^{r(r)} | 0_k^{i(g)} \rangle$ and $\langle 1_k^{f(g)} | 1_k^{i(g)} \rangle \left\langle 1_k^{r(r)} \middle| Q_k \middle| 0_k^{i(g)} \right\rangle$. The equation for B^{IV} term now assumes the following distinct shape which contains only two terms:

$$\alpha^{\mathrm{B^{IV}}}_{e^g 1_k^f : e^g 0_k^i} = \frac{1}{\hbar^2} (p_\rho)^0_{e^g e^s} \frac{h^k_{e^s e^r}}{\Delta \omega_{e^r e^s}} (p_\sigma)^0_{e^r e^g} \frac{\left\langle 1_k^{f(g)} \middle| Q_k \middle| 0_k^{r(r)} \right\rangle \langle 0_k^{r(r)} | 0_k^{i(g)} \rangle}{\omega_{e^r 0_k^r : e^g 0_k^i} - \omega_1 - i\Gamma_{e^r 0_k^r}}$$

$$+ \frac{1}{\hbar^2} (p_\rho)^0_{e^g e^r} \frac{h^k_{e^r e^s}}{\Delta \omega_{e^r e^s}} (p_\sigma)^0_{e^s e^g} \frac{\langle 1_k^{f(g)} | 1_k^{r(r)} \rangle \left\langle 1_k^{r(r)} \middle| Q_k \middle| 0_k^{i(g)} \right\rangle}{\omega_{e^r 1_k^r : e^g 0_k^i} - \omega_1 - i\Gamma_{e^r 1_k^r}} \quad (2.49)$$

The further application of eq. (2.44) inevitably implicate consideration of the symmetry of the scattering molecule and of its vibrations and you have to apply group theory [1]. We can distinguish three important cases: molecules with only one and totally symmetric mode of vibrations, molecules with a few totally symmetric mode of vibrations and molecules with non-totally simmetric mode of vibrations.
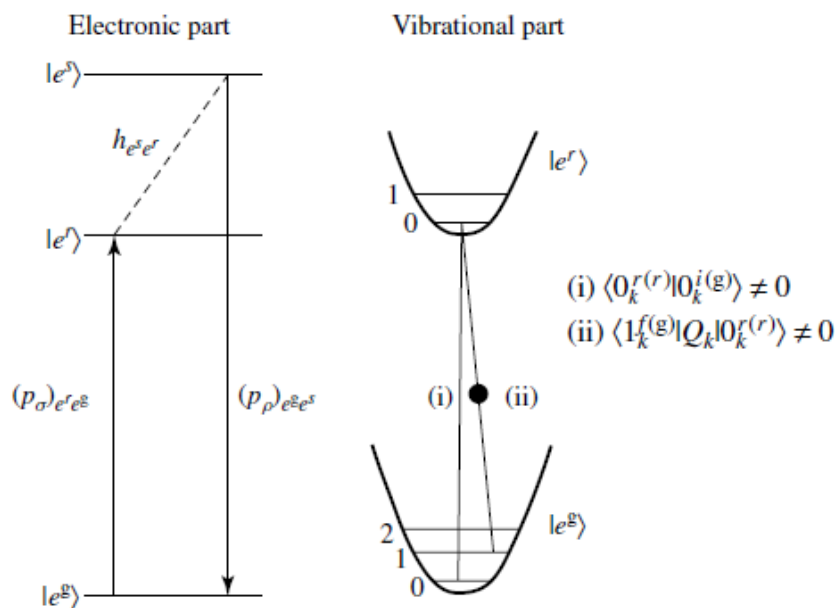
FIGURE 2.10: 0-0 resonant vibronic transition
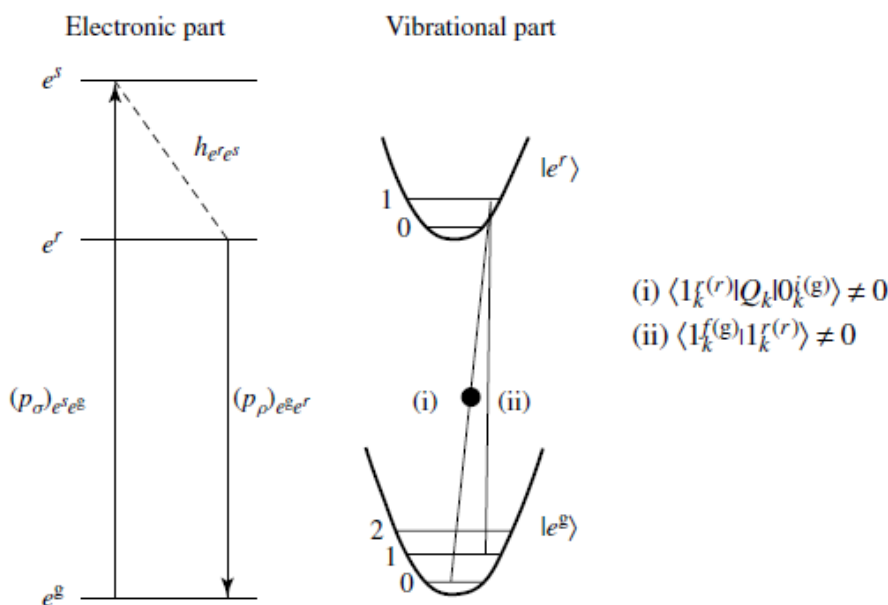
FIGURE 2.11: 1-0 resonant vibronic transition

2.6 Applications of Raman Spectroscopy

An application that is now assuming considerable importance is the use of vibrational Raman spectra solely for the identification of molecular species. Until relatively recently Raman spectra could only be obtained from appreciable amounts of materials and these had to be free from fluorescent contaminants. Thus analytical applications were very limited. However the situation has now been transformed

completely by quite dramatic advances in the techniques available for exciting, detecting and recording Raman spectra. As a result vibrational Raman spectra can now be obtained from minute amounts of material in almost any condition or environment. Raman spectra can be obtained from particular points in a sample and it is possible, for example, to construct maps of the amount of a particular species across a surface.

2.6.1   Diamond

Diamond has a characteristic peak at 1332 cm-1 that is the result of the vibration of its lattice, composed by cell of two units and sp3-sp3 bond (7.02 eV).
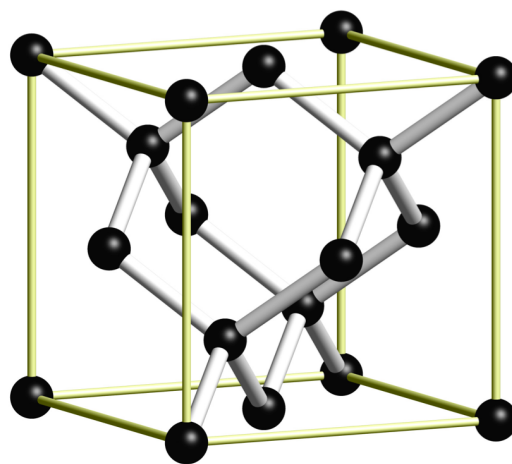
FIGURE 2.12: Lattice structure of diamond
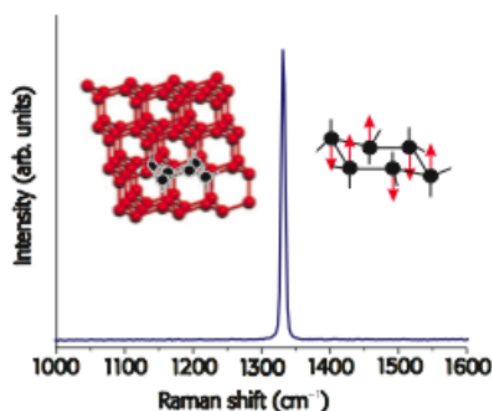
FIGURE 2.13: Raman Spectrum of Diamond

2.6.2   Hexagonal Diamond

Lonsdaleite or hexagonal diamond is an allotrope of carbon. It can be found in nature only when a meteorite containing graphite strikes the Earth. It has the peculiarity of maintaining a hexagonal graphite lattice structure composed by stack of

"chair like" atomic plan staps containing only sp3 sites. The sp3-sp3 bonds are less energetic with respect to the pure diamond ones (7.015 eV) and this is reflected on corresponding Raman spectra that shows the dowshifted value of less then 10 cm-1 (=1325 cm-1) for the main D peak[12].
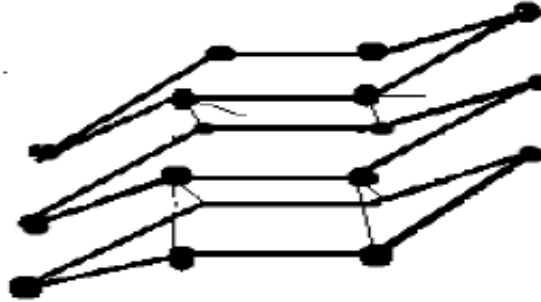
FIGURE 2.14: Lonsdaleite "chair like" lattice structure

2.6.3 Graphite and Graphene

Graphite is with diamond the principal crystalline allotrope of carbon. It has layered and planar structure The individual layers are called graphene. In each layer, the carbon atoms are hybridized sp2 and they are arranged in a honeycomb lattice with separation of 0.142 nm, and the distance between planes is 0.335 nm.
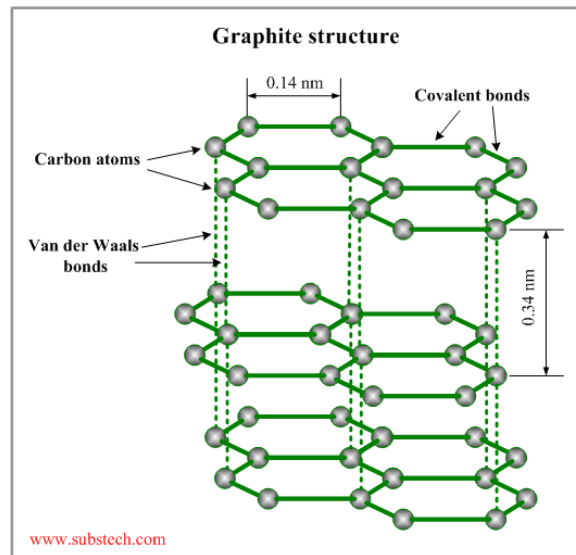
FIGURE 2.15: Graphite lattice structure

The phonon dispersion, of graphene plays a very important role in interpreting their Raman spectra. In graphene the unit cell is composed by 2 atoms, consequently six phonon dispersion modes as shown in Fig. 2.16 out of which three are acoustic (A) and three are optical (O) phonon modes. In the case of both acoustic and optical modes we have out-of plane (Z) phonon mode and the other two are in-plane modes, one longitudinal (L) and the last one transverse (T). Therefore, starting from the
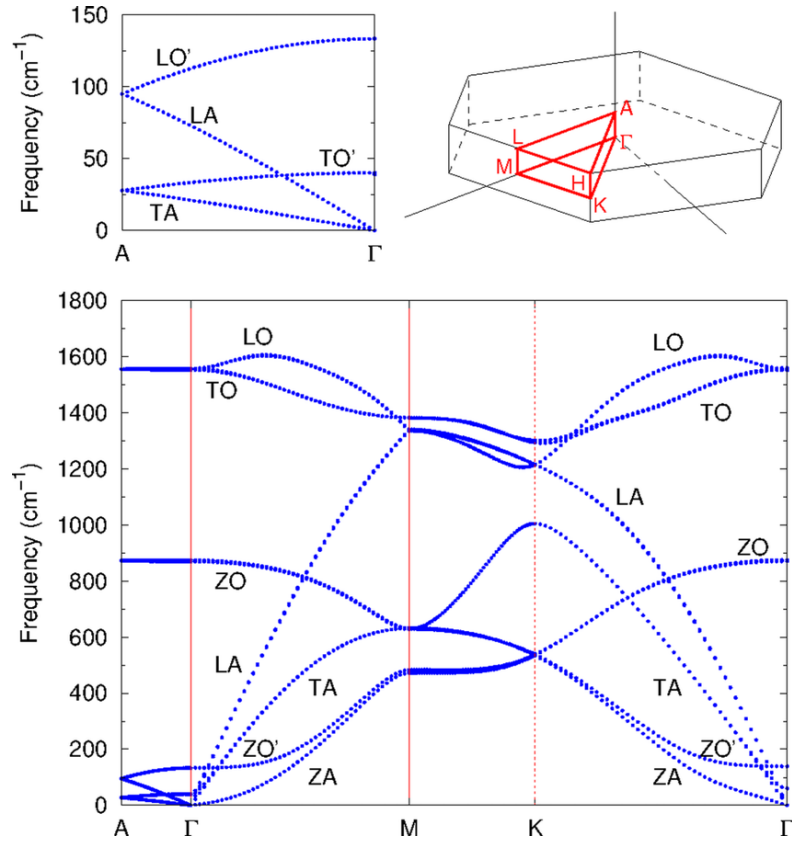
FIGURE 2.16: Graphite Phonon Dispersion

highest energy at the Γ point in the Brillouin zone the various phonon modes are named as LO, TO, ZO, LA, TA and ZA as seen in fig. 2.16.

The most interesting phonons are the optical ones in the zone-center (Γ) and zone edge (*K* and *K'*) region, considering they are accessible by Raman spectroscopy. The Γ point optical phonons are doubly degenerate with E2g symmetry for unperturbed graphene. The vibrations coincide to the rigid relative dislocation of the A and B sub-lattices. This phonon mode is Raman active and accountable for the Raman G mode in graphene. The LO phonon branch in the proximity of the Γ point is not Raman active in a one phonon process in defect free graphene, since that it has finite wave vector. Nevertheless, when there are some defects in the lattice, it can be activated. Like the LO phonons near the Γ point, the TO phonon branch in the proximity of the zone edge is accessible by a two-phonon Raman process, which gives rise to the G' (also named 2D) mode.

The most intense attributes in the Raman spectrum of monolayer graphene are the so-called G band appearing at 1582 cm-1 and the 2D band at about 2700 cm-1 using laser radiation at 2.41 eV. Instead, if we have a disordered sample or we're looking at the edge of a graphene sample, we can also see the so-called disorder-induced D-band (or GeA), at around half of the wavelenght of the 2D band (around 1350 cm-1 using laser excitation at 2.41 eV). The G-peak in the first-order Raman spectrum, coincides to the optical mode vibration of two adjacent carbon atoms on a sp2-hybridized graphene layer. There is a perpendicular stretching of the σ bonds along the plane generating the Raman G peak, which is one phonon intra-valley scattering process at the Γ point. The double-resonance (DR) process that seen in the center and right side of fig. 2.18 begins with an electron of wave-vector k around K
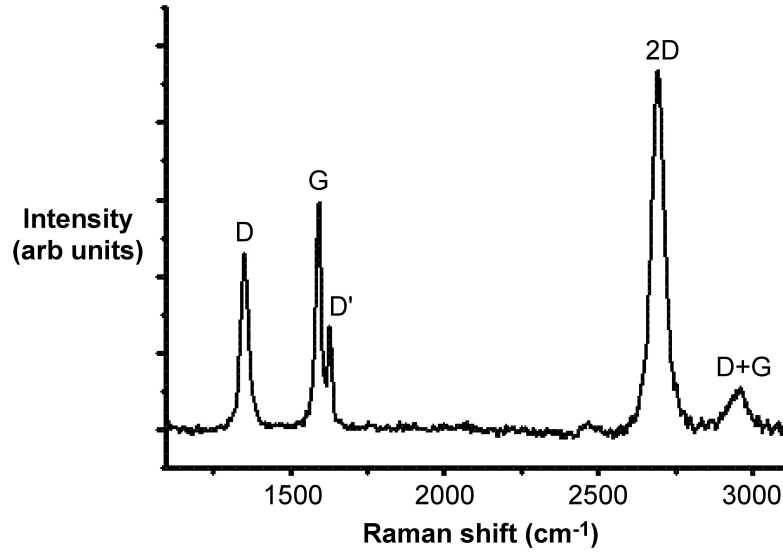
FIGURE 2.17: Example of a Graphene Raman Spectrum
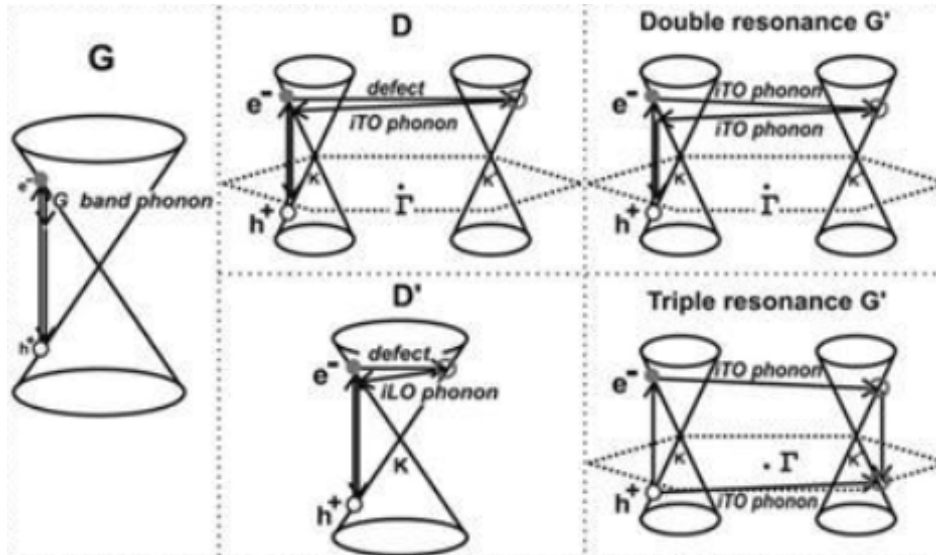
FIGURE 2.18: Phonon processes in Graphite and Graphene

absorbing a photon of the laser source[9].Then, the electron is inelastically scattered by a phonon or a defect of wavevector q and energy equal to kinetic energy of the photon to a site near around the K point, with wavevector k+q.Subsequently, the electron is then scattered back to a k state, and radiates a photon by recombining with a hole at a k point. Instead, if we are talking aboutIn the G'-band (in our case is called 2D), both processes are inelastic scattering events and two phonons are required. The triple-resonance process can happen by both scattering of electrons and holes and the recombination takes place at the inequivalent K' point with respect to K point with a photon emission as result. In the case of the D band, the general belief was that the two scattering processes consist of one elastic scattering event by defects of the crystal and one inelastic scattering event by emitting or absorbing a phonon, and consequently the 2D was considered its overtones. Recent studies, [11], shows

that it is implausible the relation with the defects of the crystal but instead the peak is due to the edges of the lattice. It is important focus on edges, because their chirality determines the electronic properties. The edge can be formed by carbon atoms organized in the zigzag or armchair configuration as shown in Fig. 2.19 . Zigzag edges are made of carbon atoms that all belong to one and the same sublattice, while the armchair edges contain carbon atoms from either sublattice. For a zigzag edge the momentum can only be transferred in a direction dz which does not allow the electron to return to the original valley in reciprocal space as seen in Fig. 2.19 . Therefore zigzag edges don't give rise to D peak in Raman spectroscopy. In graphene with defect free edges, if two edges make an angle of 120°, they should be the same. In contrast, Coupled Double Resonance Raman scattering conditions are fulfilled on A edge bonds that are simmetric to in-plane K phonon.
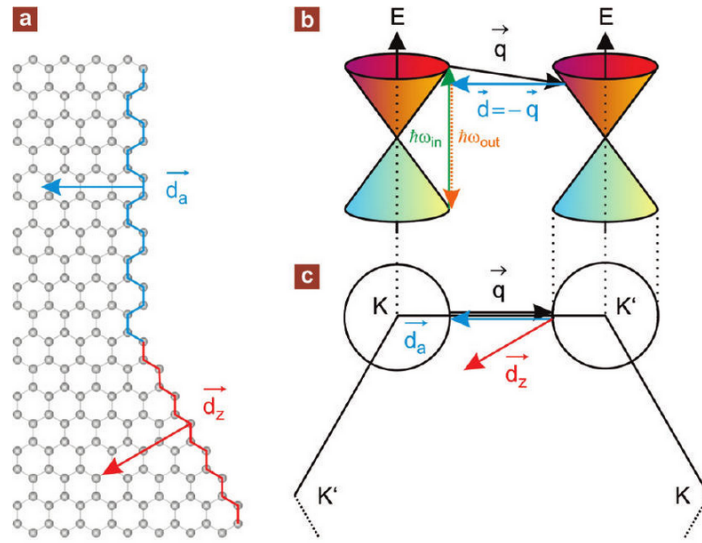
FIGURE 2.19: Raman Double Resonance mechanism at the edges

The most important characteristics of G' (also called 2D) like position, line width and intensity depend on the number of layers 'n' of the graphene layer, as seen in Fig. 2.20. This is due to the evolution of the bands of the mono-layer, bi-layer and few-layer graphene formations. These features can be used to describe the number of graphene layers 'n' in few layer graphene specimen [4]. The G' band for 1-LG at room temperature shows a single Lorentzian or Gaussian feature (symmetric peak). For bilayer graphene with Bernal AB layer stacking, both the electronic and phonon bands split into two elements. Four different DR processes can occur in bilayer case. Therefore a Raman spectrum of a bilayer graphene specimen with AB stacking can be fitted with four Lorentzians or Gaussians. Using group theory method for a 3-LG, the number of permitted Raman peaks in the G' band become fifteen. The high frequency side of the G' band begins to dominate starting from 4-LG to HOPG as seen in Fig. 2.20. The G' band is a convolution of peaks along the entire kz axis.

The recognition of the number of layers by Raman spectroscopy is well known only for graphene specimen with AB Bernal stacking. Instead, if we take the example of randomly rotation stacking like turbostratic graphite, Raman shows a G' band that is a single Lorentzian or Gaussian as in monolayer graphene but with a larger Full Width Half Maximum and much smaller ratio of IG' versus IG. This is coming from the missing of an interlayer interaction between the graphene planes. Recently,
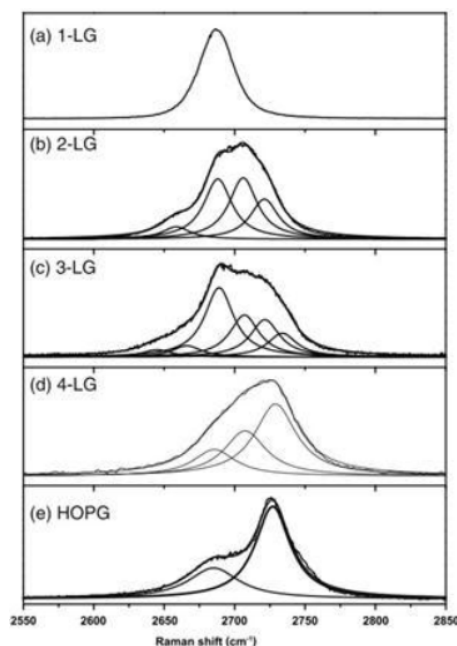
FIGURE 2.20: The measured G′ band with 2.41 eV laser energy for one, two, three and four layer graphene and HOPG

Intravalley R′ peak with center at around 1625 cm-1 is recognized in randomly produced bilayer graphene due to a rotational-induced intervalley Double Resonance scattering. Its features are due on the mismatch rotation angle and can be used as an optical label for superlattices in bilayer graphene.

2.6.4 Amorphous Carbons

Amorphous Carbon materials are very versatile and very variegated and their peculiar properties depends mainly on the ratio of sp2 (graphite-like) to sp3 (diamond like) bond. There are many types of sp2 bonded carbons with various degrees of graphitic ordering, varying from micro-crystalline graphite to glassy carbon. In general, an amorphous carbon can display any combination of sp3, sp2 and even sp1 sites, with the ulterior possibility of showing some traces of hydrogen and nitrogen [3]. This is shown very clearly in fig. 2.21

2.6.5 Single-Wall Carbon Nanotubes

Carbon nanotubes have exceptional electrical, mechanical, magnetic and even optical properties, which make them a suitable contender for use in various applications such as solar cells, memory devices, conductive composites, hydrogen and energy storages, fuel cells, and super capacitors, but this is only a portion of the possible uses. They are cylindrical tubes formed by sp2 bonded carbon atoms. A CNT is basically a roll of graphene planar sheet so-called single-wall CNT(SWCNT). They can shows well delineated narrow "G" Raman peaks and a sharp GeA peak corresponding to vacancies. For such Raman spectrum, no aliphatic bands are noticed and only some weak C5/C7 bands between the G and the GeA peak, suggesting some well defined armchair type edge on internal edges of vacancies.
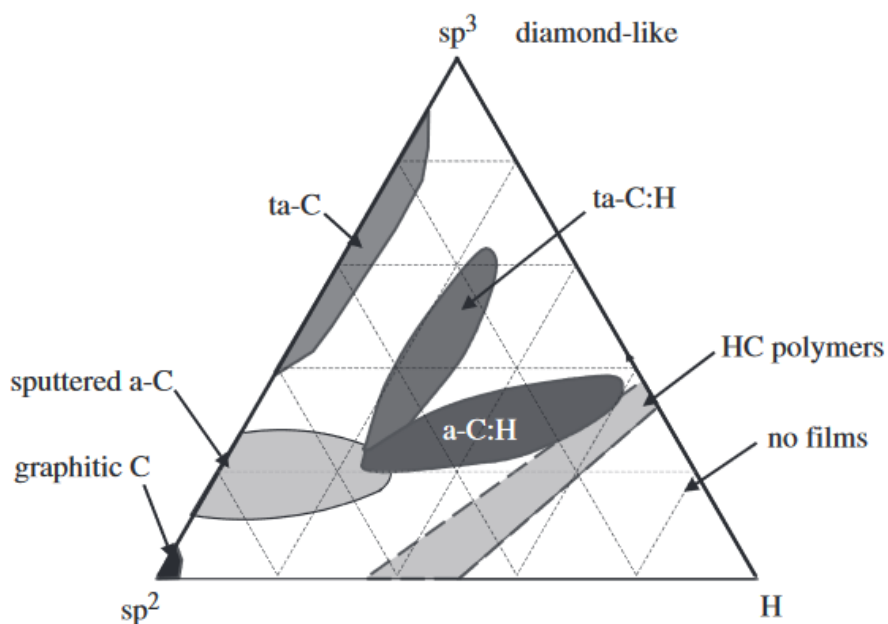
FIGURE 2.21: Ternary phase diagram of amorphous carbons. The three corners correspond to diamond graphite and hydrocarbons, respectively
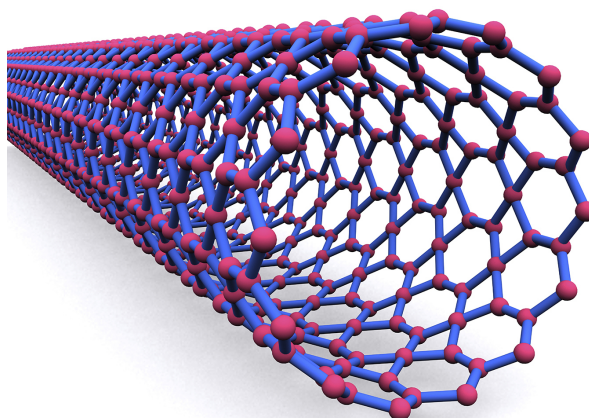
FIGURE 2.22: Schematic visualization of a SWCNT

2.6.6   Carbon Nanofibers

Carbon Nanofibers (CNF) are discontinous filaments of disordered material which is known to contain mainly sp2 hybridized carbons and some traces of sp3 carbon [14]. They exibhit a sort broader "D" and "G" bands than for graphene what confirm the disorder, the existence of vacancies and voids with disordered internal edges GeA band, similar to CNT but broader according to the higher level of disorder in this material. However the G band appears to be somewhat upshifted, the D band is observed at the expected and theoretical frequency of around 1330 cm-1. If you take in account the precise features of the spectrum, in addition to the main D and G band, we can see some broad DG and GG aliphatic bands, C5/C7 rings band and a Dd
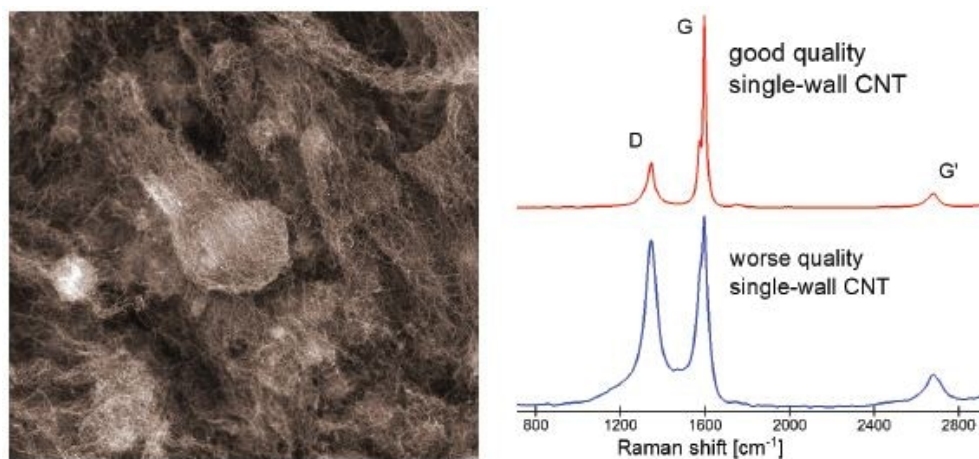
FIGURE 2.23: At left, an image of CNTs (photo taken by SEM). At right raman spectra of two different CNTs.

band probably due to some disordered diamond phase. CNF can be obtained with a wide variety of methods but in every case you have to use CVD, usually at low pressure and lower temeperatures wih respect to the fabrication of single wall carbon nanotubes. The high amount of internal carbon hybridized sp3 in contrast with the composition of CNT could be obtained by a disordered hexagonal diamondlike H6 analog to the interfacing material structure between the hexagonal graphene surface layers and a diamondlike cubic SiC substrate after high temperature treatment. Thus, the so-labelled Ddisorder band or GeA band is in fact a superposition of a disordered diamond peak (Dd) with a vacancy internal edge GeA band.
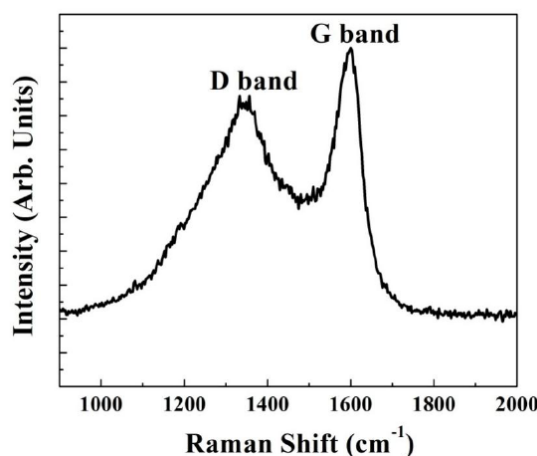
FIGURE 2.24: Picture of Carbon Nanofibers

2.6.7 Glassy Carbon

Glassy carbon is another kind of amorphous carbon: brittle and nongraphitizable. The spectrum of this material usually exhibit relatively narrow and well defined main "D" and "G" bands similar to semiconducting SWCNT. Knowing that glassy carbon is produced with high temperature heating of polymers (between 1000/2000°K),
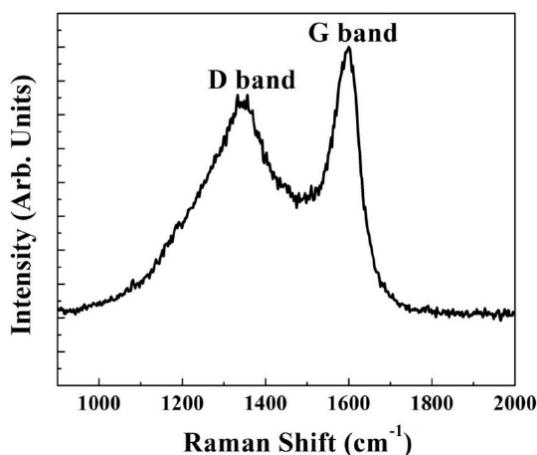
FIGURE 2.25: Raman Spectrum of Carbon Nanofibers

and that corresponding Raman spectrum is analogous to CNT one, it is generally considered a material made by carbon sp2 clusters. Nevertheless, several glassy carbon features suggest this model can be perfectioned: higher hardness than graphenic and fullerenic material (in the 10GPa/15GPa range) and elasticity, high diffusion barrier characteristics although of its porosity and particular Raman up and downshift of the different Raman peaks and band shifting with precursor material types and with the annealing temperature. On many glassy carbon Raman spectra we can see a stress upshifted "G" peak (around 1600/1610cm-1) and a distinct upshifted "D diamond" peak (around 1350cm1) (with a stress upshifting of the same magnitude than the shifting of the "G" peak). This upshifted "D diamond peak" is overlapped to a less intense broader "GeA" band, which is not stress upshifted and in parallel to a ample and soft G2p ("2D") band.
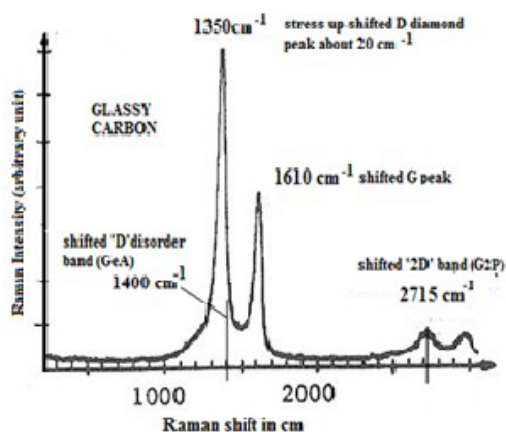
FIGURE 2.26: Raman Spectrum of Glassy Carbon

Chapter 3

Experiment

3.1 Experiment Material: Biochar

FIGURE 3.1: Biochar

Heating biomass in a zero-oxygen environment to temperatures of 250°C or greater produce energy-rich gases and liquids, and a black porous solid residue called charcoal, or char. When this char has been made expressly to have an application in favor of the nature biologically sostenible, for instance as a soil improver or to store carbon, we can name this material biochar.So, BIochar is mostly pure carbon and the thermal process used to produce biochar is called pyrolysis, and by altering the pyrolysis conditions, it's possible to change the attributes of the biochar. Usually, higher temperatures of the pyrolysis process mean a smaller quantity of char, but it could lead to a production of a material carbon more stable. The procedure can take from minutes to days and eliminate volatile compounds such as water, methane, hydrogen, and tar, and leaves behind around 20-30% of black mass and powder of the original weight. The quality of biochars are determined by various chemical traits, despite the fact the peculiarities are interrelated, but they are calculated and examined separately. The majority of the attributions correlated with the charcoal quality are derived by studies done in the field of the industry, in particular steel and chemical About the quality of the biochar, better chemical characteristics of charcoal

are obtained generally with higher levels of fixed carbon and lower levels of ash and volatiles. It is connected with high amounts of lignin and low quantities of holocelluloses and extractives in wood. So, the most important properties of Biochar are:

- • The moisture content: it lowers the calorific or heating value of charcoal. Thus, charcoal fresh from the kiln contains usually less than 1% of moisture, but the moisture content could reach 5-10%, as absorption of moisture from the humidity of the air itself is rapid. Moreover, when the hygroscopitity of charcoal is increased, the moisture content of charcoal can rise to 15% or even more. High quality charcoal has the moisture content of around 5-15% of the gross weight of charcoal. Our moisture is very low.

- • The charcoal's ash content: it is another very important charcoal's chemical property that define its quality,it is linked to fixed carbon and varies from 0.5% to more than 5% depending on raw materials and on carbonization. Our biochars exhibit a very high ash content

- The fixed carbon content: it ranges from a low of about 50% to a high or around 95%.

- Volatile matter: it is linked to the amount of fixed carbon and depends strongly on the carbonization temperature varying from 300 ° C to 1000 ° C. Thus at low temperatures (300°C) the content of volatiles is high, at carbonization temperatures of 500-600°C volatiles are lower, at temperatures of around 1000°C the volatile content is almost zero and yields is around 25%. In general, the volatile matter in charcoal can vary from a high of 40% or more down to 5% or less.

- Yield: at low temperatures (300°C) the charcoal yield is nearly 50%, at carbonization temperatures of 500-600°C yields is 30%, at temperatures of around 1000°C yields is around 25%.

- Hydrogen and oxygen content.

- Toxic residues

Tab. 3.1 resume the informations about the materials we studied (see Appendix for in-depth data).

Acronym	Feedstock	Nominal HT(°C)	Production
OSR	Oil Seed Rape Straw Pellets	550, 700, 1500, 2200	Pilot-scale rotary kiln pyrolysis unit
MSP	Mischantus Straw Pellets	550, 700	Same
WSP	Wheat Straw Pellets	550, 700	Same
SWP	Soft Wood Pellets	550, 700	Same
RH	Rice Husk	550, 700	Same
SS	Sewage Sludge	550	Same
Mischantus		350, 550, 750	Same
Willow		350, 550, 750	Same
Pine		550	Same
PKS	Palm Kernel Shell	550	Same

TABLE 3.1: List of type of Biochar studied

Nominal HT (°C)	550	700
Moisture (%wt)	1.5-1.8	1-3.6
Carbon (%wt)	46-85	48-90
Hydrogen (%wt)	1.2-2.7	0.6-1.8
Oxygen (%wt)	2.4-10.6	2-7
Biochar Yield (%wt)	21-37	17-32
Volatile Matter (%wt)	7-13	7-16
Ash (%wt)	7-16	7-16

TABLE 3.2: Characteristics of the produced materials with respect to the heating temperature

3.1.1 General Considerations about the Raman Spectrum of Biochar

The two most important things about biochar's raman spectrum has to be taken in account always are:

- Band broadening is always associated to atomic disorder

- Frequency well-defined Raman peak correspond to a resonance and consequently to a ordered material structure

First we have to focused on the first orders peak and bands that are present between 1000 to 1700 cm-1 as shown in fig. 3.2 The profile in this section of the spectrum resemble very much the features of other types of amorphous carbon, for example hydrogenated amorphous carbon or carbon nano fibers. G peak due to the vibrational mode of aliphatic sp2-sp2 bonds is somewhat upshifted from 1580 to almost 1600 meanwhile the so-called D peak is in between the Ddiamond peak at 1330 cm-1 and the so-called Ddisorder (or GeA) peak at 1350 cm-1. This is due very probably to the sovrapposition of the effects and so revealed both the presence of carbon atoms hybridized sp3 and vacancies of internal A edges. But the broadening is so much extended that we can't excluded the presence of other effects and internal peaks for example Gc5 and Gc7 peaks at 1490 cm-1 and 1540 cm-1 generated from carbon rings of five and seven atoms[10].

Meanwhile for what concerns the "2D zone" between 2300 cm-1 and 3300 cm-1 in fig 3.2, we see a very broad band that covers three main peaks at 2700, 2910, 3170. According to recent studies these peaks arise from seven different processes of Raman resonance scattering[15] , as shown in fig.. 3.3.

3.2 Micro-Raman Apparatus

A micro-raman apparatus is usually made by these important components: an excitation source, notch filters, focusing mirrors, a microscope apparatus, a grating and a detector as shown in fig. as well as a PC and a dedicated software [6]. The process is described below:
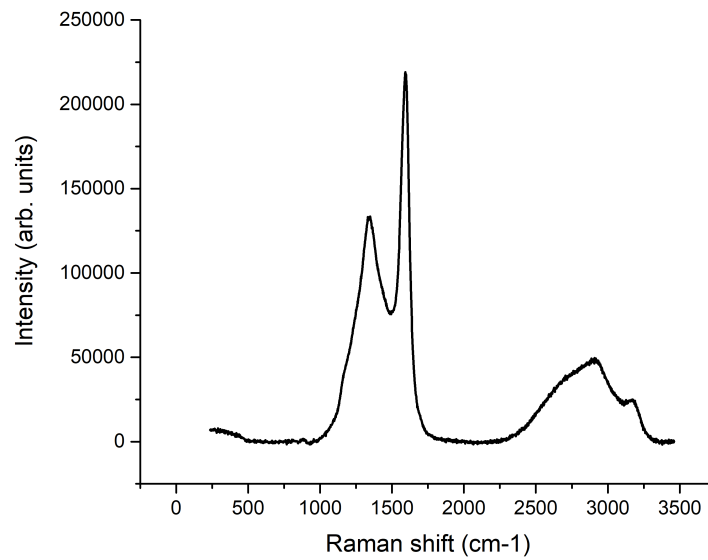
FIGURE 3.2: Raman spectrum of a sample of Biochar (SWP700-BX20130410)
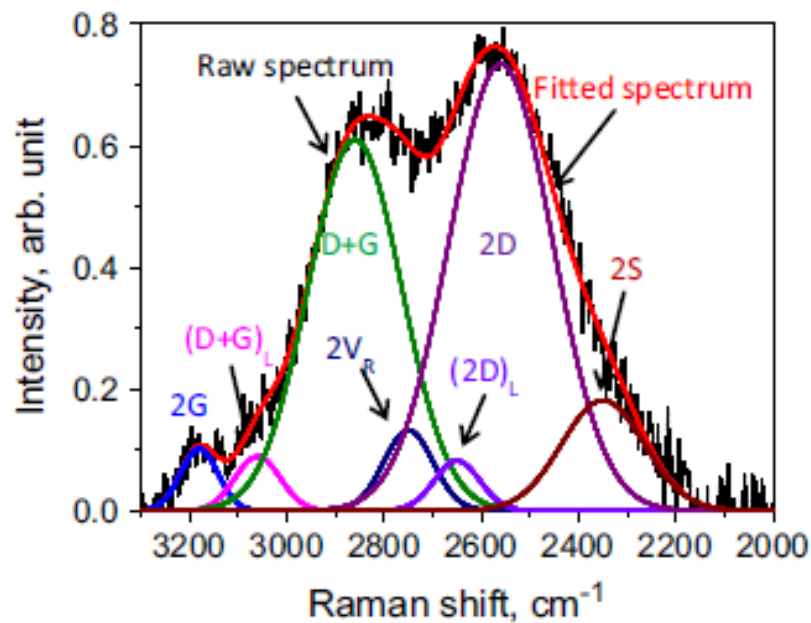
FIGURE 3.3: Second order Raman peaks

1. The excitation source, usually a laser source, produce a electromagnetic radiation of a very precise frequency

2. The light is amplified and then focused on the sample through mirrors and a microscope

3. The light is scattered by the sample and come back from the same path

4. Various filters eliminates unwanted frequencies during the route, for example Rayleigh peak, "useless" and very intense

5. The grating select and split the right frequencies

6. A Charge Coupled Device detector absorb the radiation and convert it into digital values
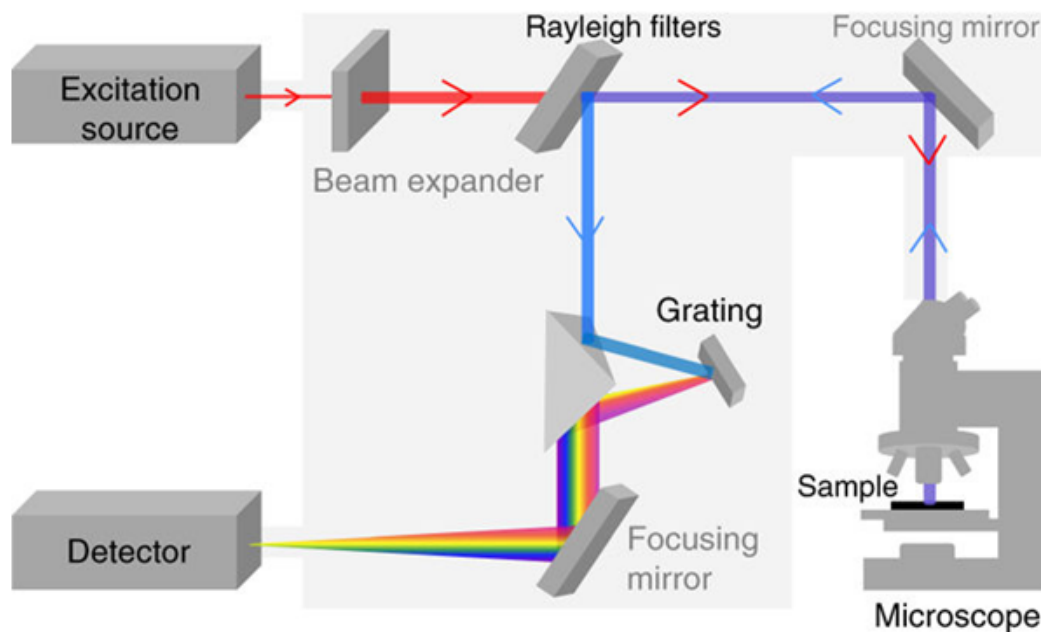
FIGURE 3.4: Schematic Representation of a micro-Raman Apparatus

Our measurements have been taken in a Politecnico Lab with two very similar micro raman apparatus. The first Raman apparatus is an old Renishaw model, equipped with only one Laser source at 514.5 nm, and an "open air" microscope stage. The other one is a more modern Raman Spectrometer InviaH from Renishaw, equipped with three different laser source (one "green" at 514.5 nm, one red and one blue) an "enclosed" stage and an updated software.

FIGURE 3.5: The most recent Raman Apparatus in PoliTo
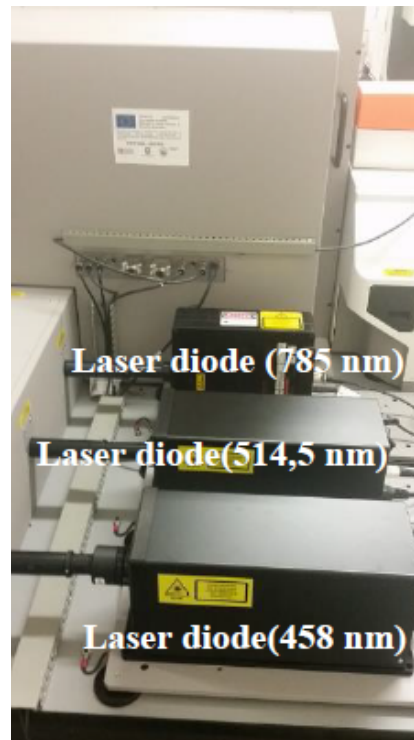
FIGURE 3.6: Three different lasers behind Raman apparatus
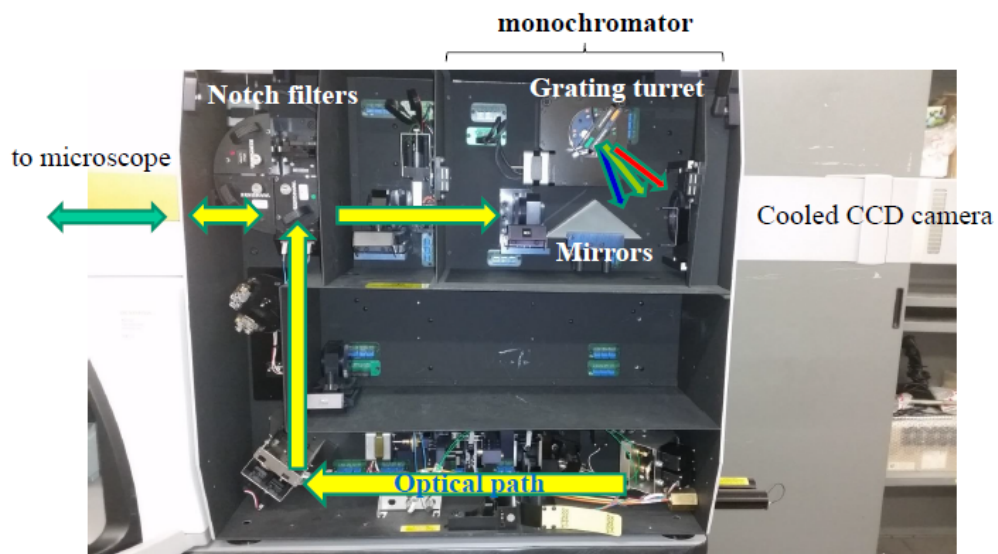
FIGURE 3.7: What a Raman apparatus looks like inside and how it works

3.3 Measurements

Making measurements with a Raman apparatus is a relatively easy process and can be divide in some distinct steps:

1. Switch on the PC, the Laser source and the spectrograph

2. Start the software that controls the instrument

3. Calibrate the instrument using a silicon sample because we know that it has only one peak precisely at 520 cm-1

4. Prepare the Biochar sample put less than a cubic centimeter of material powder on the microscopic slide, than compress it to obtain a compact planar structure, easier to visualize and to focus

5. Visualization and focusing of the magnified sample

6. Search of a flat and not too "light" fragment of material

7. Select the mode of acquisition, the number of cycle of acquisitions and the power of the light ray

8. Start the acquisition of the signals

9. Repeat the process of acquisitions at least another time to have consistent signal and avoid wrong results

10. Take the slide, remove the material, clean the slide

11. Repeat from step 4 to step 9 of the process

The most interesting thing we found in making measurements with the two Raman Apparatus was that the results were slightly different even considered the amorphous nature of the sample and the impossibility of finding the exactly same grain for the measurements. Even if officially the difference between the two should be only the more easiness of use and the possibility of using more than one laser for the more recent Raman apparatus, we think that could be some difference in sensibility. fig 3.8 shows clearly the problems that arise when we studied Raman spectra of biochar materials taken by different instruments. In this case we have four different signals of the exactly same sample (SS30) measured with our two Raman apparata. After the normalization related to G peaks, we see that the signals are consistent if we considered the same instrumentation and this is a proof that the instruments are not broken but we cannot confront them between each others. It seems that the old Raman (Raman 2 in the picture) tend to flattened and compensate the G peak, resulting to a greater ID/IG ratio. We came to the conclusion that we had to use only one instrument to make all the measurements. So we decide to use only the more "advanced" and more recent micro Raman apparatus.

At the end of the day these are the characteristics of our measurements and the settings for InviaH Renishaw Raman Spectrometer:

- Light source: green Argon laser with 514.5 nm of wavelength and 2 μm of diameter

- Power of the light source: 5 mW (1%)

- Cycles of acquisitions: 3 (some minutes to complete the processes)

- Exposure time for each acquisition: 10 seconds

- Microscope magnification: 50x

- Range of acquisition: from 400 cm-1 to 3500 cm-1
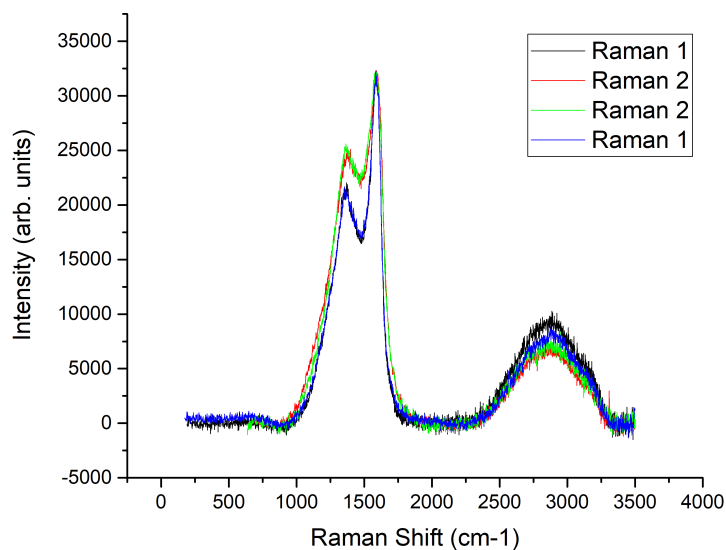
FIGURE 3.8: Comparison of sensibilities between two Different micro-Raman Apparata

3.4 Analysis of the Raw Signals: Intensity and Fluoresce

When you have a Raman raw signal you can check and study few things related to the intensity and fluorescence of the signal, because we use Raman for qualitative information more than for quantitative Intensity of the signal in Biochar materials is due generally to . Factors like focus, fluctuations in laser intensity and the orientation of the sample relative to the laser beam and Direct comparison of intensity values obtained from two separate data collection is a little problematic because we are talking about more of of an instrumental data (with an arbitrary unit) rather than a physical data. the difference in intensity is just an artifact in sample preparation and the concentration of the sample in our case can't be properly controlled before measurements.

So there isn't clear correlation between the type of wood from which is derived the biochar or the temperature of production and the intensity of the signal A plain example is showed in fig. 3.9: there are three signals from three different samples of the same material produced in the exactly same way: the most intense one it was taken days before the other two signals by two different persons. It's obvious that the intensity of the two almost equal signals is due to the fact that the signals were taken at distance of few minutes and in the same ways. Furthermore, after the treatment of the signals we confirmed that all the three signals are pratically indistinguishable.

Fluorescence is instead an important phenomenon in spectroscopy and in our experiment considered in general unwanted because is competing with Raman scattering especially at low frequencies because in most cases the emitted light has a lower energy than the absorbed radiation. As we know, a laser photon hit a molecule and looses a specific quantity of energy that allows the molecule to vibrate (this the case of Stokes scattering). Thus, the scattered photon has less energy and the detected light shows a frequency shift. The various frequency shifts associated with different molecular vibrations generates a spectrum that is peculiar of a specific element
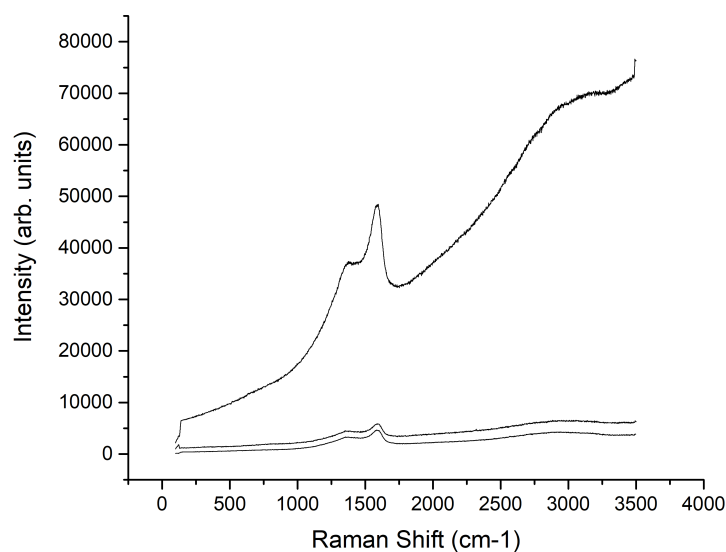
FIGURE 3.9: Comparison of Raw Signals Between Different Materials

or material. Instead, fluorescence or luminescence emission follows an absorption process. For a better understanding, one can refer to fig. 3.10.
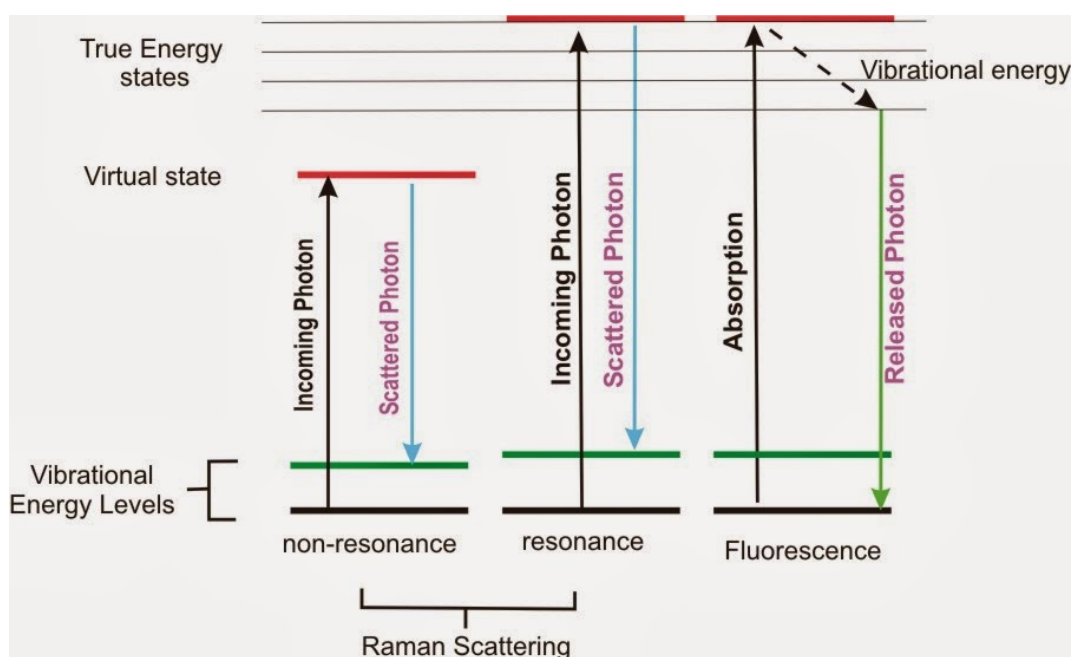
FIGURE 3.10: Comparison between Raman scattering and fluorescence

Fluorescence derives from the emission of a photon from the lowest vibrational level of an excited electronic state, succeeding a direct absorption of the photon and relaxation of the material from its vibrationally excited level of the electronic state back to the lowest vibrational level of the electronic state. A fluorescence process

(A) *Raw signal of a sample of Wsp 550*

(B) *Raw signal of a sample of Wsp 700*
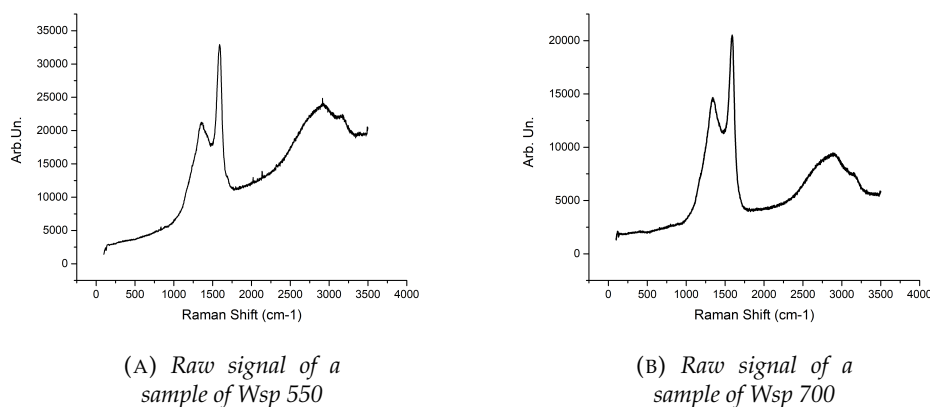
FIGURE 3.11: Comparison between spectra of WSP

(A) *Raw signal of a sample of Mischantus 350*

(B) *Raw signal of a sample of Mischantus 750*
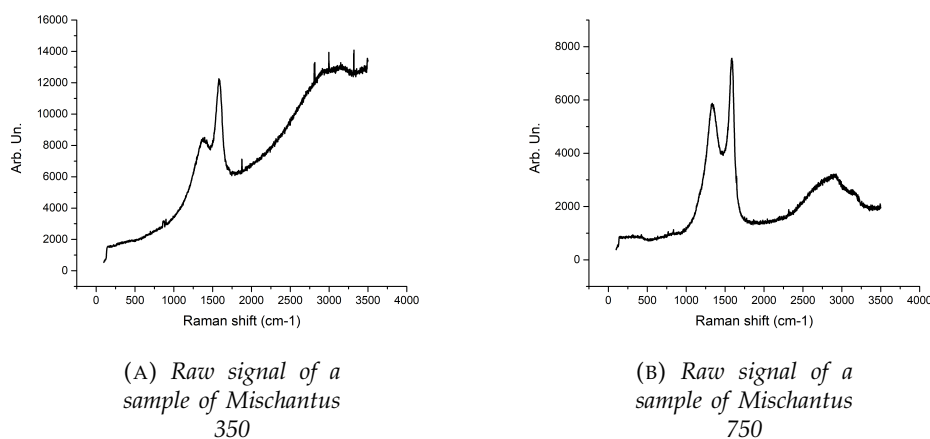
FIGURE 3.12: Comparison between spectra of Mischantus

generally requires more than 10-9s. Instead, Raman scattering is completed within a picosecond or less. If the excitation photon does not furnish adequate energy to the molecule, the necessary transition to give rise to fluorescence will not take place. Nevertheless, if fluorescence is produced, it is often much stronger than the Raman signal, covering Raman features.

This is typical of organic compounds so, in Biochar materials is a good indicator of the state of carbonization of the sample. So results confirm this hypothesis: as shown in fig 40 there is a clear difference between signals of Biochars at 550 C vs 700 C: at lower temperature the fluorescence is higher. This is more evident compairing samples with larger differences in temperature for example 350 vs 750 (see fig41). The only material that shows similar fluorescence besides the different value of temperature is RH. In particular fluorescence for 750 samples is more emphatized than the other materials at the same temperature as seen in fig. 3.13.
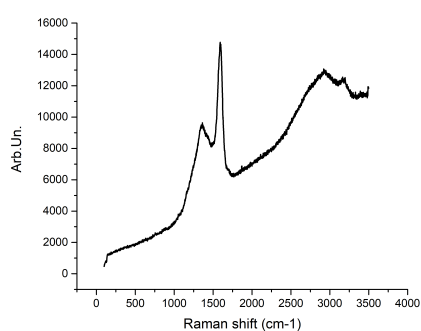
(A) *Raw signal of a sample of RH 550*
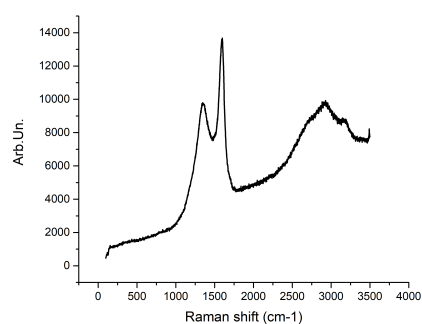
(B) *Raw signal of a sample of RH 700*

FIGURE 3.13: Comparison between spectra of RH

Chapter 4

Treatment of the Signals

As previously said, raw signals of amorphous carbon materials give fews informations, so it is needed a method to refine the spectra and obtain more maneageable signals. In PoliTo we developed a complete MatLAB program that in few passages it can extrapolate a fitted signal. The importance of having a fitted and numerically exact spectrum is justified by the things that we can find after the fitting of the signal:

- The value of the Id vs Ig ratio

- The values of the width of the peaks or bands

- The evolution of the material with the temperature

- The comparison between different materials

In order to achive these results we have modify the spectrum in some distinct passages:

1. Modifies the values of the spectra taking in account the quantic detection efficiency of the detector

2. Draw the baseline for every signal

3. Normalize the spectra between each others

4. Fitting the signals with an appropriate set of functions

Point one is very easy to satisfies, because we know the QDE of our detector, so the program will make a simple operation for every "point" taken by the CCD in relation with the wavelength of the light source. In the next sections we will analyze one by one the next three steps.

4.1 Baseline

Drawing a baseline for a Biochar's raman spectrum is a fundamental operation because as we previously said the fluorescence in these kinds of materials is very high and we need to eliminate it in order to being able to fit properly the signal. So we drawed the baseline after make some proper considerations about the fluorescence and the spectrum itself. The operation of the baseline itself is done thorugh very precise and unskippable passages.

First we have to delineate the range of signal that we want to study. In our case is virtually the entire spectrum so we can leave it untouched but in certain cases at the boundaries the spectra there can be some strumental alterations. In those situations we cut away the unnecessary part from the data.

Then we have to choose the kind of functions that are going to draw the baseline. In general there are a lot of program, unspecific as Origin or specific as the software provide by Renishaw itself, that use a line or a series of line to draw the baseline. This is not phisically justified by theoretical tractation of fluorescence and the effects on materials spectra. Lorentzian and Gaussian functions represent much better this phenomenon, as shown in fig. 4.2 After choosing the type of functions, we have to underline the background of the spectrum where there isn't presence or sign of peaks (see fig.. 4.2). You can also choose manually singular points that will be taken in account by the program during the fitting. Finally, we have to choose the method of interpolation of the functions: we can use the method of func or fminsearch. The first one is faster but less reliable so we used always the second one.
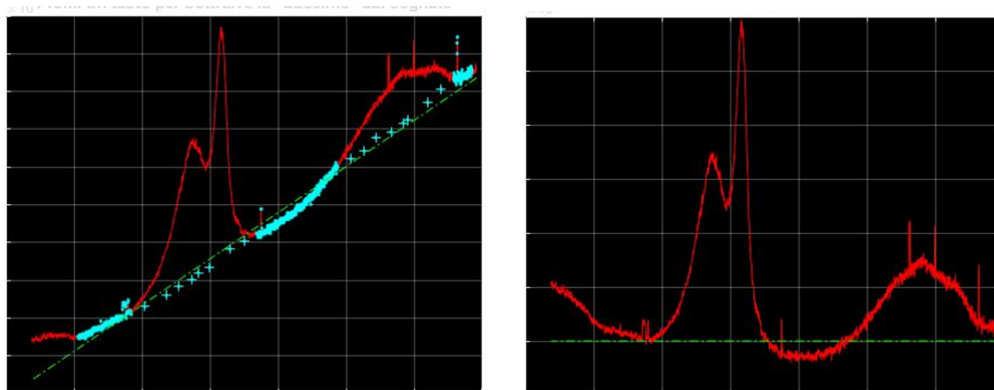
FIGURE 4.1: Example of a linear baseline
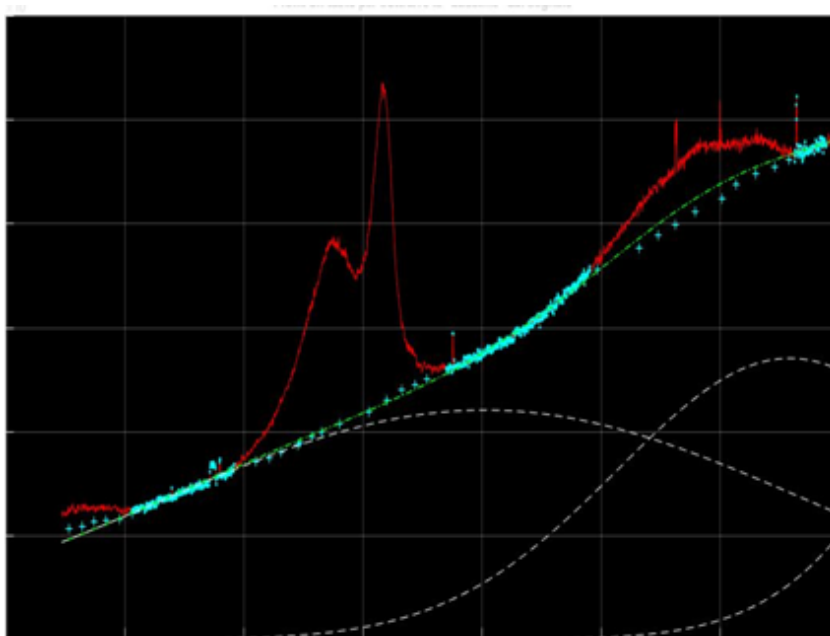
FIGURE 4.2: Example of Gaussian baseline
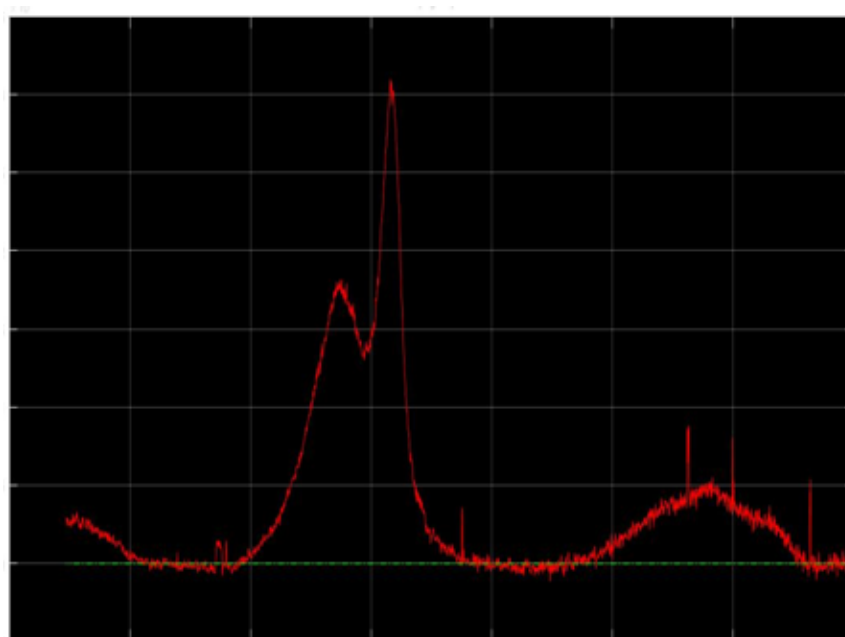
FIGURE 4.3: Results of Gaussian baseline

4.2 Normalization

After drawing the baselines for all the spectra we have to normalize the signals between each other because, as we know, the intensities of the spectra are in arbitrary units and we don't care about those, but we are interested only in the correlations between the shape of the signals. Since we are primarily interested in studying the ID/IG region and 2D region heigth is in a certain way we can choose either the G peak or the D peak to normalize the spectra regardless. We chose the G peak and performed the normalizations with another simple program indipendent from that one we used for fitting and baseline.

4.3 Fitting

The fitting process has to be done strictly after the baseline drawing but it can be done indipendently the normalization, knowing that the only differences would be in the evaluation of absolute area of the fitting functions. In general, we made first the process of normalization and then we fitted the signals, we find this method as simpler, faster and more practical.

The initial procedure is relatively simple: you have to choose a set of functions that the program will manipulate to obtain a fitted signal, composed by the sum of all those functions, that minimize the error with respect to the real signal. This is a matematical and precisely a numerical process that doesn't count any physical interpretation. Also, the results can slightly vary from time to time, even for the same spectrum. When you choose for the first time the library of functions it is important to use a set of a lot of functions to be sure of obtain the best fitting possible. Then you find how many functions has been used actually and eliminate the worthless functions. After finding the right number of functions that are needed to properly fit the signals, we found ourselves in the most critical and arbitrary part of the project.
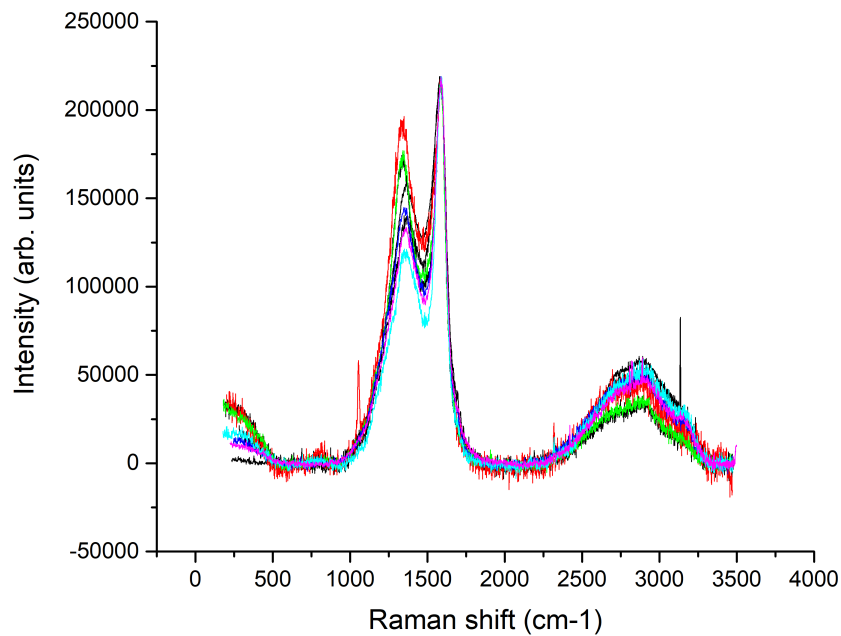
FIGURE 4.4: Example of normalizations on G peak

There are two main ways to prosecute the work and we could use two different approaches to comparate the materials:

1. Leave to the software the faculty of finding for each signal the best solutions and then comparate the components of the fitted solutions for every sample

2. Make some attempts for various samples and materials in order to find a set of functions that can be the same for every spectrum. Then fitting every sample maintaining fixed centers for every functions

If the materials don't show a visible peak shifting the second method could be more maneageagle and lead to more informations because you have only to care about heights and widths of the components of the fitted spectrum. So we preferred to use the second method.

Chapter 5

Analysis of Fitted Spectra

5.1 Characteristics of the Fitted Signals

The general characteristics of the fitted signal are the same for every materials we studied. D peak and G peak zone is perfectly fitted using four gaussians, two for each peak as shown in fig. 5.1
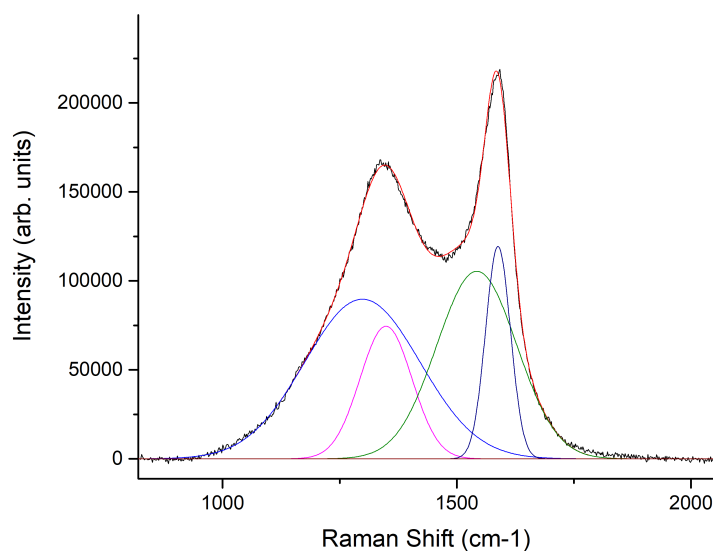
FIGURE 5.1: D and G bands of OSR 700

For the 2D zone we fitted with three gaussians (see fig. 5.2), hinting at the probable derivation from the three peaks that we find in graphene materials at those wavelengths.

5.2 Comparisons of ID/IG for Different Materials at the Same Temperature

The first important study and comparation we did it was focused on find if different woods from which derived the materials and lead to different properties can have different features in Raman spectra. We decided to make comparation between OSR, SWP, WSP, MSP and RH biochars at 700 C, because they are the only materials at that precise temperature and they are the materials for which we have the most
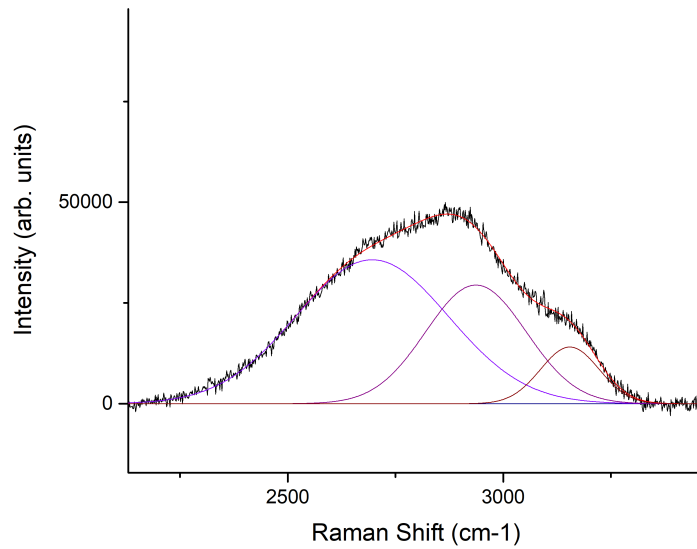
FIGURE 5.2: Second order zone of the spectrum of OSR 700

complete and detailed datasheet (see Appendix). We used a "fixed center" fitting using a library with those characteristics:

Acronym of the Peak	Center of the Peak (cm-1)
D(1)	1298.4
D(2)	1348.7
G(1)	1542.7
G(2)	1587.9
2D(1)	2695.9
2D(2)	2936.6
2D(3)	3154.6

TABLE 5.1: Library of Gaussian functions used in the fitting

A similar kind of library was used in fig. 5.1 and fig. 5.2. One result is shown below:

Amplitude (Arb. Un.)	Center (cm-1)	Width (cm-1)	Shape	ID/IG
				1.26
2.83	1298.4	116.1	Gau	
0.73	1348.7	47.9	Gau	
1.98	1542.7	87.1	Gau	
0.85	1587.9	25.5	Gau	
1.35	2695.9	170.2	Gau	
0.66	2936.6	105.9	Gau	
0.22	3154.6	64.8	Gau	

TABLE 5.2: Data of the resulting fitted functions for RH 700-626
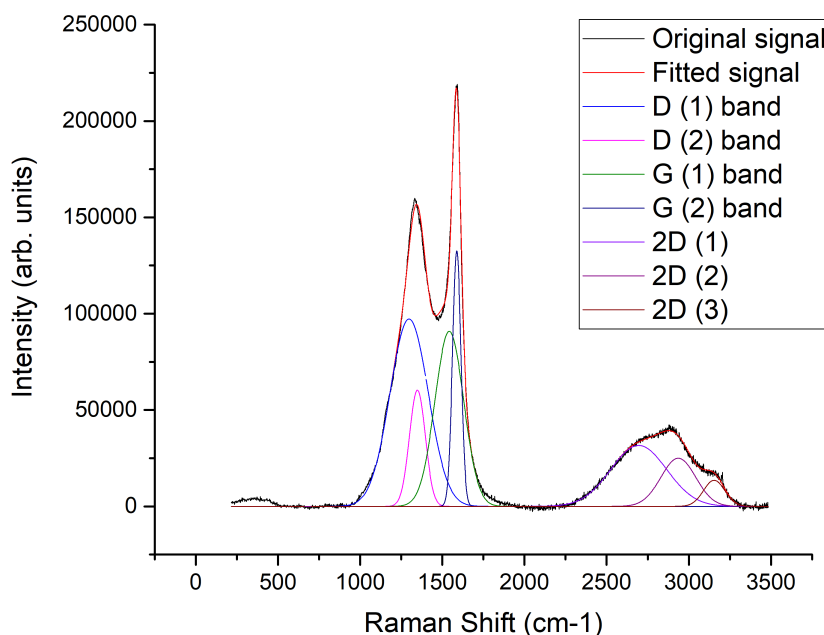
FIGURE 5.3: RH 700-626

Id/Ig ratio was calculated adding the first two gaussians (D(1) and D(2)) and dividing by the sum of the third and fourth functions (G(1) and G(2)). Looking at fig. 5.3 is straigthforward the reason which we used a fixed center fitting: the materials are so amorphous that it's not easy to divide the "real" D band from the "real" G band, also because, as we saw in chapter 4.1, that structure is probably formed by some others resonance raman scatterings. So the absolute value of Id/Ig can't give precise informations about the material but using a properly set of functions with fixed centers we can at least comparate two separate but very similar raman spectra.

Name	Id/Ig	Name	Id/Ig
MSP 700-10	1.13	RH700-627	1.18
OSR 700-828	1.25	RH 700-530	1.15
OSR 700-621	1.18	RH 700-701	1.06
OSR 700-508	1.12	SWP 700-415	1.10
WSP 700-429	1.19	SWP 700-410	1.09
WSP 700-513	1.14	SwP 700-424	1.14
WSP 700-205	1.25	SWP 700-617	1.16
RH 700-626	1.26	SWP 700-823	1.15
SWP 700-819	1.13		

TABLE 5.3: Id/Ig for every material heated at 700 C

As we see from the list above the Id/Ig ratios for our biochar materials are always around the value of 1.1. The variations that we found (from a minimun value 1.06 to maximum value 1.25) we think they can be due to some factors. These signal pass through the step of acquisition, the drawing of the baseline, the normalization

and then the mathematical fitting so some discrepancies are taken in account. Also, we see that the different values of Id/Ig are usually distributed equally for every kind of materials, infact if we would make the mean of the values we would obtain pratically the same results for every material. To conclude we can say there are no differences in the spectra of different materials.

5.3 Comparison of Id/Ig for Different Temperatures for the Same Material

After demonstrate that it's very difficult ricavate differences and peculiarity of different Biochar's samples from their raman spectra we focused in the evolution of the raman spectra for the same starting material (same woods) and same fabrication features but different NHT (nominal heat temperature). Mischantus and Willow samples provided by the University of Edinburgh were suited for this purpose: as seen in Appendix we have three different samples at three different temperatures (350, 550 and 750) for both kind of biochar. We noted from the drawing of the baseline and the subsequent normalization that could be some evidences of an evolution in the features of the raman spectrum for every biochar material. If we compare the signals, even without mathematical and analytical instrument, we can roughly estimate an increment of the "D peak" with respect to the "G peak". This is shown in fig. 5.4:
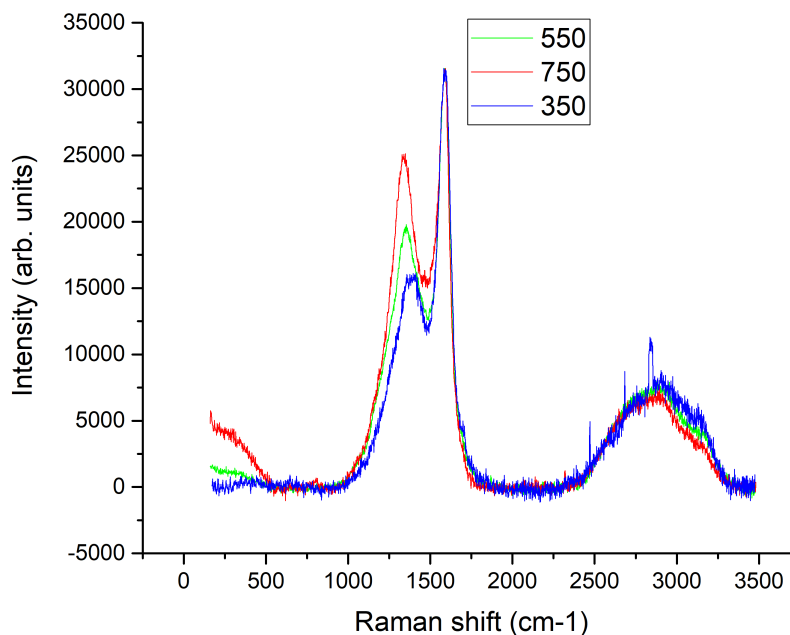
FIGURE 5.4: Willows of the series 1011/3

To validate our hypotesis we submit these samples to the same procedure viewed in chapter 6.2. For Willows we used this library of functions:

Acronym of the Peak	Center of the Peak (cm-1)
D(1)	1283.4
D(2)	1358.0
G(1)	1548.7
G(2)	1586.3
2D(1)	2676.0
2D(2)	2930.2
2D(3)	3162.0

TABLE 5.4: Library of Gaussian functions used in the fitting of willow samples

One of the results is shown below (fig. 5.5):
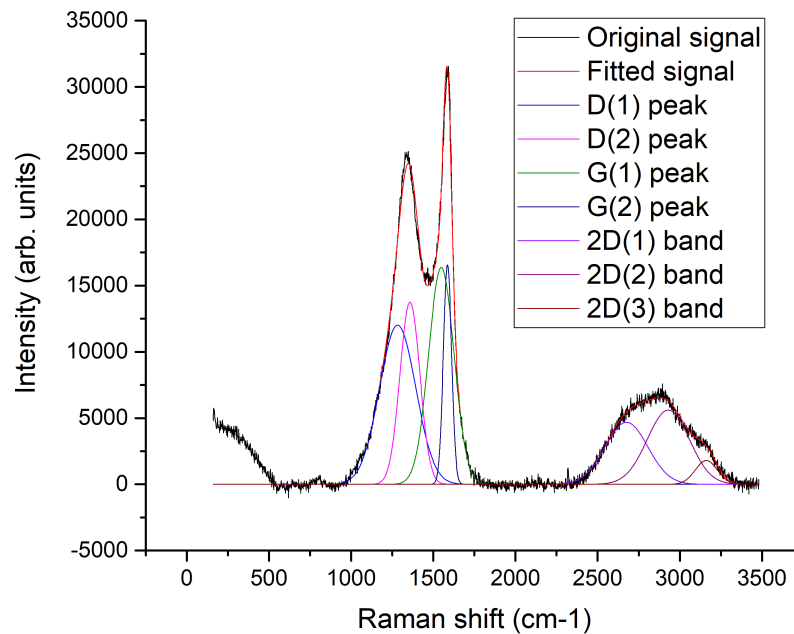
FIGURE 5.5: Fitted willow of the series 1011/3

The general results of ID/IG for every willows samples are shown in the next list:

From these results it is clear the slight evolution of the ID/IG ratio with respect to the temperature.

We made the same procedure with Mischantus using another type of library of functions:

And the Id/Ig ratio of every sample is :

Even in this case we see the increasing of Id/Ig ratio with respect to the increasing of NHT. The differences between Mischantus and Willow at the same temperature are mainly due to the differences between the set of functions chosen.

Amplitude (Arb. Un.)	Center (cm-1)	Width (cm-1)	Shape	ID/IG 1.29
3.32	1283.4	110.2	Gau	
2.08	1358.0	60.2	Gau	
3.16	1548.7	76.9	Gau	
1.04	1586.3	24.9	Gau	
1.52	2676.0	129.4	Gau	
1.80	2930.2	128.1	Gau	
3.02	3162.0	66.9	Gau	

TABLE 5.5: Data of the resulting fitted functions for Willow 750 series 1011/3

Willow350	Id/Ig	Willow550	Id/Ig	Willow750	Id/Ig
1009-171	0.94	1009-171	1.02	1009-171	1.23
1009-177	0.91	1009-177	1.03	1009-177	1.30
1011-3	0.78	1011-3	1.04	1011-3	1.29

TABLE 5.6: Id/Ig for every willow sample

Acronym of the Peak	Center of the Peak (cm-1)
D(1)	1283.4
D(2)	1358.0
G(1)	1527.9
G(2)	1582.7
2D(1)	2719.7
2D(2)	2959.2
2D(3)	3147.3

TABLE 5.7: Library of Gaussian functions used in the fitting of mischantus samples

Mischantus350	Id/Ig	Mischantus550	Id/Ig	Mischantus750	Id/Ig
1011-9	0.67	1011-9	0.85	1011-9	1.04
1011-17	0.77	1011-17	0.95	1011-17	1.03
1011-23	0.76	1011-23	0.90	1011-23	1.21

TABLE 5.8: Id/Ig for every mischantus sample

5.4 Comparisons of the Width of the Components for Different Temperatures of the Same Material

We found to this point differences in Id/Ig ratios vs nominal heating temperatures. So we thought that could be differences in the materials due mainly to the increasing of the heating temperatures. One practical way to analyse the evolution of similar spectra, for example spectra with fixed center's fitting functions, as in our case, is focusing on the width of the peaks. Thus, starting from the solutions of the previous chapter (6.2), we relate the value of the width vs NHT for Mischantus and willow:
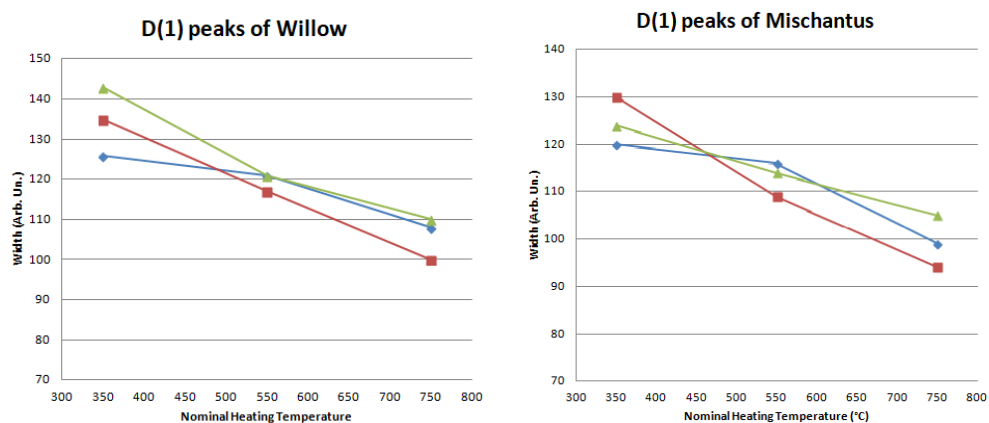
FIGURE 5.6: Comparison between spectra of WSP
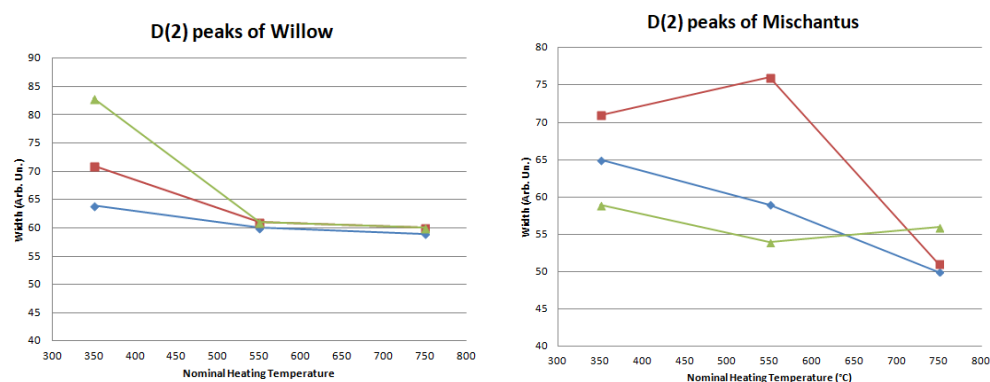
FIGURE 5.7: Comparison between spectra of WSP
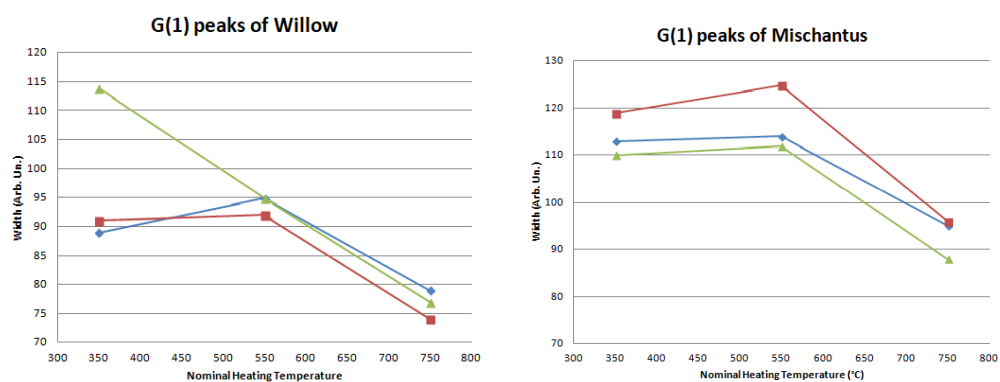
FIGURE 5.8: Comparison between spectra of WSP
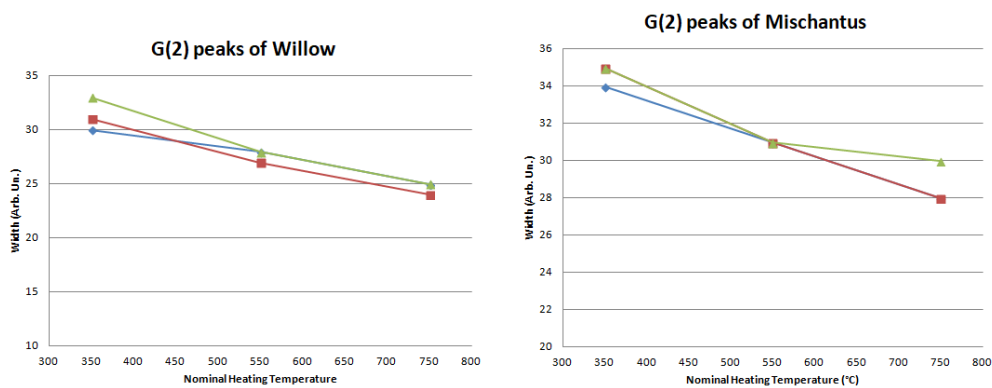
FIGURE 5.9: Comparison between spectra of WSP

From these results we can extrapolate neat considerations about Biochars: although there isn't an unequivocal trend in the width of the peaks between 350 and 550, if we compare the width of the peaks at 350 with the width of the same peaks at 750 we find always a consistent drop for each kind of peak. The behaviour of the widths of the peaks are not so clear when you passed from a heating temperature of 350 to 550 for a few reasons: first one is the biochar is at low temperatures, so it is very hard to distinguish very disordered structures, second one is due to its relatively small shift in temperature (only 150 degrees), last one is due to the impossibility in finding the same spot for different measurements.

5.5 Final Integrations of the Work

Following the previous intuitions, we tried to complete the work studying the Raman Spectra of Biochar at much higher temperature. We expected to see a further narrowing of the main peaks, D G and the three peaks around 3000 cm-1, that we can explain as the crystallization and in particular the graphitization of the sample [13]. So we took some spectra from sample of OSR heated at 1500 C at 2200 C, a kind of biochar already studied at 550 C and 700 C in chapter 6.2. Fig. 5.10 shows the non-fitted results, but the main characteristics of the signals are already pretty evident:
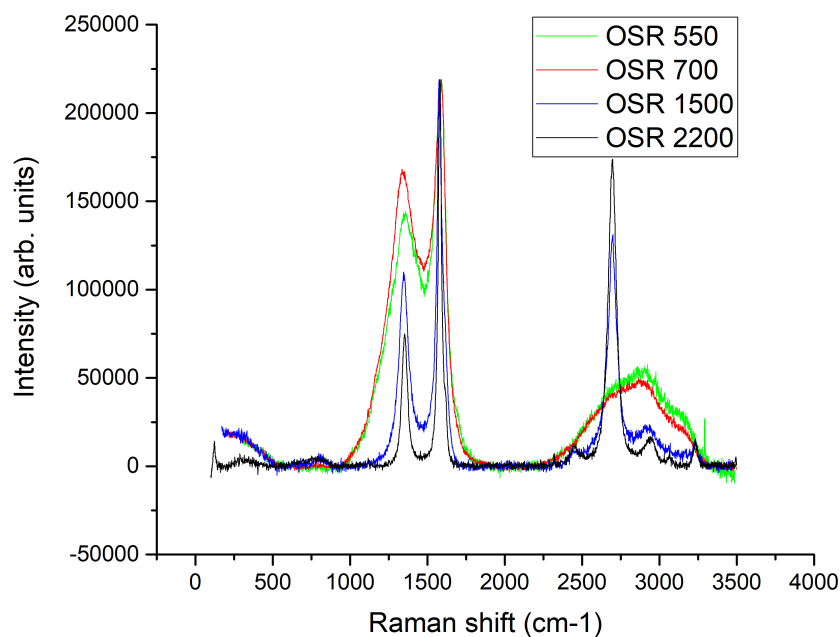
FIGURE 5.10: OSR signals

To make clearer the considerations about these last signals we can make a comparisons with the spectrum of a sample of graphene, as for example in fig. 5.11:
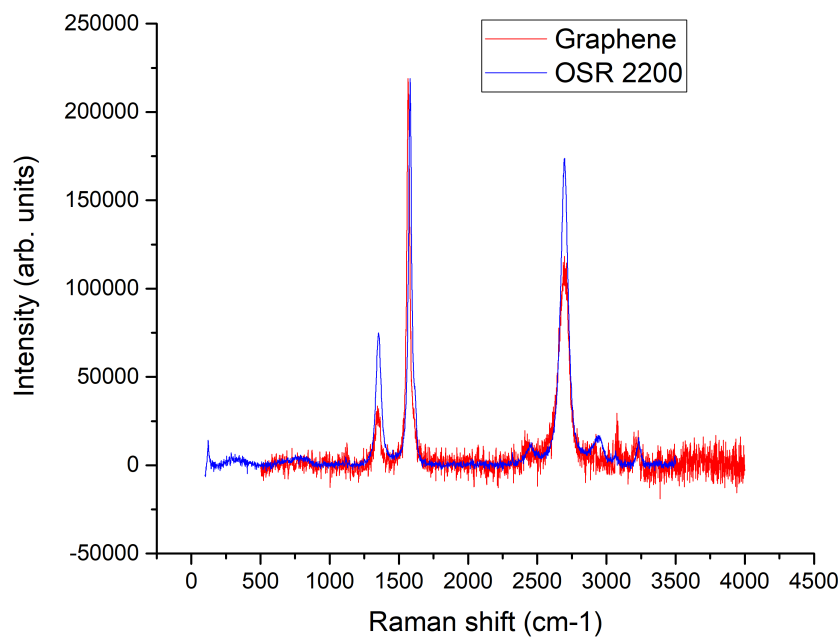
FIGURE 5.11: Comparison between OSR 2200 signal and Graphene spectrum

The obvious next step involve the fitting of the signals. We find these solutions:
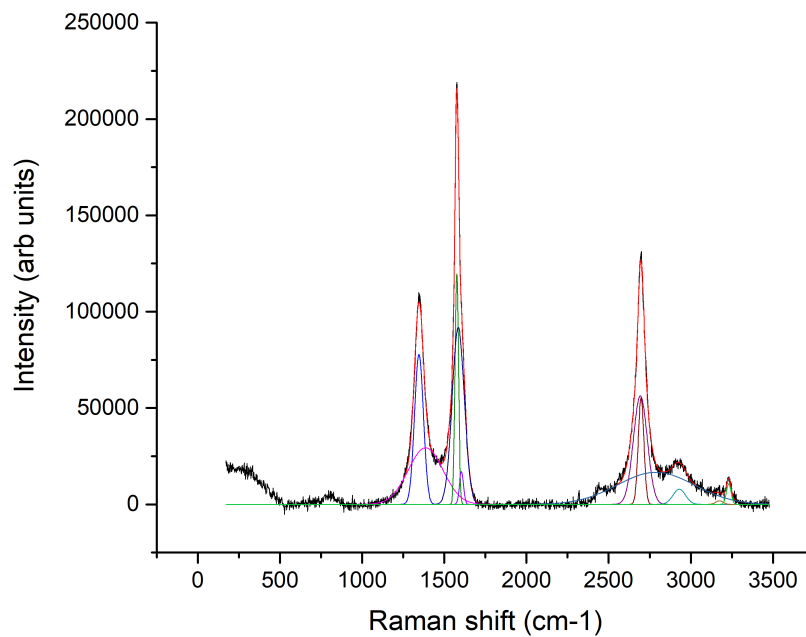
FIGURE 5.12: OSR 1500 fitted

Peak	Amplitude (Arb. Un.)	Center (cm-1)	Width (cm-1)	Shape	ID/IG 1.12
D(1)	5.19	1345.8	26.6	Gau	
D(2)	7.79	1386.0	105.8	Gau	
G(1)	3.14	1576.7	10.5	Gau	
G(2)	8.46	1584.8	36.7	Gau	
	0.52	1604.3	12.2	Gau	
2D(1)	5.95	2692.9	42.1	Gau	
2D(2)	2.37	2697.3	17.1	Gau	
	9.77	2787.9	233.9	Gau	
	0.75	2930.2	38.2	Gau	
	0.11	3174.5	22.53	Gau	
	0.38	3230.7	14.29	Gau	

TABLE 5.9: Data of the resulting fitted functions for OSR 1500
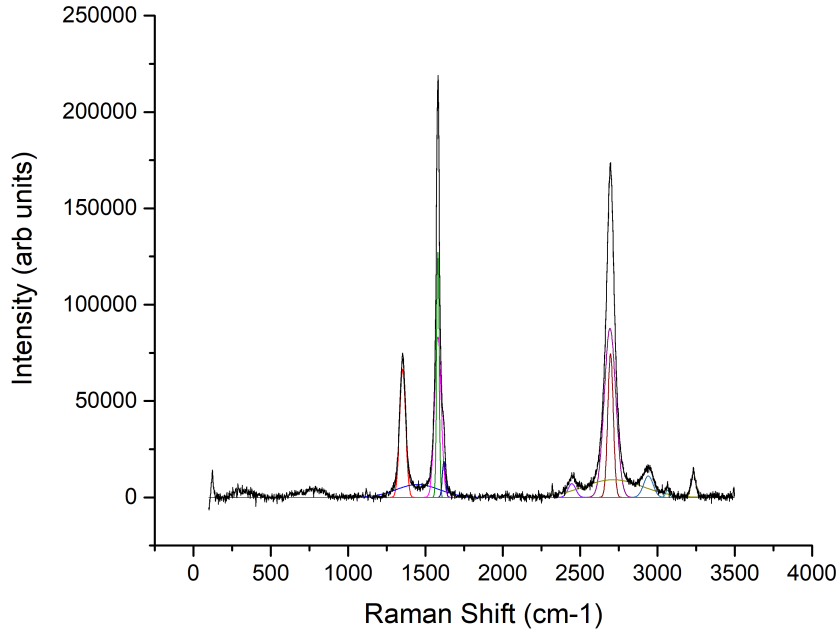
FIGURE 5.13: OSR 2200 fitted

Peak	Amplitude (Arb. Un.)	Center (cm-1)	Width (cm-1)	Shape	ID/IG 0.45
D	3.19	1352.8	19.1	Gau	
	7.79	1451.0	139.4	Gau	
G(1)	3.14	1580.6	21.3	Gau	
G(2)	8.46	1580.8	8.06	Gau	
	0.52	1619.9	10.1	Gau	
	5.95	2447.4	25.3	Gau	
2D(1)	2.37	2693.7	37.0	Gau	
2D(2)	9.77	2697.0	191.7	Gau	
	0.75	2941.4	30.8	Gau	
	0.11	3065.5	12.6	Gau	
	0.38	3233.0	15.5	Gau	
	0.38	3230.7	14.29	Gau	

TABLE 5.10: Data of the resulting fitted functions for OSR 2200

The comprehension of the elements of the fitted signal is a little bit different from the case of lower temperatures, as we studied in previous paragraphs. At these levels of crystallization we can distinguish many more peaks and bands than before and so we have to use a larger set of functions, but the gaussians will be narrower. As we see from fig. 5.10 in the range of wavelenght of second order raman scattering we see a very high 2D peak, this is typical of graphene and graphite (fig. 5.11), and we explained the meaning in chapter 3.6.3. Instead, in the range of first order raman scattering (mainly D and G band) we can notice for OSR1500 a substantial narrowing of the peaks and for OSR2200 even a great change for D peak, that become a

single gaussian meanwhile the gaussians that was the second D peak become a simple background between D and G bands. Furthermore, the Id/Ig ratios emerge as incomparable each others. Fig . 5.14, 5.15 and 5.16 illustrate very well the differences between the raman spectra. Finally in fig. 5.14, we see the differences between a sample of graphite and OSR2200. Although very blurred (this is due to the instrument) graphite has narrower peaks and a lower D peaks with respect to Biochar. Therefore, OSR2200 still shows traces of its (previous) disordered nature.
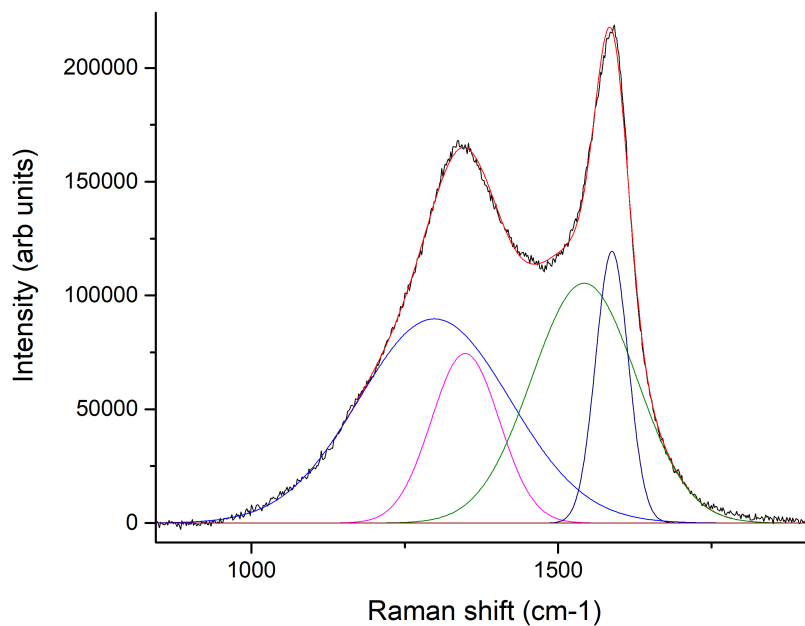
FIGURE 5.14: OSR 700 fitted in the 1st order "zone"
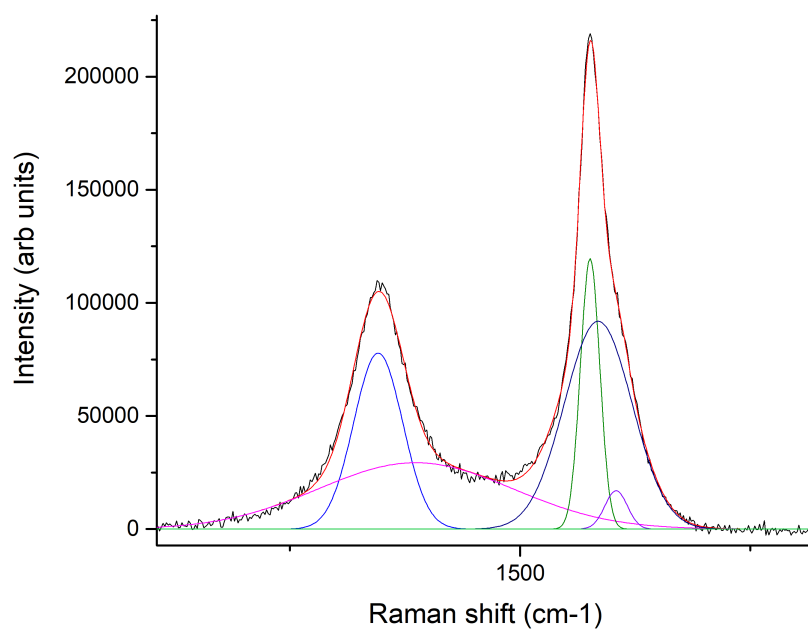
FIGURE 5.15: OSR 1500 fitted in the 1st order "zone"
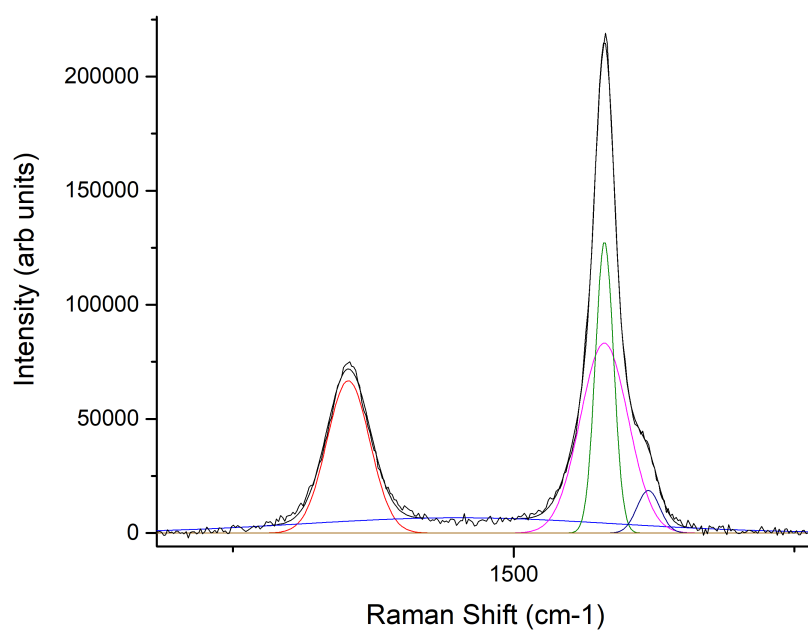
FIGURE 5.16: OSR 2200 fitted in the 1st order "zone"
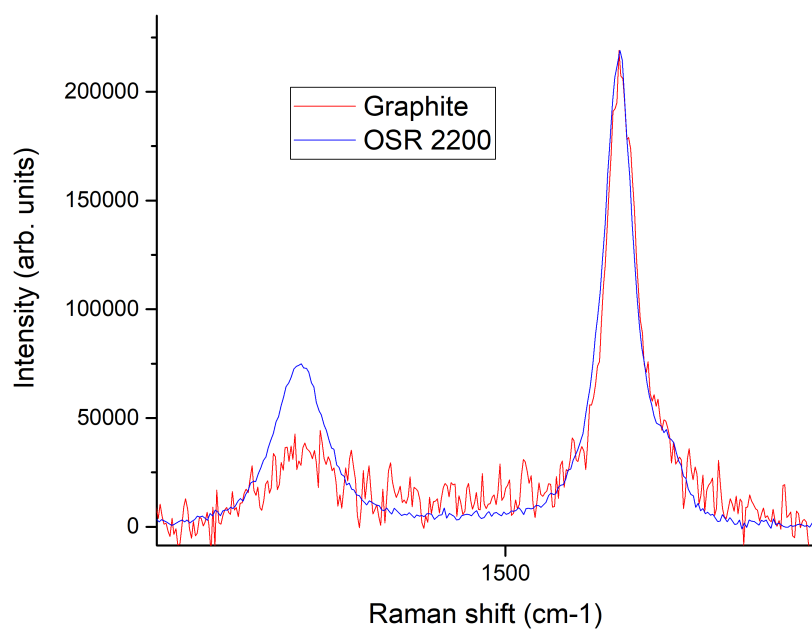
FIGURE 5.17: Comparison between graphite and OSR2200 spectra

Chapter 6

Conclusions

The analytical study of the Raman spectra of carbons has been an ample, variegated and discussed scientific field in the past few years. The increasing of the precision and sensibility of the newest machines that performs this type of spectroscopy and the increasing of the potential applications for a wide variety of carbon based materials have made the process of raman scattering worth of deep researches. Our project had and still continue to have great ambition: find correlations between raman spectra and properties of biochars is a challenge that could lead to improvement and understanding of the material and the mechanisms of scattering and also for raman instrument. During the work we deal with a lot of difficulties due to the nature of the material and in some cases also the lack of technical specifications and informations about some aspects of the behaviour of the raman spectrometer and theoretically informations about the Raman scattering in biochars. Our initials hypothesis and data on the two micro-Raman apparatus state that there shouldn't be differences in sygnals acquired by the two instruments. Instead, results show a clear distinction in shape between the Raman spectra, probably due to the different sensibility and capacity of focus, so we had to study signals take by one only instrument to deduce consistent conclusions. Theoretical studies and reaserches about the nature of the peaks and the bands of amorphous materials and in particular Biochars are relatively recents and there is still an opening debate about the classification and the mechanisms of resonance scatterings. In general we can assume that each of discovered and hypotized photon scattering between the range of wavelenght from around 1200 cm-1 to 1600 cm-1, mainly sp3-sp3, sp2-sp2 and A-edges vibrations, could have a small or large impact in the formation of Raman spectrum. Unfortunately the singular mechanism in the shape of Biochar spectra is pratically unidentifiable due to the large number of scatterings, extreme band broadening. Furthermore, the process of fitting, made with our software implemented in MatLab, acts only in a mathematical way and so we can't trust in it when we have to make physical assumptions. However,we had also taken in account the intrinsic inconsistency of amorphous materials produced by pyrolysis heating and the single-point Raman spectroscopy: we can't be sure that the signal represents the values of carbonizations the chemical composition and the electronic state of the entire material. This is one of the reason why we analyse more samples produced in similar or even identical ways, and for every sample we took at least two different signals in two different regions. This give us more confidence and lead to more significant conclusions. At the end of the day, we find no distinguishable differences and peculiarities between Biochars produced with slightly different methods of productions (mostly differences in time and contaminants) and different wood derivation. Instead, the Nominal Highest Treatment Temperature represent a pretty characterizable feature when we study the Raman spectra of Biochars. We can see clear evidence in the evaluation of fluorescence of a sample: at higher temperature the material undergo

to a deeper process of carbonization and crystallization, losing its original organic aspect, therefore we notice a reduction of the photoluminesce in the material. More accurately, we find a clear and coherent path in the evolution of the Raman spectrum of every Biochar. Evaluating the Id/Ig ratio as the sum of every function in the range of the so-called D band divided by the sum of every function in the range of the so-called G band we see a regular and constant increment of this factor between the range of 350 C to 750 C. In parallel we notice a complementar narrowing of the width of each component of the spectrum whit the increasing of the temperature of production, even in this case from 350 C to 750 C. Finally, in order to avvalorate our suppositions, we study the signal of Biochar made at much higher temperatures, for example 1500 C or 2200 C, and we acknowledge beyond a shadow of a doubt the progresses of and the evolutions of the Raman spectra of Biochars. The process of graphitization and crystallization become a lot more clear and this mean more order and as a consequence we obtain a more detailed spectrum with more and narrower peaks.

Appendix A

Physics formulas

A.1 Terms of polarizability tensor resulting from the Herzberg-Teller coupling simplifications

$$
A^I = \frac{1}{\hbar} \sum_{e^r v^r \neq e^g v^i, e^f v^f} \left\{ \frac{\langle v^f | (p_\rho)^0_{e^f e^r} | v^r \rangle \langle v^r | (p_\sigma)^0_{e^r e^g} | v^i \rangle}{\omega_{e^r v^r : e^g v^i} - \omega_1 - i\Gamma_{e^r v^r}} \right.
$$
$$
\left. + \frac{\langle v^f | (p_\sigma)^0_{e^f e^r} | v^r \rangle \langle v^r | (p_\rho)^0_{e^r e^g} | v^i \rangle}{\omega_{e^r v^r : e^f v^f} + \omega_1 + i\Gamma_{e^r v^r}} \right\} \quad (A.1)
$$

$$
B^I = \frac{1}{\hbar^2} \sum_{e^r v^r \neq e^g v^i, e^f v^f} \left\{ \frac{\langle v^f | \sum_{e^s \neq e^r} \sum_k (p_\rho)^0_{e^f e^s} \frac{h^k_{e^s e^r}}{\omega_{e^r} - \omega_{e^s}} Q_k | v^r \rangle \langle v^r | (p_\sigma)^0_{e^r e^g} | v^i \rangle}{\omega_{e^r v^r : e^g v^i} - \omega_1 - i\Gamma_{e^r v^r}} \right.
$$
$$
\left. + \frac{\langle v^f | \sum_{e^s \neq e^r} \sum_k (p_\sigma)^0_{e^f e^s} \frac{h^k_{e^s e^r}}{\omega_{e^r} - \omega_{e^s}} Q_k | v^r \rangle \langle v^r | (p_\rho)^0_{e^r e^g} | v^i \rangle}{\omega_{e^r v^r : e^f v^f} + \omega_1 + i\Gamma_{e^r v^r}} \right\}
$$
$$
+ \frac{1}{\hbar^2} \sum_{e^r v^r \neq e^g v^i, e^f v^f} \left\{ \frac{\langle v^f | (p_\rho)^0_{e^f e^r} | v^r \rangle \langle v^r | \sum_{e^s \neq e^r} \sum_k \frac{h^k_{e^s e^r}}{\omega_{e^r} - \omega_{e^s}} Q_k (p_\sigma)^0_{e^s e^g} | v^i \rangle}{\omega_{e^r v^r : e^g v^i} - \omega_1 - i\Gamma_{e^r v^r}} \right.
$$
$$
\left. + \frac{\langle v^f | (p_\sigma)^0_{e^f e^r} | v^r \rangle \langle v^r | \sum_{e^s \neq e^r} \sum_k \frac{h^k_{e^s e^r}}{\omega_{e^r} - \omega_{e^s}} Q_k (p_\rho)^0_{e^s e^g} | v^i \rangle}{\omega_{e^r v^r : e^f v^f} + \omega_1 + i\Gamma_{e^r v^r}} \right\} \quad (A.2)
$$

$$
C^I = \frac{1}{\hbar^2} \sum_{e^r v^r \neq e^g v^i, e^f v^f} \left\{ \frac{\langle v^f | \sum_{e^t \neq e^f} \sum_k \frac{h^k_{e^f e^t}}{\omega_{e^f} - \omega_{e^t}} Q_k (p_\rho)^0_{e^t e^r} | v^r \rangle \langle v^r | (p_\sigma)^0_{e^r e^g} | v^i \rangle}{\omega_{e^r v^r : e^g v^i} - \omega_1 - i\Gamma_{e^r v^r}} \right.
$$
$$
\left. + \frac{\langle v^f | \sum_{e^t \neq e^f} \sum_k \frac{h^k_{e^f e^t}}{\omega_{e^f} - \omega_{e^t}} Q_k (p_\sigma)^0_{e^t e^r} | v^r \rangle \langle v^r | (p_\rho)^0_{e^r e^g} | v^i \rangle}{\omega_{e^r v^r : e^f v^f} + \omega_1 + i\Gamma_{e^r v^r}} \right\}
$$
$$
+ \frac{1}{\hbar^2} \sum_{e^r v^r \neq e^g v^i, e^f v^f} \left\{ \frac{\langle v^f | (p_\rho)^0_{e^f e^r} | v^r \rangle \langle v^r | \sum_{e^t \neq e^g} \sum_k (p_\sigma)^0_{e^r e^t} \frac{h^k_{e^t e^g}}{\omega_{e^g} - \omega_{e^t}} Q_k | v^i \rangle}{\omega_{e^r v^r : e^g v^i} - \omega_1 - i\Gamma_{e^r v^r}} \right.
$$
$$
\left. + \frac{\langle v^f | (p_\sigma)^0_{e^f e^r} | v^r \rangle \langle v^r | \sum_{e^s \neq e^r} \sum_k (p_\rho)^0_{e^r e^t} \frac{h^k_{e^t e^g}}{\omega_{e^g} - \omega_{e^t}} Q_k | v^i \rangle}{\omega_{e^r v^r : e^f v^f} + \omega_1 + i\Gamma_{e^r v^r}} \right\} \quad (A.3)
$$

$$D^{I} = \frac{1}{\hbar^3} \sum_{e^r v^r \neq e^g v^i, e^f v^f} \left\{ \frac{\langle v^f | \sum_{e^s \neq e^r} \sum_k (p_\rho)^0_{e^f e^s} \frac{h^k_{e^s e^r}}{\omega_{e^r} - \omega_{e^s}} Q_k |v^r\rangle \langle v^r | \sum_{e^{s'} \neq e^r} \sum_{k'} \frac{h^{k'}_{e^r e^{s'}}}{\omega_{e^r} - \omega_{e^{s'}}} Q_{k'} (p_\sigma)^0_{e^{s'} e^g} |v^i\rangle}{\omega_{e^r v^r : e^g v^i} - \omega_1 - i\Gamma_{e^r v^r}} \right.$$

$$\left. + \frac{\langle v^f | \sum_{e^{s'} \neq e^r} \sum_{k'} (p_\sigma)^0_{e^f e^{s'}} \frac{h^{k'}_{e^{s'} e^r}}{\omega_{e^r} - \omega_{e^{s'}}} Q_{k'} |v^r\rangle \langle v^r | \sum_{e^s \neq e^r} \sum_k \frac{h^k_{e^r e^s}}{\omega_{e^r} - \omega_{e^s}} Q_k (p_\rho)^0_{e^s e^g} |v^i\rangle}{\omega_{e^r v^r : e^f v^f} + \omega_1 + i\Gamma_{e^r v^r}} \right\}$$

(A.4)

A.2 Terms of polarizability tensor resulting from the separation of vibrational terms from the electronic terms

$$A^{II} = \frac{1}{\hbar} \sum_{e^r v^r \neq e^g v^i, e^f v^f} \left\{ \frac{(p_\rho)^0_{e^f e^r} (p_\sigma)^0_{e^r e^g}}{\omega_{e^r v^r : e^g v^i} - \omega_1 - i\Gamma_{e^r v^r}} \right.$$

$$\left. + \frac{(p_\sigma)^0_{e^f e^r} (p_\rho)^0_{e^r e^g}}{\omega_{e^r v^r : e^f v^f} + \omega_1 + i\Gamma_{e^r v^r}} \right\} \langle v^f | v^r \rangle \langle v^r | v^i \rangle \quad \text{(A.5)}$$

$$B^{II} = \frac{1}{\hbar^2} \sum_{e^r v^r \neq e^g v^i, e^f v^f} \sum_{e^s \neq e^r} \sum_k \left\{ \frac{(p_\rho)^0_{e^f e^s} h^k_{e^s e^r} (p_\sigma)^0_{e^r e^g}}{(\omega_{e^r} - \omega_{e^s})(\omega_{e^r v^r : e^g v^i} - \omega_1 - i\Gamma_{e^r v^r})} \right.$$

$$\left. + \frac{(p_\sigma)^0_{e^f e^s} h^k_{e^s e^r} (p_\rho)^0_{e^r e^g}}{(\omega_{e^r} - \omega_{e^s})(\omega_{e^r v^r : e^f v^f} + \omega_1 + i\Gamma_{e^r v^r})} \right\} \langle v^f | Q_k | v^r \rangle \langle v^r | v^i \rangle$$

$$+ \frac{1}{\hbar^2} \sum_{e^r v^r \neq e^g v^i, e^f v^f} \sum_{e^s \neq e^r} \sum_k \left\{ \frac{(p_\rho)^0_{e^f e^r} h^k_{e^r e^s} (p_\sigma)^0_{e^s e^g}}{(\omega_{e^r} - \omega_{e^s})(\omega_{e^r v^r : e^g v^i} - \omega_1 - i\Gamma_{e^r v^r})} \right.$$

$$\left. + \frac{(p_\rho)^0_{e^f e^r} h^k_{e^r e^s} (p_\sigma)^0_{e^s e^g}}{(\omega_{e^r} - \omega_{e^s})(\omega_{e^r v^r : e^f v^f} + \omega_1 + i\Gamma_{e^r v^r})} \right\} \langle v^f | v^r \rangle \langle v^r | Q_k | v^i \rangle \quad \text{(A.6)}$$

$$C^{II} = \frac{1}{\hbar^2} \sum_{e^r v^r \neq e^g v^i, e^f v^f} \sum_{e^t \neq e^f e^g} \sum_k \left\{ \frac{h^k_{e^f e^t} (p_\rho)^0_{e^t e^r} (p_\sigma)^0_{e^r e^g}}{(\omega_{e^f} - \omega_{e^t})(\omega_{e^r v^r : e^g v^i} - \omega_1 - i\Gamma_{e^r v^r})} \right.$$

$$\left. + \frac{h^k_{e^f e^t} (p_\sigma)^0_{e^t e^r} (p_\rho)^0_{e^r e^g}}{(\omega_{e^f} - \omega_{e^t})(\omega_{e^r v^r : e^f v^f} + \omega_1 + i\Gamma_{e^r v^r})} \right\} \langle v^f | Q_k | v^r \rangle \langle v^r | v^i \rangle$$

$$+ \frac{1}{\hbar^2} \sum_{e^r v^r \neq e^g v^i, e^f v^f} \sum_{e^s \neq e^r} \sum_k \left\{ \frac{(p_\rho)^0_{e^f e^r} (p_\sigma)^0_{e^r e^t} h^k_{e^t e^g}}{(\omega_{e^g} - \omega_{e^t})(\omega_{e^r v^r : e^g v^i} - \omega_1 - i\Gamma_{e^r v^r})} \right.$$

$$\left. + \frac{(p_\sigma)^0_{e^f e^r} (p_\rho)^0_{e^r e^t} h^k_{e^t e^g}}{(\omega_{e^g} - \omega_{e^t})(\omega_{e^r v^r : e^f v^f} + \omega_1 + i\Gamma_{e^r v^r})} \right\} \langle v^f | v^r \rangle \langle v^r | Q_k | v^i \rangle \quad \text{(A.7)}$$

$$
\begin{aligned}
\mathrm{D}^{\mathrm{II}} = \frac{1}{\hbar^3} &\sum_{e^r v^r \neq e^g v^i, e^f v^f} \sum_{e^s e^{s\prime} \neq e^r} \sum_{k,k\prime} \Bigg\{ \frac{(p_\rho)^0_{e^f e^s} h^k_{e^s e^r} h^{k\prime}_{e^r e^{s\prime}} (p_\sigma)^0_{e^{s\prime} e^g} \langle v^f | Q_k | v^r \rangle \langle v^r | Q_{k\prime} | v^i \rangle}{(\omega_{e^r} - \omega_{e^s})(\omega_{e^r} - \omega_{e^{s\prime}})(\omega_{e^r v^r : e^g v^i} - \omega_1 - i\Gamma_{e^r v^r})} \\
&+ \frac{(p_\sigma)^0_{e^f e^{s\prime}} h^{k\prime}_{e^{s\prime} e^r} h^k_{e^r e^s} (p_\rho)^0_{e^s e^g} \langle v^f | Q_{k\prime} | v^r \rangle \langle v^r | Q_k | v^i \rangle}{(\omega_{e^r} - \omega_{e^{s\prime}})(\omega_{e^r} - \omega_{e^s})(\omega_{e^r v^r : e^f v^f} + \omega_1 + i\Gamma_{e^r v^r})} \Bigg\} \langle v^f | Q_k | v^r \rangle \langle v^r | v^i \rangle
\end{aligned}
$$

$$(\mathrm{A}.8)$$

Appendix B

Biochar data

	Sample description	Sample i/d			Sample description	Sample i/d
1		BX-20130621		45		1009/171/350
2	OSR700	BX-20130828		46	willow	1009/171/550
3		BX-20130508		47		1009/171/750
4	OSR550	BX-20130220		48		1009/177/350
5		BX-20130204		49	willow	1009/177/550
6		BX-20130315		50		1009/177/750
7	WSP550	BX-20130306		51		1011/3/350
8		BX-20131125		52	willow	1011/3/550
9		BX-20130429		53		1011/3/750
10	WSP700	BX-20130513		54		1011/9/350
11		BX-20131205		55	miscanthus	1011/9/550
12		BX-20131021		56		1011/9/750
13	RH550	BX-20130520		57		1011/17/350
14		BX-20130628		58	miscanthus	1011/17/550
15		BX-20130517		59		1011/17/750
16		BX-20130626		60		1011/23/350
17	RH700	BX-20130701		61	miscanthus	1011/23/550
18		BX-20130627		62		1011/23/750
19		BX-20130530		63	willow	1017/5A
20		BX-20130325		64		1017/9A
21	MSP550	BX-20130329		65	miscanthus	1017/13A
22		BX-20130605		66		1017/17A
23	MSP700	drum 10		67		Pine nc1
24		drum 1		68		Pine nc9
25	SWP550	drum 4		69		Pine nc19
26		drum 19		70		PKS nc1
27		BX-20130823		71		PKS nc6
28		BX-20130819				
29	SWP700	BX-20130617				
30		BX-20130424				
31		BX-20130410				
32		BX-20130415				
33		SS30-1				
34		SS30-2				
35		SS30-3				
36		SS25-1				
37		SS25-2				
38	SS	SS25-3				
39		SS26-1				
40		SS26-2				
41		SS26-3				
42		SS24-1				
43		SS24-2				
44		SS24-3				

FIGURE B.1: Biochar list

UK Biochar Research Centre
reducing and removing CO$_2$ while improving soils: a significant and sustainable response to climate change

www.biochar.ac.uk | biochar@ed.ac.uk

MSP550
Standard biochar specification sheet – Version 1.0 | November 2014

Feedstock: Miscanthus Straw Pellets | **Production:** Pilot-scale rotary kiln pyrolysis unit, nominal peak temperature 550°C

Key features: • Reproducible   • Extensively characterised   • Readily available

Biochar C stability compared to a set of 92 biochar

Basic Utility Properties		Mean	Run-to-Run Variation, SD(n)
Moisture[a]	wt% (a.r.)	1.83	0.12 (4)
C$_{tot}$	wt% (d.b.)	75.41	2.75 (4)
H	wt% (d.b.)	2.42	0.30 (4)
O (by difference)	wt% (d.b.)	9.24	2.30 (4)
H:C$_{tot}$	Molar ratio	0.38	0.04 (4)
O:C$_{tot}$	Molar ratio	0.09	0.03 (4)
C$_{org}$	wt% (d.b.)	tbd	tbd
H:C$_{org}$	Molar ratio	tbd	tbd
Total ash[a]	wt% (d.b.)	12.15	1.00 (4)
Total N	wt% (d.b.)	0.78	0.09 (4)
pH	[-]	9.77	0.21 (4)
Electric conductivity	dS/m	0.82	0.18 (4)
Liming (if pH above 7)	% CaCO$_3$	tbd	tbd
Biochar C stability[b]	% C-basis	94.92	0.65 (4)

Production parameters		Mean	Run-to-Run Variation, SD(n)
Nominal HTT	°C	550	- (1)
Reactor wall temp.	°C	550	- (1)
Max. char HTT	°C	554	- (1)
Heating rate	°C/min	65	- (1)
Kiln residence time	min	12	- (1)
Mean time at HTT	min	3.9	- (1)
Biochar yield	wt% (d.b.)	22.81	1.60 (4)
Pyrolysis liquid yield	wt% (d.b.)	41.00	- (1)
Pyrolysis gas yield	wt% (d.b.)	34.12	- (1)
Pyrolysis liquid HHV	MJ/kg	0.37	- (1)
Pyrolysis gas HHV	MJ/kg	9.37	- (1)

Advanced Analysis & Soil Enhancement Properties		Mean	Run-to-Run Variation, SD(n)
Mineral N (ammonium & nitrate)	mg/kg (d.b)	<3	- (4)
Total P[c]	wt% (d.b.)	0.19	0.04 (4)
Total K[c]	wt% (d.b.)	0.95	0.08 (4)
Available P	mg/kg (d.b.)	tbd	tbd
Volatile Matter[a]	wt% (d.b.)	11.62	1.54 (4)
Total Surface Area	m^2/g (d.b.)	33.6	- (1)
External Surface Area	m^2/g (d.b.)	tbd	tbd

Toxicant Reporting - Total Content		Mean	Run-to-Run Variation, SD(n)		IBI	EBC (premium)	BQM (high grade)
Germination Inhibition Assay	pass/fail	tbd	tbd				
Polycyclic Aromatic Hydrocarbons (EPA16)[d]	mg/kg dry wt	0.53	0.28 (4)		6-20	4	20
Dioxin/ Furan (PCDD/ Fs)[e]	ng/kg dry wt	2.70	- (1)		9	20	20
Polychlorinated Biphenyls (PCBs)[f]	ng/kg dry wt	0.04	- (1)		0.2-0.5	0.2	0.50
As	mg/kg dry wt	1.35	0.62 (3)		12-100	n/a	10
Cd	mg/kg dry wt	0.71	0.97 (3)		1.4-39	1	3
Cr	mg/kg dry wt	8.67	3.32 (3)		64-1200	80	15
Co	mg/kg dry wt	2.69	2.02 (3)		40-150	n/a	n/a
Cu	mg/kg dry wt	26.64	37.87 (3)		63-1500	100	40
Pb	mg/kg dry wt	bdl	- (3)		70-500	120	60
Hg	mg/kg dry wt	bdl	- (3)		1-17	1	1
Mo	mg/kg dry wt	7.90	6.25 (3)		5-20	n/a	10
Ni	mg/kg dry wt	4.95	2.01 (3)		47-600	30	10
Se	mg/kg dry wt	bdl	- (3)		1-36	n/a	5
Zn	mg/kg dry wt	63.40	30.35 (3)		200-7000	400	150

(As through Zn: modified dry ashing followed by ICP-OES; IBI/EBC/BQM: comparison vs. recommended standard thresholds+)

Notes: HTT=highest treatment temperature, HHV = higher heating value, tbd = to be defined in next version, bdl. = below detection limit, SD = standard deviation (refers to run-to-run consistency, not analytical error) + available standards related to biochar (IBI = International Biochar Initiative, EBC = European Biochar Standard, BQM = Biochar Quality Mandate), ^{e} as TEQ (toxic equivalent) values were bdl, total (tetra to octa chlorinated) dioxin/furan content is reported instead.

(a) TGA, (b) Cross A, Sohi SP (2013), (c) Aqua Regia digestion followed by ICP, (d) Soxhlet extraction (toluene, 6h) determination by GCMS, (e) US EPA 1613, (f) AES O84 (based on US EPA 1668)

For full details please go to: http://www.charchive.org/record.php?record_id=97

UK Biochar Research Centre

reducing and removing CO₂ while improving soils: a significant and sustainable response to climate change

www.biochar.ac.uk | biochar@ed.ac.uk

MSP700

Standard biochar specification sheet – Version 1.0 | November 2014

Feedstock: Miscanthus Straw Pellets | **Production:** Pilot-scale rotary kiln pyrolysis unit, nominal peak temperature700°C

Key features: ● Reproducible ● Extensively characterised ● Readily available

Biochar C stability compared to a set of 92 biochar

Basic Utility Properties		Mean	Run-to-Run Variation, SD(n)
Moisture[a]	wt% (a.r.)	2.23	0.06 (2)
C_{tot}	wt% (d.b.)	79.18	0.07 (2)
H	wt% (d.b.)	1.26	0.12 (2)
O (by difference)	wt% (d.b.)	6.99	0.19 (2)
$H:C_{tot}$	Molar ratio	0.19	0.02 (4)
$O:C_{tot}$	Molar ratio	0.07	0.00 (2)
C_{org}	wt% (d.b.)	tbd	tbd
$H:C_{org}$	Molar ratio	tbd	tbd
Total ash[a]	wt% (d.b.)	11.55	0.17 (2)
Total N	wt% (d.b.)	1.03	0.03 (2)
pH	[-]	9.72	0.30 (4)
Electric conductivity	dS/m	1.91	0.27 (4)
Liming (if pH above 7)	% CaCO₃	tbd	tbd
Biochar C stability[b]	% C-basis	98.93	0.14 (3)

Production parameters		Mean	Run-to-Run Variation, SD(n)
Nominal HTT	°C	700	- (1)
Reactor wall temp.	°C	700	- (1)
Max. char HTT	°C	tbd	tbd
Heating rate	°C/min	80	- (1)
Kiln residence time	min	12	- (1)
Mean time at HTT	min	tbd	tbd
Biochar yield	wt% (d.b.)	21.07	0.11 (2)
Pyrolysis liquid yield	wt% (d.b.)	33.69	- (1)
Pyrolysis gas yield	wt% (d.b.)	44.29	- (1)
Pyrolysis liquid HHV	MJ/kg	2.29	- (1)
Pyrolysis gas HHV	MJ/kg	12.42	- (1)

Advanced Analysis & Soil Enhancement Properties		Mean	Run-to-Run Variation, SD(n)
Mineral N (ammonium & nitrate)	mg/kg (d.b.)	<3	- (2)
Total P[c]	wt% (d.b.)	0.76	0.45 (4)
Total K[c]	wt% (d.b.)	2.60	0.75 (4)
Available P	mg/kg (d.b.)	tbd	tbd
Volatile Matter[a]	wt% (d.b.)	7.71	0.10 (2)
Total Surface Area	m²/g (d.b.)	37.2	- (1)
External Surface Area	m²/g (d.b.)	tbd	tbd

Toxicant Reporting - Total Content		Mean	Run-to-Run Variation, SD(n)		IBI	EBC (premium)	BQM (high grade)
Germination Inhibition Assay	pass/fail	tbd	tbd				
Polycyclic Aromatic Hydrocarbons (EPA16)[d]	mg/kg dry wt	0.12	0.01 (2)		6-20	4	20
Dioxin/ Furan (PCDD/ Fs)[e]	ng/kg dry wt	3.90	- (1)		9	20	20
Polychlorinated Biphenyls (PCBs)[f]	ng/kg dry wt	0.00	- (1)		0.2-0.5	0.2	0.50
As	mg/kg dry wt	1.60	1.41 (3)		12-100	n/a	10
Cd	mg/kg dry wt	4.58	7.67 (3)		1.4-39	1	3
Cr	mg/kg dry wt	36.14	9.99 (3)		64-1200	80	15
Co	mg/kg dry wt	3.91	2.63 (3)		40-150	n/a	n/a
Cu	mg/kg dry wt	5.88	0.79 (3)		63-1500	100	40
Pb	mg/kg dry wt	bdl	- (3)		70-500	120	60
Hg	mg/kg dry wt	bdl	- (3)		1-17	1	1
Mo	mg/kg dry wt	22.63	14.97 (3)		5-20	n/a	10
Ni	mg/kg dry wt	30.40	3.86 (3)		47-600	30	10
Se	mg/kg dry wt	bdl	- (3)		1-36	n/a	5
Zn	mg/kg dry wt	44.53	16.61 (3)		200-7000	400	150

(toxicant elements: modified dry ashing followed by ICP-OES; comparison vs. recommended standard thresholds+)

Notes: HTT=highest treatment temperature, HHV = higher heating value, tbd = to be defined in next version, bdl. = below detection limit, SD = standard deviation (refers to run-to-run consistency, not analytical error) + available standards related to biochar (IBI = International Biochar Initiative, EBC = European Biochar Standard, BQM = Biochar Quality Mandate), ᵉ as TEQ (toxic equivalent) values were bdl, total (tetra to octa chlorinated) dioxin/furan content is reported instead.

(a) TGA, (b) Cross A, Sohi SP (2013), (c) Aqua Regia digestion followed by ICP, (d) Soxhlet extraction (toluene, 6h) determination by GCMS, (e) US EPA 1613, (f) AES O84 (based on US EPA 1668)

For full details please go to: http://www.charchive.org/record.php?record_id=96
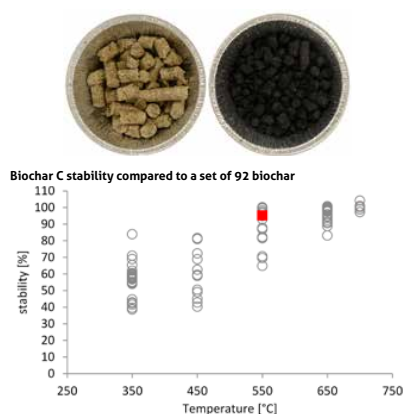
UK Biochar Research Centre

reducing and removing CO₂ while improving soils: a significant and sustainable response to climate change

www.biochar.ac.uk | biochar@ed.ac.uk

OSR550

Standard biochar specification sheet – Version 1.0 | November 2014

Feedstock: Oil Seed Rape Straw Pellets | **Production:** Pilot-scale rotary kiln pyrolysis unit, nominal peak temp. 550°C

Key features: ● Reproducible ● Extensively characterised ● Readily available

Biochar C stability compared to a set of 92 biochar

Basic Utility Properties		Mean	Run-to-Run Variation, SD(n)
Moisture[a]	wt% (a.r.)	2.61	0.49 (8)
C_{tot}	wt% (d.b.)	68.85	2.26 (4)
H	wt% (d.b.)	1.82	0.22 (4)
O (by difference)	wt% (d.b.)	8.91	1.30 (4)
$H:C_{tot}$	Molar ratio	0.32	0.03 (4)
$O:C_{tot}$	Molar ratio	0.10	0.02 (4)
C_{org}	wt% (d.b.)	tbd	tbd
$H:C_{org}$	Molar ratio	tbd	tbd
Total ash[a]	wt% (d.b.)	19.50	2.16 (8)
Total N	wt% (d.b.)	1.59	0.22 (4)
pH	[-]	9.78	0.47 (4)
Electric conductivity	dS/m	2.27	0.38 (4)
Liming (if pH above 7)	% CaCO₃	tbd	tbd
Biochar C stability[b]	% C-basis	97.31	0.25 (5)

Production parameters		Mean	Run-to-Run Variation, SD(n)
Nominal HTT	°C	550	- (1)
Reactor wall temp.	°C	550	- (1)
Max. char HTT	°C	553	- (1)
Heating rate	°C/min	78	- (1)
Kiln residence time	min	12	- (1)
Mean time at HTT	min	5	- (1)
Biochar yield	wt% (d.b.)	28.87	0.78 (2)
Pyrolysis liquid yield	wt% (d.b.)	tbd	tbd
Pyrolysis gas yield	wt% (d.b.)	tbd	tbd
Pyrolysis liquid HHV	MJ/kg	1.35	- (1)
Pyrolysis gas HHV	MJ/kg	9.52	- (1)

Advanced Analysis & Soil Enhancement Properties		Mean	Run-to-Run Variation, SD(n)
Mineral N (ammonium & nitrate)	mg/kg (d.b.)	<3	- (2)
Total P[c]	wt% (d.b.)	0.29	0.08 (4)
Total K[c]	wt% (d.b.)	2.86	0.26 (4)
Available P	mg/kg (d.b.)	tbd	tbd
Volatile Matter[a]	wt% (d.b.)	16.38	2.78 (8)
Total Surface Area	m²/g (d.b.)	7.3	- (1)
External Surface Area	m²/g (d.b.)	tbd	tbd

Toxicant Reporting - Total Content		Mean	Run-to-Run Variation, SD(n)		IBI	EBC (premium)	BQM (high grade)
Germination Inhibition Assay	pass/fail	tbd	tbd				
Polycyclic Aromatic Hydrocarbons (EPA16)[d]	mg/kg dry wt	0.54	0.16 (2)		6-20	4	20
Dioxin/ Furan (PCDD/ Fs)[e]	ng/kg dry wt	6.8	- (1)		9	20	20
Polychlorinated Biphenyls (PCBs)[f]	ng/kg dry wt	0.001	- (1)		0.2-0.5	0.2	0.50
As	mg/kg dry wt	1.09	0.78 (3)		12-100	n/a	10
Cd	mg/kg dry wt	1.76	1.57 (3)		1.4-39	1	3
Cr	mg/kg dry wt	bdl	- (3)		64-1200	80	15
Co	mg/kg dry wt	3.06	0.28 (3)		40-150	n/a	n/a
Cu	mg/kg dry wt	7.86	2.38 (3)		63-1500	100	40
Pb	mg/kg dry wt	17.62	15.99 (3)		70-500	120	60
Hg	mg/kg dry wt	bdl	- (3)		1-17	1	1
Mo	mg/kg dry wt	1.29	0.34 (3)		5-20	n/a	10
Ni	mg/kg dry wt	2.49	0.74 (3)		47-600	30	10
Se	mg/kg dry wt	bdl	- (3)		1-36	n/a	5
Zn	mg/kg dry wt	7.22	2.93 (3)		200-7000	400	150

(modified dry ashing followed by ICP-OES)

(comparison vs. recommended standard thresholds+)

Notes: HTT=highest treatment temperature, HHV = higher heating value, tbd = to be defined in next version, bdl. = below detection limit, SD = standard deviation (refers to run-to-run consistency, not analytical error) + available standards related to biochar (IBI = International Biochar Initiative, EBC = European Biochar Standard, BQM = Biochar Quality Mandate), ᵉ as TEQ (toxic equivalent) values were bdl, total (tetra to octa chlorinated) dioxin/furan content is reported instead.

(a) TGA, (b) Cross A, Sohi SP (2013), (c) Aqua Regia digestion followed by ICP, (d) Soxhlet extraction (toluene, 6h) determination by GCMS, (e) US EPA 1613, (f) AES O84 (based on US EPA 1668)

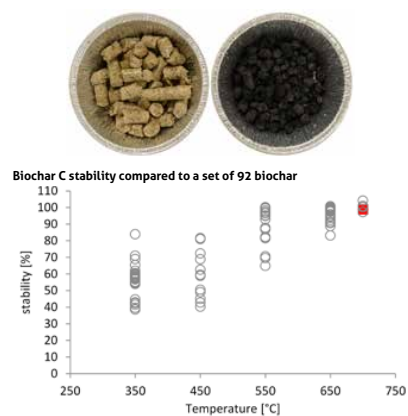For full details please go to: http://www.charchive.org/record.php?record_id=98
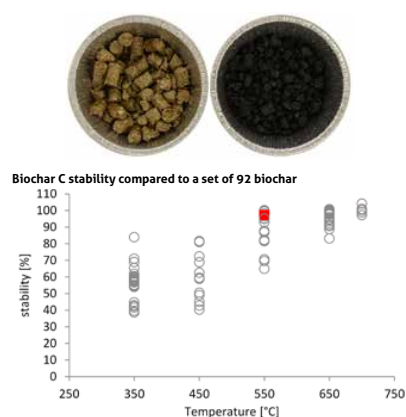
UK Biochar Research Centre
reducing and removing CO₂ while improving soils: a significant and sustainable response to climate change

www.biochar.ac.uk | biochar@ed.ac.uk

OSR700
Standard biochar specification sheet – Version 1.0 | November 2014

Feedstock: Oil Seed Rape Straw Pellets | **Production:** Pilot-scale rotary kiln pyrolysis unit, nominal peak temp. 700°C

Key features: ● Reproducible ● Extensively characterised ● Readily available

Biochar C stability compared to a set of 92 biochar

Basic Utility Properties		Mean	Run-to-Run Variation, SD(n)
Moisture[a]	wt% (a.r.)	3.63	0.73 (6)
C_{tot}	wt% (d.b.)	67.74	0.86 (5)
H	wt% (d.b.)	1.09	0.14 (5)
O (by difference)	wt% (d.b.)	7.84	1.23 (5)
$H:C_{tot}$	Molar ratio	0.19	0.02 (5)
$O:C_{tot}$	Molar ratio	0.09	0.02 (5)
C_{org}	wt% (d.b.)	tbd	tbd
$H:C_{org}$	Molar ratio	tbd	tbd
Total ash[a]	wt% (d.b.)	21.92	0.52 (6)
Total N	wt% (d.b.)	1.26	0.18 (5)
pH	[-]	10.41	0.49 (4)
Electric conductivity	dS/m	3.11	0.37 (4)
Liming (if pH above 7)	% CaCO₃	tbd	tbd
Biochar C stability[b]	% C-basis	104.17	0.19 (4)

Production parameters		Mean	Run-to-Run Variation, SD(n)
Nominal HTT	°C	700	- (1)
Reactor wall temp.	°C	700	- (1)
Max. char HTT	°C	677	- (1)
Heating rate	°C/min	103	- (1)
Kiln residence time	min	12	- (1)
Mean time at HTT	min	5.14	- (1)
Biochar yield	wt% (d.b.)	22.62	2.99 (3)
Pyrolysis liquid yield	wt% (d.b.)	tbd	tbd
Pyrolysis gas yield	wt% (d.b.)	tbd	tbd
Pyrolysis liquid HHV	MJ/kg	tbd	tbd
Pyrolysis gas HHV	MJ/kg	tbd	tbd

Advanced Analysis & Soil Enhancement Properties		Mean	Run-to-Run Variation, SD(n)
Mineral N (ammonium & nitrate)	mg/kg (d.b.)	<3	- (5)
Total P[c]	wt% (d.b.)	0.258	0.079 (5)
Total K[c]	wt% (d.b.)	2.98	0.396 (5)
Available P	mg/kg (d.b.)	tbd	tbd
Volatile Matter[a]	wt% (d.b.)	13.18	3.47 (6)
Total Surface Area	m²/g (d.b.)	25.20	- (1)
External Surface Area	m²/g (d.b.)	tbd	tbd

Toxicant Reporting - Total Content		Mean	Run-to-Run Variation, SD(n)		IBI	EBC (premium)	BQM (high grade)
Germination Inhibition Assay	pass/fail	tbd	tbd				
Polycyclic Aromatic Hydrocarbons (EPA16)[d]	mg/kg dry wt	<0.11	- (5)		6-20	4	20
Dioxin/ Furan (PCDD/ Fs)[e]	ng/kg dry wt	4.50	- (1)		9	20	20
Polychlorinated Biphenyls (PCBs)[f]	ng/kg dry wt	0.001	- (1)		0.2-0.5	0.2	0.50
As	mg/kg dry wt	1.09	0.79 (3)		12-100	n/a	10
Cd	mg/kg dry wt	2.98	0.13 (3)		1.4-39	1	3
Cr	mg/kg dry wt	4.36	0.95 (3)		64-1200	80	15
Co	mg/kg dry wt	3.17	0.17 (3)		40-150	n/a	n/a
Cu	mg/kg dry wt	13.78	0.93 (3)		63-1500	100	40
Pb	mg/kg dry wt	bdl	- (3)		70-500	120	60
Hg	mg/kg dry wt	bdl	- (3)		1-17	1	1
Mo	mg/kg dry wt	1.68	0.14 (3)		5-20	n/a	10
Ni	mg/kg dry wt	3.27	0.22 (3)		47-600	30	10
Se	mg/kg dry wt	bdl	- (3)		1-36	n/a	5
Zn	mg/kg dry wt	8.80	0.24 (3)		200-7000	400	150

(As through Zn: modified dry ashing followed by ICP-OES; comparison vs. recommended standard thresholds +)

Notes: HTT=highest treatment temperature, HHV = higher heating value, tbd = to be defined in next version, bdl. = below detection limit, SD = standard deviation (refers to run-to-run consistency, not analytical error) + available standards related to biochar (IBI = International Biochar Initiative, EBC = European Biochar Standard, BQM = Biochar Quality Mandate), ᵉ as TEQ (toxic equivalent) values were bdl, total (tetra to octa chlorinated) dioxin/furan content is reported instead.

(a) TGA, (b) Cross A, Sohi SP (2013), (c) Aqua Regia digestion followed by ICP, (d) Soxhlet extraction (toluene, 6h) determination by GCMS, (e) US EPA 1613, (f) AES O84 (based on US EPA 1668)

For full details please go to: http://www.charchive.org/record.php?record_id=99

UK Biochar Research Centre

reducing and removing CO₂ while improving soils: a significant and sustainable response to climate change

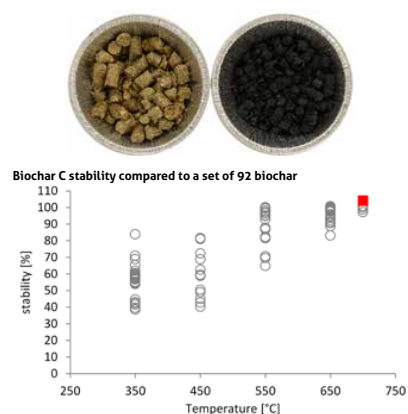www.biochar.ac.uk | biochar@ed.ac.uk

RH550

Standard biochar specification sheet – Version 1.0 | November 2014

Feedstock: Rice Husk | **Production:** Pilot-scale rotary kiln pyrolysis unit, nominal peak temperature 550°C

Key features: ● Reproducible ● Extensively characterised ● Readily available

Basic Utility Properties		Mean	Run-to-Run Variation, SD(n)
Moisture[a]	wt% (a.r.)	1.54	0.30 (8)
C_{tot}	wt% (d.b.)	48.69	2.37 (5)
H	wt% (d.b.)	1.24	0.12 (5)
O (by difference)	wt% (d.b.)	2.47	0.37 (4)
$H:C_{tot}$	Molar ratio	0.28	0.06 (6)
$O:C_{tot}$	Molar ratio	0.04	0.01 (4)
C_{org}	wt% (d.b.)	tbd	tbd
$H:C_{org}$	Molar ratio	tbd	tbd
Total ash[a]	wt% (d.b.)	47.93	5.43 (8)
Total N	wt% (d.b.)	1.04	0.09 (6)
pH	[-]	9.71	0.26 (4)
Electric conductivity	dS/m	0.48	0.14 (4)
Liming (if pH above 7)	% CaCO₃	tbd	tbd
Biochar C stability[b]	% C-basis	95.28	0.22 (5)

Biochar C stability compared to a set of 92 biochar

Advanced Analysis & Soil Enhancement Properties		Mean	Run-to-Run Variation, SD(n)
Mineral N (ammonium & nitrate)	mg/kg (d.b.)	<3	- (5)
Total P[c]	wt% (d.b.)	0.10	0.07 (4)
Total K[c]	wt% (d.b.)	0.39	0.17 (4)
Available P	mg/kg (d.b.)	tbd	tbd
Volatile Matter[a]	wt% (d.b.)	7.48	1.22 (8)
Total Surface Area	m²/g (d.b.)	20.10	- (1)
External Surface Area	m²/g (d.b.)	tbd	tbd

Production parameters		Mean	Run-to-Run Variation, SD(n)
Nominal HTT	°C	550	- (1)
Reactor wall temp.	°C	550	- (1)
Max. char HTT	°C	556	- (1)
Heating rate	°C/min	98	- (1)
Kiln residence time	min	15	- (1)
Mean time at HTT	min	8.5	- (1)
Biochar yield	wt% (d.b.)	37.20	5.11 (5)
Pyrolysis liquid yield	wt% (d.b.)	26.18	- (1)
Pyrolysis gas yield	wt% (d.b.)	46.04	- (1)
Pyrolysis liquid HHV	MJ/kg	0	- (1)
Pyrolysis gas HHV	MJ/kg	9.52	- (1)

Toxicant Reporting - Total Content		Mean	Run-to-Run Variation, SD(n)		IBI	EBC (premium)	BQM (high grade)
Germination Inhibition Assay	pass/fail	tbd	tbd				
Polycyclic Aromatic Hydrocarbons (EPA16)[d]	mg/kg dry wt	0.21	0.11 (5)		6-20	4	20
Dioxin/ Furan (PCDD/ Fs)[e]	ng/kg dry wt	5.10	- (1)		9	20	20
Polychlorinated Biphenyls (PCBs)[f]	ng/kg dry wt	0.00	- (1)		0.2-0.5	0.2	0.50
As	mg/kg dry wt	0.26	0.46 (3)		12-100	n/a	10
Cd	mg/kg dry wt	17.84	3.55 (3)		1.4-39	1	3
Cr	mg/kg dry wt	4.99	4.92 (3)		64-1200	80	15
Co	mg/kg dry wt	2.94	1.51 (3)		40-150	n/a	n/a
Cu	mg/kg dry wt	5.40	0.29 (3)		63-1500	100	40
Pb	mg/kg dry wt	bdl	- (3)		70-500	120	60
Hg	mg/kg dry wt	bdl	- (3)		1-17	1	1
Mo	mg/kg dry wt	0.64	0.46 (3)		5-20	n/a	10
Ni	mg/kg dry wt	3.00	2.29 (3)		47-600	30	10
Se	mg/kg dry wt	bdl	- (3)		1-36	n/a	5
Zn	mg/kg dry wt	23.58	4.44 (3)		200-7000	400	150

modified dry ashing followed by ICP-OES

comparison vs. recommended standard thresholds+

Notes: HTT=highest treatment temperature, HHV = higher heating value, tbd = to be defined in next version, bdl. = below detection limit, SD = standard deviation (refers to run-to-run consistency, not analytical error) + available standards related to biochar (IBI = International Biochar Initiative, EBC = European Biochar Standard, BQM = Biochar Quality Mandate), ᵉ as TEQ (toxic equivalent) values were bdl, total (tetra to octa chlorinated) dioxin/furan content is reported instead.

(a) TGA, (b) Cross A, Sohi SP (2013), (c) Aqua Regia digestion followed by ICP, (d) Soxhlet extraction (toluene, 6h) determination by GCMS, (e) US EPA 1613, (f) AES O84 (based on US EPA 1668)

For full details please go to: http://www.charchive.org/record.php?record_id=91
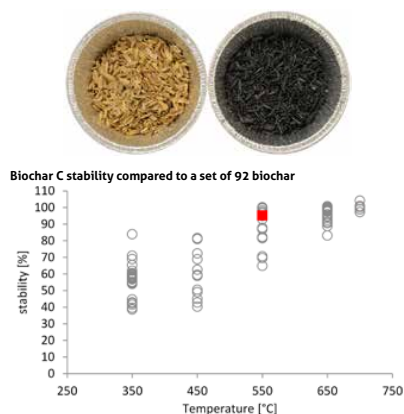
UK Biochar Research Centre

reducing and removing CO₂ while improving soils: a significant and sustainable response to climate change

www.biochar.ac.uk | biochar@ed.ac.uk

RH700

Standard biochar specification sheet – Version 1.0 | November 2014

Feedstock: Rice Husk | **Production:** Pilot-scale rotary kiln pyrolysis unit, nominal peak temperature 700°C

Key features: • Reproducible • Extensively characterised • Readily available

Biochar C stability compared to a set of 92 biochar

stability [%] vs Temperature [°C]

Basic Utility Properties		Mean	Run-to-Run Variation, SD(n)
Moisture[a]	wt% (a.r.)	1.49	0.41 (9)
C_{tot}	wt% (d.b.)	47.32	1.82 (4)
H	wt% (d.b.)	0.63	0.07 (4)
O (by difference)	wt% (d.b.)	2.06	1.11 (4)
$H:C_{tot}$	Molar ratio	0.16	0.01 (4)
$O:C_{tot}$	Molar ratio	0.03	0.02 (3)
C_{org}	wt% (d.b.)	tbd	tbd
$H:C_{org}$	Molar ratio	tbd	tbd
Total ash[a]	wt% (d.b.)	47.93	5.43 (9)
Total N	wt% (d.b.)	0.85	0.08 (4)
pH	[-]	9.81	0.64 (4)
Electric conductivity	dS/m	0.69	0.26 (4)
Liming (if pH above 7)	% CaCO₃	tbd	tbd
Biochar C stability[b]	% C-basis	100.18	0.27 (5)

Production parameters		Mean	Run-to-Run Variation, SD(n)
Nominal HTT	°C	700	- (1)
Reactor wall temp.	°C	700	- (1)
Max. char HTT	°C	680	- (1)
Heating rate	°C/min	92	- (1)
Kiln residence time	min	17	- (1)
Mean time at HTT	min	9	- (1)
Biochar yield	wt% (d.b.)	32.77	2.44 (4)
Pyrolysis liquid yield	wt% (d.b.)	tbd	- (1)
Pyrolysis gas yield	wt% (d.b.)	tbd	- (1)
Pyrolysis liquid HHV	MJ/kg	tbd	- (1)
Pyrolysis gas HHV	MJ/kg	tbd	- (1)

Advanced Analysis & Soil Enhancement Properties		Mean	Run-to-Run Variation, SD(n)
Mineral N (ammonium & nitrate)	mg/kg (d.b.)	<3	- (4)
Total P[c]	wt% (d.b.)	0.16	0.04 (4)
Total K[c]	wt% (d.b.)	0.62	0.16 (4)
Available P	mg/kg (d.b.)	tbd	tbd
Volatile Matter[a]	wt% (d.b.)	4.99	0.85 (9)
Total Surface Area	m²/g (d.b.)	42	- (1)
External Surface Area	m²/g (d.b.)	tbd	tbd

Toxicant Reporting - Total Content		Mean	Run-to-Run Variation, SD(n)		IBI	EBC (premium)	BQM (high grade)
Germination Inhibition Assay	pass/fail	tbd	tbd				
Polycyclic Aromatic Hydrocarbons (EPA16)[d]	mg/kg dry wt	0.34	0.16 (4)		6-20	4	20
Dioxin/ Furan (PCDD/ Fs)[e]	ng/kg dry wt	5.90	- (1)		9	20	20
Polychlorinated Biphenyls (PCBs)[f]	ng/kg dry wt	0.00	- (1)		0.2-0.5	0.2	0.50
As	mg/kg dry wt	bdl	- (3)		12-100	n/a	10
Cd	mg/kg dry wt	19.97	3.35 (3)		1.4-39	1	3
Cr	mg/kg dry wt	bdl	- (3)		64-1200	80	15
Co	mg/kg dry wt	4.59	0.53 (3)		40-150	n/a	n/a
Cu	mg/kg dry wt	26.93	30.20 (3)		63-1500	100	40
Pb	mg/kg dry wt	bdl	- (3)		70-500	120	60
Hg	mg/kg dry wt	bdl	- (3)		1-17	1	1
Mo	mg/kg dry wt	0.67	0.19 (3)		5-20	n/a	10
Ni	mg/kg dry wt	2.71	0.42 (3)		47-600	30	10
Se	mg/kg dry wt	bdl	- (3)		1-36	n/a	5
Zn	mg/kg dry wt	36.17	25.94 (3)		200-7000	400	150

(columns for elements As–Zn determined by: modified dry ashing followed by ICP-OES; right-hand IBI/EBC/BQM columns: comparison vs. recommended standard thresholds+)

Notes: HTT=highest treatment temperature, HHV = higher heating value, tbd = to be defined in next version, bdl. = below detection limit, SD = standard deviation (refers to run-to-run consistency, not analytical error) + available standards related to biochar (IBI = International Biochar Initiative, EBC = European Biochar Standard, BQM = Biochar Quality Mandate), ᵉ as TEQ (toxic equivalent) values were bdl, total (tetra to octa chlorinated) dioxin/furan content is reported instead.

(a) TGA, (b) Cross A, Sohi SP (2013), (c) Aqua Regia digestion followed by ICP, (d) Soxhlet extraction (toluene, 6h) determination by GCMS, (e) US EPA 1613, (f) AES O84 (based on US EPA 1668)

For full details please go to: http://www.charchive.org/record.php?record_id=92
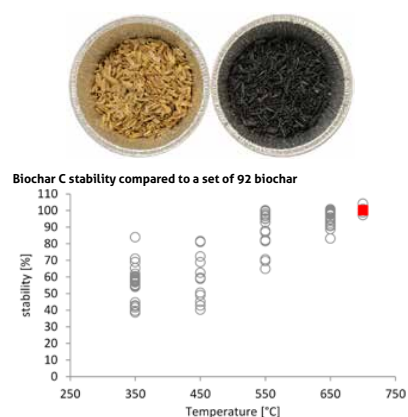
UK Biochar Research Centre
reducing and removing CO₂ while improving soils: a significant and sustainable response to climate change

www.biochar.ac.uk | biochar@ed.ac.uk

SWP550
Standard biochar specification sheet – Version 1.0 | November 2014

Feedstock: Soft Wood Pellets | **Production:** Pilot-scale rotary kiln pyrolysis unit, nominal peak temperature 550°C

Key features: • Reproducible • Extensively characterised • Readily available

Biochar C stability compared to a set of 92 biochar

Basic Utility Properties		Mean	Run-to-Run Variation, SD(n)
Moisture[a]	wt% (a.r.)	1.52	0.16 (8)
C_{tot}	wt% (d.b.)	85.52	1.22 (9)
H	wt% (d.b.)	2.77	0.09 (9)
O (by difference)	wt% (d.b.)	10.36	1.19 (9)
$H:C_{tot}$	Molar ratio	0.39	0.01 (9)
$O:C_{tot}$	Molar ratio	0.09	0.01 (9)
C_{org}	wt% (d.b.)	tbd	tbd
$H:C_{org}$	Molar ratio	tbd	tbd
Total ash[a]	wt% (d.b.)	1.25	0.42 (11)
Total N	wt% (d.b.)	<0.10	- (9)
pH	[-]	7.91	0.30 (4)
Electric conductivity	dS/m	0.09	0.03 (4)
Liming (if pH above 7)	% CaCO₃	tbd	tbd
Biochar C stability[b]	% C-basis	69.62	0.20 (5)

Production parameters		Mean	Run-to-Run Variation, SD(n)
Nominal HTT	°C	550	- (1)
Reactor wall temp.	°C	550	- (1)
Max. char HTT	°C	543.78	- (1)
Heating rate	°C/min	548.58	- (1)
Kiln residence time	min	12	- (1)
Mean time at HTT	min	3.9	- (1)
Biochar yield	wt% (d.b.)	21.80	0.79 (6)
Pyrolysis liquid yield	wt% (d.b.)	37.00	- (1)
Pyrolysis gas yield	wt% (d.b.)	39.00	- (1)
Pyrolysis liquid HHV	MJ/kg	13.87	- (1)
Pyrolysis gas HHV	MJ/kg	10.66	- (1)

Advanced Analysis & Soil Enhancement Properties		Mean	Run-to-Run Variation, SD(n)
Mineral N (ammonium & nitrate)	mg/kg (d.b.)	<3	- (4)
Total P[c]	wt% (d.b.)	0.06	0.04 (4)
Total K[c]	wt% (d.b.)	0.25	0.07
Available P	mg/kg (d.b.)	tbd	tbd
Volatile Matter[a]	wt% (d.b.)	14.20	0.81 (8)
Total Surface Area	m²/g (d.b.)	26.40	- (1)
External Surface Area	m²/g (d.b.)	tbd	tbd

Toxicant Reporting - Total Content		Mean	Run-to-Run Variation, SD(n)		IBI	EBC (premium)	BQM (high grade)
Germination Inhibition Assay	pass/fail	tbd	tbd				
Polycyclic Aromatic Hydrocarbons (EPA16)[d]	mg/kg dry wt	4.39	3.45 (4)		6-20	4	20
Dioxin/ Furan (total PCDD/ Fs)[e]*	ng/kg dry wt	0.02	- (1)		9	20	20
Polychlorinated Biphenyls (PCBs)[f]	ng/kg dry wt	0.17	-(1)		0.2-0.5	0.2	0.50
As	mg/kg dry wt	0.90	1.19 (3)		12-100	n/a	10
Cd	mg/kg dry wt	3.48	5.76 (3)		1.4-39	1	3
Cr	mg/kg dry wt	34.57	38.17 (3)		64-1200	80	15
Co	mg/kg dry wt	1.04	0.20 (3)		40-150	n/a	n/a
Cu	mg/kg dry wt	19.41	22.31 (3)		63-1500	100	40
Pb	mg/kg dry wt	bdl	- (3)		70-500	120	60
Hg	mg/kg dry wt	bdl	- (3)		1-17	1	1
Mo	mg/kg dry wt	3.36	1.17 (3)		5-20	n/a	10
Ni	mg/kg dry wt	3.30	2.27 (3)		47-600	30	10
Se	mg/kg dry wt	5.68	5.53 (3)		1-36	n/a	5
Zn	mg/kg dry wt	25.71	5.20 (3)		200-7000	400	150

(column note: modified dry ashing followed by ICP-OES)
(column note: comparison vs. recommended standard thresholds+)

Notes: HTT=highest treatment temperature, HHV = higher heating value, tbd = to be defined in next version, bdl. = below detection limit, SD = standard deviation (refers to run-to-run consistency, not analytical error) | available standards related to biochar (IBI = International Biochar Initiative, EBC = European Biochar Standard, BQM = Biochar Quality Mandate), * as TEQ (toxic equivalent) values were bdl, total (tetra to octa chlorinated) dioxin/furan content is reported instead.

(a) TGA, (b) Cross A, Sohi SP (2013), (c) Aqua Regia digestion followed by ICP, (d) Soxhlet extraction (toluene, 6h) determination by GCMS, (e) US EPA 1613, (f) AES O84 (based on US EPA 1668)

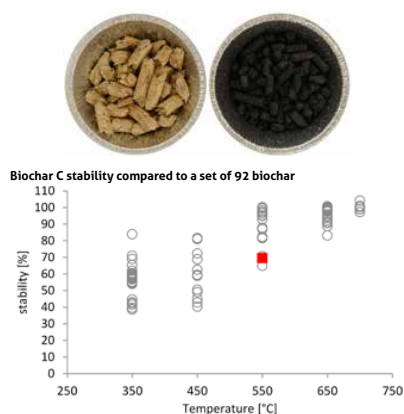For full details please go to: http://www.charchive.org/record.php?record_id=94

UK Biochar Research Centre

reducing and removing CO₂ while improving soils: a significant and sustainable response to climate change

www.biochar.ac.uk | biochar@ed.ac.uk

SWP700

Standard biochar specification sheet – Version 1.0 | November 2014

Feedstock: Soft Wood Pellets | **Production:** Pilot-scale rotary kiln pyrolysis unit, nominal peak temperature 700°C

Key features: ● Reproducible ● Extensively characterised ● Readily available

Biochar C stability compared to a set of 92 biochar

Basic Utility Properties		Mean	Run-to-Run Variation, SD(n)
Moisture[a]	wt% (a.r.)	1.00	0.24 (8)
C_{tot}	wt% (d.b.)	90.21	0.39 (9)
H	wt% (d.b.)	1.83	0.15 (9)
O (by difference)	wt% (d.b.)	6.02	0.74 (8)
$H:C_{tot}$	Molar ratio	0.24	0.02 (8)
$O:C_{tot}$	Molar ratio	0.05	0.01 (8)
C_{org}	wt% (d.b.)	tbd	tbd
$H:C_{org}$	Molar ratio	tbd	tbd
Total ash[a]	wt% (d.b.)	1.89	0.43 (8)
Total N	wt% (d.b.)	<0.1	- (9)
pH	[-]	8.44	0.69 (4)
Electric conductivity	dS/m	0.16	0.06 (4)
Liming (if pH above 7)	% CaCO₃	tbd	tbd
Biochar C stability[b]	% C-basis	97.27	0.50 (7)

Production parameters		Mean	Run-to-Run Variation, SD(n)
Nominal HTT	°C	700	- (1)
Reactor wall temp.	°C	700	- (1)
Max. char HTT	°C	680	- (1)
Heating rate	°C/min	87	- (1)
Kiln residence time	min	12	- (1)
Mean time at HTT	min	5	- (1)
Biochar yield	wt% (d.b.)	17.34	2.46 (6)
Pyrolysis liquid yield	wt% (d.b.)	27.64	- (1)
Pyrolysis gas yield	wt% (d.b.)	54.05	- (1)
Pyrolysis liquid HHV	MJ/kg	1.06	- (1)
Pyrolysis gas HHV	MJ/kg	12.6	- (1)

Advanced Analysis & Soil Enhancement Properties		Mean	Run-to-Run Variation, SD(n)
Mineral N (ammonium & nitrate)	mg/kg (d.b.)	<3	- (4)
Total P[c]	wt% (d.b.)	0.07	0.04 (4)
Total K[c]	wt% (d.b.)	0.28	0.09 (4)
Available P	mg/kg (d.b.)	tbd	tbd
Volatile Matter[a]	wt% (d.b.)	6.66	0.46 (8)
Total Surface Area	m²/g (d.b.)	162.3	- (1)
External Surface Area	m²/g (d.b.)	tbd	tbd

Toxicant Reporting - Total Content		Mean	Run-to-Run Variation, SD(n)		IBI	EBC (premium)	BQM (high grade)
Germination Inhibition Assay	pass/fail	tbd	tbd				
Polycyclic Aromatic Hydrocarbons (EPA16)[d]	mg/kg dry wt	0.18	0.08 (9)		6-20	4	20
Dioxin/ Furan (PCDD/ Fs)[e]	ng/kg dry wt	3.30	- (1)		9	20	20
Polychlorinated Biphenyls (PCBs)[f]	ng/kg dry wt	0.17	- (1)		0.2-0.5	0.2	0.50
As	mg/kg dry wt	0.61	0.69 (3)	modified dry ashing followed by ICP-OES	12-100	n/a	10
Cd	mg/kg dry wt	8.16	13.86 (3)		1.4-39	1	3
Cr	mg/kg dry wt	123.35	49.92 (3)		64-1200	80	15
Co	mg/kg dry wt	4.37	1.73 (3)		40-150	n/a	n/a
Cu	mg/kg dry wt	9.66	3.03 (3)		63-1500	100	40
Pb	mg/kg dry wt	bdl	- (3)		70-500	120	60
Hg	mg/kg dry wt	bdl	- (3)		1-17	1	1
Mo	mg/kg dry wt	38.54	26.17 (3)		5-20	n/a	10
Ni	mg/kg dry wt	74.07	31.09 (3)		47-600	30	10
Se	mg/kg dry wt	bdl	- (3)		1-36	n/a	5
Zn	mg/kg dry wt	99.60	141.28 (3)		200-7000	400	150

comparison vs. recommended standard thresholds +

Notes: HTT=highest treatment temperature, HHV = higher heating value, tbd = to be defined in next version, bdl. = below detection limit, SD = standard deviation (refers to run-to-run consistency, not analytical error) + available standards related to biochar (IBI = International Biochar Initiative, EBC = European Biochar Standard, BQM = Biochar Quality Mandate), ᵉ as TEQ (toxic equivalent) values were bdl, total (tetra to octa chlorinated) dioxin/furan content is reported instead.

(a) TGA, (b) Cross A, Sohi SP (2013), (c) Aqua Regia digestion followed by ICP, (d) Soxhlet extraction (toluene, 6h) determination by GCMS, (e) US EPA 1613, (f) AES O84 (based on US EPA 1668)

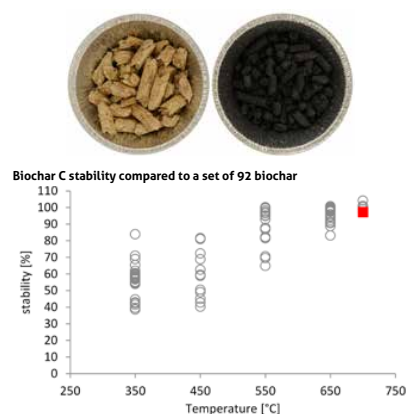For full details please go to: http://www.charchive.org/record.php?record_id=95
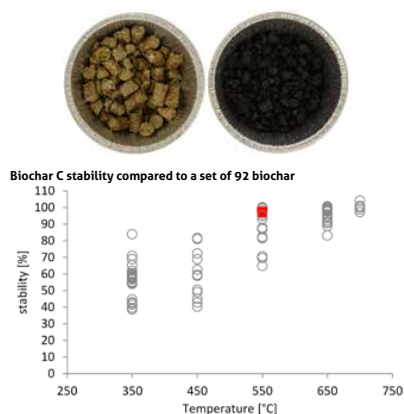
UK Biochar Research Centre

reducing and removing CO₂ while improving soils: a significant and sustainable response to climate change

www.biochar.ac.uk | biochar@ed.ac.uk

WSP550

Standard biochar specification sheet – Version 1.0 | November 2014

Feedstock: Wheat Straw Pellets | **Production:** Pilot-scale rotary kiln pyrolysis unit, nominal peak temperature 550°C

Key features: ● Reproducible   ● Extensively characterised   ● Readily available

Biochar C stability compared to a set of 92 biochar

Basic Utility Properties		Mean	Run-to-Run Variation, SD(n)
Moisture[a]	wt% (a.r.)	1.88	0.08 (7)
C_{tot}	wt% (d.b.)	68.26	1.10 (6)
H	wt% (d.b.)	2.10	0.25 (6)
O (by difference)	wt% (d.b.)	6.92	0.33 (6)
$H:C_{tot}$	Molar ratio	0.37	0.05 (6)
$O:C_{tot}$	Molar ratio	0.08	0.00 (6)
C_{org}	wt% (d.b.)	tbd	tbd
$H:C_{org}$	Molar ratio	tbd	tbd
Total ash[a]	wt% (d.b.)	21.25	1.09 (7)
Total N	wt% (d.b.)	1.39	0.10 (6)
pH	[-]	9.94	0.16 (4)
Electric conductivity	dS/m	1.70	0.43 (4)
Liming (if pH above 7)	% CaCO₃	tbd	tbd
Biochar C stability[b]	% C-basis	96.51	0.30 (5)

Production parameters		Mean	Run-to-Run Variation, SD(n)
Nominal HTT	°C	550	- (1)
Reactor wall temp.	°C	550	- (1)
Max. char HTT	°C	-	- (1)
Heating rate	°C/min	80	- (1)
Kiln residence time	min	15	- (1)
Mean time at HTT	min	5	- (1)
Biochar yield	wt% (d.b.)	24.11	1.08 (6)
Pyrolysis liquid yield	wt% (d.b.)	42.68	- (1)
Pyrolysis gas yield	wt% (d.b.)	31.60	- (1)
Pyrolysis liquid HHV	MJ/kg	1.56	- (1)
Pyrolysis gas HHV	MJ/kg	9.41	- (1)

Advanced Analysis & Soil Enhancement Properties		Mean	Run-to-Run Variation, SD(n)
Mineral N (ammonium & nitrate)	mg/kg (d.b.)	<3	- (6)
Total P[c]	wt% (d.b.)	0.14	0.02 (4)
Total K[c]	wt% (d.b.)	1.56	0.35 (4)
Available P	mg/kg (d.b.)	tbd	tbd
Volatile Matter[a]	wt% (d.b.)	10.55	0.86 (7)
Total Surface Area	m²/g (d.b.)	26.40	- (1)
External Surface Area	m²/g (d.b.)	tbd	tbd

Toxicant Reporting - Total Content		Mean	Run-to-Run Variation, SD(n)		IBI	EBC (premium)	BQM (high grade)
Germination Inhibition Assay	pass/fail	tbd	tbd				
Polycyclic Aromatic Hydrocarbons (EPA16)[d]	mg/kg dry wt	0.40	0.28 (6)		6-20	4	20
Dioxin/ Furan (PCDD/ Fs)[e]	ng/kg dry wt	4.30	- (1)		9	20	20
Polychlorinated Biphenyls (PCBs)[f]	ng/kg dry wt	0.013	- (1)		0.2-0.5	0.2	0.50
As	mg/kg dry wt	1.16	0.21 (3)		12-100	n/a	10
Cd	mg/kg dry wt	3.15	1.14 (3)		1.4-39	1	3
Cr	mg/kg dry wt	bdl	- (3)		64-1200	80	15
Co	mg/kg dry wt	1.54	0.60 (3)		40-150	n/a	n/a
Cu	mg/kg dry wt	3.63	0.39 (3)		63-1500	100	40
Pb	mg/kg dry wt	bdl	- (3)		70-500	120	60
Hg	mg/kg dry wt	bdl	- (3)		1-17	1	1
Mo	mg/kg dry wt	0.84	0.20 (3)		5-20	n/a	10
Ni	mg/kg dry wt	1.00	0.74 (3)		47-600	30	10
Se	mg/kg dry wt	bdl	- (3)		1-36	n/a	5
Zn	mg/kg dry wt	10.50	2.90 (3)		200-7000	400	150

(As–Zn rows: modified dry ashing followed by ICP-OES; comparison vs. recommended standard thresholds+)

Notes: HTT=highest treatment temperature, HHV = higher heating value, tbd = to be defined in next version, bdl. = below detection limit, SD = standard deviation (refers to run-to-run consistency, not analytical error) + available standards related to biochar (IBI = International Biochar Initiative, EBC = European Biochar Standard, BQM = Biochar Quality Mandate), ᵉ as TEQ (toxic equivalent) values were bdl, total (tetra to octa chlorinated) dioxin/furan content is reported instead.

(a) TGA, (b) Cross A, Sohi SP (2013), (c) Aqua Regia digestion followed by ICP, (d) Soxhlet extraction (toluene, 6h) determination by GCMS, (e) US EPA 1613, (f) AES O84 (based on US EPA 1668)

For full details please go to: http://www.charchive.org/record.php?record_id=100
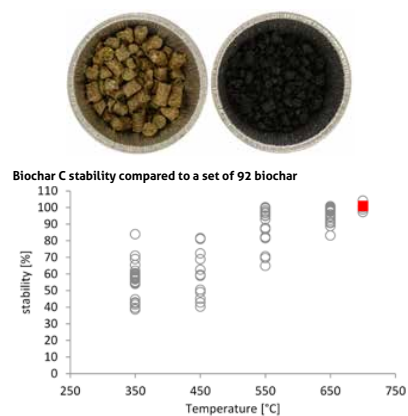
UK Biochar Research Centre

reducing and removing CO₂ while improving soils: a significant and sustainable response to climate change

www.biochar.ac.uk | biochar@ed.ac.uk

WSP700

Standard biochar specification sheet – Version 1.0 | November 2014

Feedstock: Wheat Straw Pellets | **Production:** Pilot-scale rotary kiln pyrolysis unit, nominal peak temperature 700°C

Key features: ● Reproducible ● Extensively characterised ● Readily available

Biochar C stability compared to a set of 92 biochar

Basic Utility Properties		Mean	Run-to-Run Variation, SD(n)
Moisture[a]	wt% (a.r.)	2.17	0.22 (5)
C_{tot}	wt% (d.b.)	69.04	1.32 (4)
H	wt% (d.b.)	1.18	0.04 (4)
O (by difference)	wt% (d.b.)	5.30	1.06 (4)
$H:C_{tot}$	Molar ratio	0.20	0.01 (4)
$O:C_{tot}$	Molar ratio	0.06	0.01 (4)
C_{org}	wt% (d.b.)	tbd	tbd
$H:C_{org}$	Molar ratio	tbd	tbd
Total ash[a]	wt% (d.b.)	23.82	2.33 (5)
Total N	wt% (d.b.)	1.32	0.03 (4)
pH	[-]	10.03	0.19 (4)
Electric conductivity	dS/m	1.52	0.42 (4)
Liming (if pH above 7)	% $CaCO_3$	tbd	tbd
Biochar C stability[b]	% C-basis	100.97	0.21 (5)

Production parameters		Mean	Run-to-Run Variation, SD(n)
Nominal HTT	°C	700	- (1)
Reactor wall temp.	°C	700	- (1)
Max. char HTT	°C	668	- (1)
Heating rate	°C/min	79	- (1)
Kiln residence time	min	15	- (1)
Mean time at HTT	min	6	- (1)
Biochar yield	wt% (d.b.)	23.54	0.76 (4)
Pyrolysis liquid yield	wt% (d.b.)	tbd	tbd
Pyrolysis gas yield	wt% (d.b.)	tbd	tbd
Pyrolysis liquid HHV	MJ/kg	tbd	tbd
Pyrolysis gas HHV	MJ/kg	tbd	tbd

Advanced Analysis & Soil Enhancement Properties		Mean	Run-to-Run Variation, SD(n)
Mineral N (ammonium & nitrate)	mg/kg (d.b.)	<3	- (4)
Total P[c]	wt% (d.b.)	0.25	0.10 (4)
Total K[c]	wt% (d.b.)	1.47	0.77 (4)
Available P	mg/kg (d.b.)	tbd	tbd
Volatile Matter[a]	wt% (d.b.)	7.38	0.78 (4)
Total Surface Area	m²/g (d.b.)	23.20	- (1)
External Surface Area	m²/g (d.b.)	tbd	tbd

Toxicant Reporting - Total Content		Mean	Run-to-Run Variation, SD(n)		IBI	EBC (premium)	BQM (high grade)
Germination Inhibition Assay	pass/fail	tbd	tbd				
Polycyclic Aromatic Hydrocarbons (EPA16)[d]	mg/kg dry wt	<0.11	- (3)		6-20	4	20
Dioxin/ Furan (PCDD/ Fs)[e]	ng/kg dry wt	1.80	- (1)		9	20	20
Polychlorinated Biphenyls (PCBs)[f]	ng/kg dry wt	0.001	- (1)		0.2-0.5	0.2	0.50
As	mg/kg dry wt	1.26	0.03 (3)		12-100	n/a	10
Cd	mg/kg dry wt	1.27	1.58 (3)		1.4-39	1	3
Cr	mg/kg dry wt	4.45	3.99 (3)		64-1200	80	15
Co	mg/kg dry wt	1.58	1.24 (3)		40-150	n/a	n/a
Cu	mg/kg dry wt	4.68	0.35 (3)		63-1500	100	40
Pb	mg/kg dry wt	bdl	- (3)		70-500	120	60
Hg	mg/kg dry wt	bdl	- (3)		1-17	1	1
Mo	mg/kg dry wt	3.26	3.00 (3)		5-20	n/a	10
Ni	mg/kg dry wt	2.50	2.19 (3)		47-600	30	10
Se	mg/kg dry wt	bdl	- (3)		1-36	n/a	5
Zn	mg/kg dry wt	12.03	12.55 (3)		200-7000	400	150

(modified dry ashing followed by ICP-OES) (comparison vs. recommended standard thresholds +)

Notes: HTT=highest treatment temperature, HHV = higher heating value, tbd = to be defined in next version, bdl. = below detection limit, SD = standard deviation (refers to run-to-run consistency, not analytical error) + available standards related to biochar (IBI = International Biochar Initiative, EBC = European Biochar Standard, BQM = Biochar Quality Mandate), ᵉ as TEQ (toxic equivalent) values were bdl, total (tetra to octa chlorinated) dioxin/furan content is reported instead.

(a) TGA, (b) Cross A, Sohi SP (2013), (c) Aqua Regia digestion followed by ICP, (d) Soxhlet extraction (toluene, 6h) determination by GCMS, (e) US EPA 1613, (f) AES O84 (based on US EPA 1668)

For full details please go to: http://www.charchive.org/record.php?record_id=93

Bibliography

[1]   M Cardona. *Fundamentals of Semiconductors Physics and Material Properties*. Ed. by Springer. 2010.

[2]   M Cardona. *Light Scattering in Solids II*. Ed. by Springer. 1982.

[3]   A C Ferrari. "Raman spectroscopy of amorphous, nanostructured, diamond-like carbon, and nanodiamond". In: *The Royal Society* (2004).

[4]   A C Ferrari. *Raman spectroscopy of graphene and graphite: Disorder, electron–phonon coupling, doping and nonadiabatic effects*. 2007. URL: www.sciencedirect.com.

[5]   D J Griffiths. *Introduction to Quantum Mechanics*. Ed. by Pearson Education Inc. 2005.

[6]   Howell G M Edwards Ian R Lewis. *Handbook of Raman Spectroscopy*. Ed. by Taylor and Francis Group. 2001.

[7]   R L Liboff. *Introductory Quantum Mechanics*. Ed. by Addison Wesley. 2003.

[8]   Derek A. Long. *The Raman Effect: A Unified Treatment of the Theory of Raman Scattering by Molecules*. Ed. by John Wiley & Sons Ltd. 2002.

[9]   G. Dresselhaus M. A. Pimenta and A. Jorioa. *Studying disorder in graphite-based systems by Raman spectroscopy*. 2007. URL: http://pubs.rsc.org.

[10] Stephane Neuville. *Advanced ta-C Coating with updated Fundamentals for Energy Production Efficiency Increase*. 2016. URL: www.sciencedirect.com.

[11] Stephane Neuville. *Carbon structure Analysis with Differentiated Raman spectroscopy*. 2014. URL: https://www.researchgate.net/publication/289648360.

[12] Stephane Neuville. "Perspective on Low Energy Bethe Nuclear Fusion Reactor with Quantum Electronic Atomic Rearrangement of Carbon". In: *J. Condensed Matter Nucl. Sci.* (2017).

[13] Stephane Neuville. *Quantum electronic mechanisms of atomic rearrangements during growth of hard carbon films*. 2011. URL: www.elsevier.com/locate/surfcoat.

[14] Gupta N. Poveda R.L. *Carbon Nanofiber Reinforced Polymer Composites*. 2016. URL: http://www.springer.com/978-3-319-23786-2.

[15] T Li S Wang. *Second-order Raman spectroscopy of char during gasification*. 2014. URL: www.elsevier.com/locate/fuproc.

[16] Barbara Stuart. *Infrared Spectroscopy: Fundamentals and Applications*. Ed. by John Wiley & Sons Ltd. 2002.